Evaluating Physiological Coherence of Microvascular Hemodynamics between Brain and Skeletal Muscle using High-Resolution Near-Infrared Spectroscopy.

by

Isuru Sachitha Bandara Herath

A thesis submitted to the Faculty of Graduate Studies of

The University of Manitoba

in partial fulfilment of the requirements of the degree of

MASTER OF SCIENCE

Graduate Program in Biomedical Engineering

University of Manitoba

Winnipeg, Canada

This dissertation is the result of my own work and includes nothing which is the outcome of work done in collaboration except where specifically indicated in the text. It is not substantially the same as any that I have submitted, nor is being concurrently submitted for a degree or diploma or other qualification at the University of Manitoba or any other University or similar institution except as declared in the Preface and specified in the text. I further state that no substantial part of my dissertation has already been submitted, or is being concurrently submitted for any such degree, diploma or other qualification at the University of Manitoba or any other University or similar institution except as declared in the Preface and specified in the text.

ACKNOWLEDGEMENT

I would like to express my deepest gratitude to my supervisor, Dr. Asher Mendelson, for his unwavering patience, kindness, and invaluable guidance. Your mentorship has profoundly shaped my academic journey, and your support in helping me navigate a new country and research domain has meant the world to me.

I also express my deepest gratitude to Dr. Frederick A. Zeiler for his invaluable guidance and the opportunities that inspired me to pursue further studies with confidence and purpose.

I am grateful to all the patients and healthy volunteers who generously consented to participate in this research, contributing to the advancement of knowledge for the betterment of society.

I also thank Dr. Rodrigo Villar for his guidance and for facilitating the collection of healthy control data at his research lab.

A sincere thank you to my undergraduate supervisors, Dr. Randima Dinalankara, Dr. Udaya Wijenayake, and Dr. Akila Subasinghe, and to all the lecturers at the Faculty of Engineering, University of Sri Jayewardenepura, as well as my school teachers in Sri Lanka, for shaping my academic foundation and instilling in me the drive to go further.

To my lab mates at the Critical Care Lab, Amirali, Britney, and Raju, thank you very much for your companionship, support, and encouragement throughout this journey.

I deeply appreciate my parents and family for nurturing me and supporting my path to becoming an engineer and academic.

To the love of my life, thank you very much for embarking on this journey with me, leaving behind the comforts of home, and building our new lives together from scratch in a new country.

Finally, I extend my heartfelt appreciation to the taxpayers of Sri Lanka and Canada for sustaining publicly funded education and research and making this research possible for the betterment of society.

TABLE OF CONTENTS

LIST OF TABLES

LIST OF FIGURES

LIST OF ABBREVIATION

hr-NIRS	High-Resolution Near-Infrared Spectroscopy
NIRS	Near-Infrared Spectroscopy
ICU	Intensive Care Unit
BMI	Body Mass Index
MHC	Microvascular Hemoglobin Content
HbT	Total hemoglobin
TSI	Tissue Saturation Index
ABP	Arterial Blood Pressure
NIBP	Non-Invasive Blood Pressure
ICA	Independent Component Analysis
MAPopt	Optimal Mean Arterial Pressure
O2Hb	Oxy-hemoglobin
HHb	Deoxy-hemoglobin
MIMICSS	Microvascular Monitoring in Circulatory Shock in Sepsis Longitudinal Observational Cohort Study
CA	Cerebral Autoregulation
CBF	Cerebral Blood Flow
LLA	Lower Limit of Autoregulation
ULA	Upper Limit of Autoregulation
OEF	Oxygen Extraction Fraction
MODS	Multiple Organ Dysfunction Syndrome
CIPNM	Critical Illness Polyneuropathy and Myopathy
BBB	Blood-Brain Barrier
TBI	Traumatic Brain Injury
CPP	Cerebral Perfusion Pressure
ICP	Intracranial Pressure
SVR	Systemic Vascular Resistance
DPF	Differential Path Length Factor
CW NIRS	Continuous Wave Near-Infrared Spectroscopy
TRS NIRS	Time-Resolved Spectroscopy Near-Infrared Spectroscopy

SRS NIRS	Spatially Resolved Spectroscopy Near-Infrared Spectroscopy
FD NIRS	Frequency-Domain Near-Infrared Spectroscopy
STFT	Short-Time Fourier Transform
CWT	Continuous Wavelet Transform
DWT	Discrete Wavelet Transform
DTW	Dynamic Time Warping
PAA	Piecewise Aggregate Approximation
wPRx	Wavelet Semblance-based Pressure Reactivity Index
LSL	Lab Streaming Layer
ICM	Intensive Care Monitoring (software)
MV	Microvascular (frequency band)
CW	Continuous Wave
TRS	Time-Resolved Spectroscopy
SRS	Spatially Resolved Spectroscopy
FD	Frequency Domain
RBC	Red Blood Cell
QO2	Rate of Oxygen Delivery
VO2	Oxygen Consumption
DO2	Diffusive Oxygen Conductance
COx	Cerebral Oximetry Index
%signfCoherenceDuration	Percentage of Time Above the Significant Coherence Durations of Wavelet Coherence

ABSTRACT

Physiological coherence between organ-specific microvascular hemodynamics is a fundamental yet underexplored aspect of human systemic blood flow regulation, particularly in systemic vascular diseases such as critical illness. Current critical care monitoring predominantly relies on systemic macro-hemodynamic parameters, which fail to capture the heterogeneity and dynamic relationships of microvascular perfusion across organs like brain and skeletal muscle. This knowledge gap is especially evident regarding the temporal and frequency-specific coherence of microvascular signals between these organs, limiting the development of targeted, organ-specific therapies. To address this, we developed a novel methodological framework to quantify physiological coherence between brain and skeletal muscle microcirculation using high-resolution Near-Infrared Spectroscopy (hr-NIRS) and advanced wavelet-based signal processing. This study employed continuous, non-invasive monitoring in ICU patients (n=40) and healthy controls (n=15), simultaneously acquiring total hemoglobin (HbT) from the frontal cortex and brachioradialis, along with systemic blood pressure. Time-frequency and time-phasic relationships were characterized using wavelet coherence and semblance analyses, assessing both the strength and synchrony of microvascular coupling across cardiac and microvascular frequency bands. Key findings include: (i) ICU patients exhibited significantly reduced coherence duration and phase synchrony between brain and skeletal muscle microcirculation in the cardiac frequency band compared to healthy controls; (ii) ICU non-survivors demonstrated excessive synchronization between skeletal muscle microcirculation and systemic blood pressure in the microvascular and cardiac frequency bands compared to ICU survivors. These results establish, for the first time, that dynamic physiological coherence between brain and skeletal muscle microcirculation is significantly altered in critical illness, with distinct patterns associated with patient outcomes. Integrating wavelet-based coherence metrics into bedside monitoring offers a promising direction for the development of novel biomarkers to guide personalized therapeutic strategies and risk stratification in the ICU.

Keywords: *Biomedical Signal Processing, Microvascular Hemodynamics, Wavelet Coherence, Semblance, hr-NIRS*

1 CHAPTER 1 - INTRODUCTION

1.1 General Introduction

The human body is a complex system exhibiting organ-specific anatomical and functional physiology while maintaining homeostasis. Although the body functions as an interconnected network of organs, systems, and regulatory mechanisms, many physiological relationships among these components remain poorly understood. Among these mechanisms, the microcirculation plays a critical role as the primary interface between the cardiovascular system and the organs of the body for oxygen delivery, nutrient exchange, and metabolic waste removal, through the precise regulation of blood flow in arterioles, capillaries, and venules[1,2]. Despite the critical role of the microcirculation in maintaining systemic physiological function, the physiological coherence between organ-specific microvascular hemodynamics remains poorly characterized, particularly in the context of systemic vascular diseases such as critical illness[3,4].

Existing critical care monitoring predominantly relies on systemic and macro-hemodynamic parameters such as Mean Arterial Pressure (MAP), cardiac output and ECG (Electrocardiogram)[5–8]. These systemic and macro-hemodynamic parameters reflect systemic circulation and do not reliably indicate organ-specific microcirculatory status[9,10]. Current studies correlated perfusion status with better ICU outcomes compared to macro-hemodynamics[11,12], where peripheral perfusion clinical indicators: such as capillary refill time, skin mottling, and body temperature gradients are used as resuscitation targets[13,14]. Also, recent clinical investigations have indicated that organ-specific microcirculation measures, such as regional cerebral oxygen saturation (rSO_2) and tissue oxygen saturation (StO_2), are significantly associated with patient outcomes[15–19]. However, these studies have focused exclusively on organ-specific microvascular hemodynamics and their individual associations with patient outcomes. To date, according to our knowledge, no studies have been conducted to evaluate the physiological coherence of microvascular hemodynamics between brain and skeletal muscle tissues in critically ill or healthy populations.

Recent advances in non-invasive monitoring technologies, specifically High-Resolution Near-Infrared Spectroscopy (hr-NIRS)[20–22], have enabled simultaneous monitoring of microcirculation dynamics in targeted organs such as the brain and skeletal muscle through continuous, high-frequency time series data acquisition. Thus, this enables the simultaneous monitoring of

microcirculatory dynamics of multiple organs along with systemic blood pressure. These signals can be analyzed using advanced biomedical signal processing techniques to assess physiological coherence, that is, the degree of synchronized or coordinated behavior of microvascular hemodynamics between the brain and skeletal muscle, as well as their coupling with systemic blood pressure.

While the vital role of microcirculation in maintaining systemic physiological function is well recognized, the physiological coherence between organ-specific microvascular hemodynamics between the brain and skeletal muscle remains insufficiently characterized in terms of both healthy state and critical illness. Thus, this thesis aims to advance our understanding of dynamic interactions between organ-specific microvascular hemodynamics using hr-NIRS and advanced biomedical signal processing techniques by the following objectives:

I. Evaluating physiological coherence of microvascular hemodynamics between brain and skeletal muscle along with systemic blood pressure in ICU patients and Healthy control

II. Evaluating ICU patients' outcome based on physiological coherence of microvascular hemodynamics between brain and skeletal muscle along with systemic blood pressure

By systematically addressing these objectives, this thesis seeks to bridge the current knowledge gap concerning the physiological coherence of microvascular hemodynamics in the brain and skeletal muscle, alongside systemic blood pressure, in both healthy states and critical illnesses. The anticipated findings aim to offer foundational insights for future research focused on developing biomarkers that assess the physiological coherence between organ-specific microvascular hemodynamics and systemic circulation. Such advancements could enhance the understanding of microvascular function in critical care settings and support the development of personalized therapeutic strategies, ultimately leading to improved patient outcomes.

1.2 Aims and Hypotheses

Current literature has extensively characterized organ-specific microvascular hemodynamics in healthy individuals and critically ill patients using high-resolution Near-Infrared Spectroscopy[15,16,18,23]. In ICU populations, research has primarily focused on isolated parameters such as rSO_2 and StO_2 of skeletal muscle, demonstrating associations with clinical outcomes including mortality and organ dysfunction[15,17]. While some studies have examined temporal associations between rSO_2 and StO_2 in ICU settings, these analyses are often limited by low temporal resolution and the absence of comparative data from healthy populations[15].

Furthermore, studies have analyzed the correlation between hr-NIRS-derived mean arterial pressure (MAP) metrics obtained from brain and skeletal muscle microcirculation monitoring, highlighting the technical feasibility and potential clinical relevance of simultaneous microvascular hemodynamic monitoring in brain and skeletal muscle[24]. However, these investigations also lack comparative analyses with healthy cohorts.

Moreover, studies have explored the time-frequency and time-phasic characteristics of physiological coherence of microvascular hemodynamics between multiple sites within the brain, correlating these dynamic patterns with disease states[25–27]. Nevertheless, these studies have not conducted cross-population comparisons involving healthy individuals.

Collectively, the current literature emphasizes the heterogeneity of physiological coherence of microvascular hemodynamics between multiple sites or regions within the same organ (e.g., coherence between different cerebral regions by comprising microvascular hemodynamics signals from these multiple regions) and suggests the potential significance of evaluating physiological coherence of microvascular hemodynamics between different organs as a holistic marker of microvascular function in humans.

Despite these advances in existing literature, no studies to date have assessed the physiological coherence of microvascular hemodynamics between the brain and skeletal muscle, nor their relationships with systemic blood pressure, while comparing these dynamics between healthy subjects, critically ill ICU patients, and across ICU survivors and non-survivors. This represents a significant gap in the current understanding of systemic and organ-specific microvascular hemodynamics. Thus, addressing this knowledge gap is critically important because understanding

inter-organ microvascular hemodynamic coordination could provide fundamental insights into systemic and organ-specific microvascular regulation mechanisms, enable clinicians to identify critically ill patients at higher risk of poor outcomes, and potentially guide targeted therapeutic interventions to optimize microvascular function.

Therefore, to address this knowledge gap, the present study proposes a prospective observational cohort design to evaluate the physiological coherence of microvascular hemodynamics between the brain and skeletal muscle, as well as their relationships with systemic blood pressure, through simultaneous microvascular hemodynamics monitoring using hr-NIRS in both critically ill ICU patients and healthy cohorts. Accordingly, this study will assess the following two hypotheses.

HYPOTHESIS # 1.1: The physiological coherence of microvascular hemodynamics between the brain and skeletal muscle, and with systemic blood pressure, is significantly altered in ICU patients compared to healthy controls.

HYPOTHESIS # 1.2: The ICU non-survivors exhibit significantly altered physiological coherence of microvascular hemodynamics between the brain and skeletal muscle, and with systemic blood pressure, compared to ICU survivors.

1.3 Thesis Overview

The following chapters are structured to provide a comprehensive foundation, methodological rigor, and critical analysis of the research findings, as outlined below,

Chapter 2-Literature Review: This chapter provides a comprehensive review of the foundational physiology of the circulatory system, with detailed discussions on microcirculation in the brain and skeletal muscle, and the pathophysiology of microvascular dysfunction in critical illness. It covers the principles and clinical applications of NIRS technology for non-invasive tissue oxygenation monitoring and reviews digital signal processing techniques focusing wavelet-based time-frequency analysis used to assess dynamic relationships in physiological signals. The literature review culminates in a synthesis of current knowledge, identifying the lack of studies on

microvascular coherence between brain and skeletal muscle and justifying the thesis's research direction.

Chapter 3 - Methodology: This chapter details the experimental design, participant recruitment (including ICU patients and healthy controls), instrumentation (hr-NIRS setup), data acquisition protocols, and preprocessing pipelines. It provides a thorough description of the analytical framework, including the implementation of wavelet coherence and semblance analyses for quantifying physiological coherence across organ systems.

Chapter 4 - Results: This chapter is structured around the research hypotheses, presenting comparative analyses of physiological coherence metrics between ICU patients and healthy controls, and between ICU survivors and non-survivors. This chapter includes statistical analyses, visualizations, and tabulated findings to support the interpretation of results.

Chapter 5 – Discussion: The discussion chapter interprets the results in the context of existing literature, emphasizing the novelty and clinical relevance of physiological coherence of microvascular hemodynamics between brain and skeletal muscle and their relationships with systemic blood pressure as a potential biomarker. The chapter critically evaluates the significance of altered physiological coherence in ICU patients, discusses potential mechanisms, and considers the clinical relevance of these findings for prognosis and therapeutic decision-making. Limitations of the study and methodological considerations are also addressed.

Chapter 6 – Conclusion: This chapter summarizes the key findings of the thesis, reiterates their significance, and highlights how the research advances current knowledge on physiological coherence of microvascular hemodynamics between brain and skeletal muscle in health and disease.

Chapter 7 – Future Directions: The final chapter outlines potential directions for future research, including the development of novel biomarkers for evaluating inter-organ physiological coherence of microvascular hemodynamics, the integration of advanced signal processing techniques and microvascular hemodynamics monitoring technologies, and the translation of these findings into clinical practice to improve patient outcomes in critical care settings.

2 CHAPTER 2 - LITERATURE REVIEW

2.1 Overview of Circulatory System, Physiology of Microcirculation in the Brain and Skeletal Muscle, and Pathophysiology of Microvascular Dysfunction in Critical Illness

2.1.1 Circulatory system: Overview

The human circulatory system functions as a sophisticated transport mechanism for the distribution of oxygen, nutrients, and immunological mediators while simultaneously removing metabolic byproducts[1,28,29]. This integrated network operates through two interdependent pathways: the systemic circulation, which distributes oxygen-rich blood from the heart to peripheral tissues before returning deoxygenated blood through venous structures, and the pulmonary circulation, which directs deoxygenated blood through pulmonary arteries for alveolar gas exchange before oxygenated blood returns via pulmonary veins[30–32].

Blood, the primary transport medium within the circulatory system, comprises four functionally distinct components that operate in unison[1]. Red blood cells (RBCs) containing hemoglobin proteins that demonstrate high oxygen-binding characteristics through cooperative binding kinetics[1,33]. White blood cells utilize defensive mechanisms for immune responses against infections[34]. Platelets work as active agents in blood clotting, preventing excessive bleeding. Plasma serves as a liquid medium of blood that carries these cells, along with proteins, electrolytes, and other essential substances[1,35].

Hemoglobin (Hb) within RBCs binds to oxygen that diffuses across the alveolar membrane into capillaries of the lungs, forming Oxyhemoglobin (O2Hb), which is then transported to the tissues. Upon reaching the tissues, O2Hb releases oxygen, which diffuses into cells to support metabolic processes, and upon releasing oxygen, O2Hb becomes deoxy-hemoglobin (HHb). After oxygen is released, HHb is transported back to the lungs via the venous circulation where it binds with oxygen again to reform O2Hb. The mechanism of binding and release of oxygen by hemoglobin are influenced by several factors, including pH, temperature, and CO_2 levels[36]. The Bohr effect describes how a decrease in pH or an increase in CO_2 partial pressure reduces hemoglobin's affinity for oxygen, facilitating oxygen release in metabolically active tissues[37,38]. Conversely, the Haldane effect explains how deoxygenated hemoglobin increases CO_2 transport, promoting their removal from tissues[37,38].

In Circulation, the dynamics of blood flow are governed by fluid dynamics principles of pressure, resistance, and flow rate. Blood flows from areas of higher pressure to areas of lower pressure, driven by the heart's pumping action. Resistance to blood flow is influenced by factors such as blood viscosity, vessel length, and vessel diameter. Poiseuille's law quantitatively describes this relationship, stating that flow rate is proportional to the fourth power of the vessel radius and inversely proportional to viscosity and vessel length. These factors collectively determine the biophysics of blood delivery to tissues throughout the body[1,39].

2.1.2 Microcirculation

Microcirculation is blood circulation in the smallest vessels in the body (typically less than 300 μm in diameter), which is the location of nutrient and waste exchange within tissues[1,2]. Microcirculation comprises three different types of blood vessels: arterioles, capillaries, and venules, which have unique structural and functional characteristics[1,40].

Arterioles, the smallest arteries, receive blood flow and pressure from systemic arteries, and regulate blood flow into capillary beds through vasodilation and vasoconstriction of smooth muscle surrounding their outer diameter. Capillaries are thin-walled vessels lacking smooth muscle that are the terminal exchange site of nutrients, gases, and waste products between blood and tissues, they are the direct interface between the circulatory system and organs. Venules, the smallest veins, collect deoxygenated blood from capillaries and transport it back to larger veins[2,40]; they are also the predominant site of immune interactions within tissue.

Microvascular regulation ensures tissue vitality by dynamically adjusting blood flow through coordinated physiological systems to match with metabolic demands. Three interconnected mechanisms- myogenic, metabolic, and neurohumoral orchestrate this process to meet cellular demands while maintaining systemic stability[41,42].

Arteriolar smooth muscle cells intrinsically respond to blood pressure fluctuations through the myogenic mechanism. Elevated pressure triggers vasoconstriction to protect delicate capillaries from hyper-perfusion damage, while reduced pressure induces vasodilation to sustain nutrient delivery[42]. This self-stabilizing system operates continuously, exemplified by renal blood flow regulation where cortical arterioles adjust diameters within seconds to preserve filtration rates during blood pressure variations[41,42].

Tissues actively modulate local blood flow by releasing vasoactive signals during heightened activity. For example, exercising muscles generate CO_2 and adenosine, which dilate nearby arterioles to amplify oxygen supply[41,42]. Conversely, oxygen surplus in underutilized regions constricts vessels, optimizing resource distribution. This feedback loop proves critical in neural tissues, where uninterrupted perfusion prevents energy deficits that could impair brain function[41].

Hormones and autonomic nerves synchronize microvascular behavior with whole-body needs. During stress, adrenal epinephrine constricts nonessential vessels via α-adrenergic receptors while dilating cardiac and skeletal muscle vasculature through β-receptors[42]. Chronic conditions like hypertension remodel this system, as evidenced by retinal venule narrowing and cerebral capillary rarefaction observed in small vessel disease studies[41].

In summary, microcirculation serves as the critical interface for nutrient and waste exchange, with its regulation depending on the coordinated action of myogenic, metabolic, and neurohumoral mechanisms. Understanding these regulatory pathways is essential for explaining the pathophysiology of cardiovascular and metabolic diseases, as well as for developing biomarkers and targeted therapeutic strategies to preserve microvascular health[43–46].

2.1.3 Tissue Oxygenation

Tissue oxygenation is the mechanism of delivering oxygen to tissues, which is essential for cellular respiration and energy production[29]. Oxygen serves as the final electron acceptor in the electron transport chain, which is a critical process for Adenosine triphosphate (ATP) production within the mitochondria of the cell. Without sufficient oxygen supply, cells cannot produce enough ATP to meet their energy demands, leading to cellular dysfunction and potentially cell death. Hypoxia, or oxygen deficiency, can result in a range of pathological conditions, including ischemia, inflammation, and organ failure[47,48].

Adequate tissue oxygenation is crucial for maintaining optimal cellular function, preventing tissue damage, and avoiding ultimate organ failures in the body. As explained, the assessment of tissue oxygenation reflects the status of the optimal function of the tissues/organ of interest[49], and the balance between oxygen delivery by the microcirculation and oxygen metabolism at the tissue level.

Oxygen delivery to tissues is transported through oxyhemoglobin, the oxygen-bound form of hemoglobin. Since hemoglobin is contained exclusively within red blood cells, oxygen distribution through the circulatory system depends on the movement of these RBCs within the microcirculation. Therefore, the regulation of oxygen distribution is fundamentally achieved as a function of the microcirculatory system, which ensures that oxygen is distributed in accordance with the metabolic demands of the specific tissues[50,51]. For example, skeletal muscle, which can increase its oxygen consumption by up to 100-fold during exercise[52], relies on the precise regulation of microvascular blood flow to match oxygen supply with metabolic demand.

2.1.4 Microcirculation and Tissue Oxygenation in the Brain and Skeletal Muscle

The brain and skeletal muscle, while both highly dependent on efficient microcirculation for optimal functionality, exhibit distinct physiological demands and microvascular mechanisms and adaptations[2,40,53]. The brain requires a constant and tightly regulated supply of oxygen to maintain neuronal activity and prevent damage. In contrast, skeletal muscle needs to adjust its oxygen delivery dynamically to meet varying metabolic demands during rest and exercise[53,54].

2.1.5 Microcirculation in the Brain.

Microcirculation in the brain can be discussed and reviewed based on four distinct features: Structural Characteristics, Cerebral Regulation of Blood Flow, Oxygen Delivery and Tissue Oxygenation, and Pathophysiology of Microcirculation in the Brain. These aspects are critical for understanding how the brain maintains its highly efficient functionalities.

2.1.5.1 Structural Characteristics:

The microvascular mechanism of the brain is uniquely designed to maintain a stable internal environment.

Blood-Brain Barrier (BBB): The Blood-Brain Barrier is formed by specialized endothelial cells with tight junctions, limiting paracellular permeability. Astrocytic end-feet surrounds the capillaries, providing structural support and regulating Blood-Brain Barrier function[55,56]. Pericytes, which is embedded in the capillary basement membrane, contribute to Blood-Brain Barrier integrity of and blood flow regulation[56]. The Blood-Brain Barrier strictly controls the passage of molecules into the brain, protecting it from harmful substances and maintaining ionic homeostasis[57].

Capillary Density and Morphology: Capillary density in the brain is exceptionally high-averaging 2,500–3,000 capillaries per mm^3 ensuring nearly every neuron is closely supplied with oxygen and nutrients[55,58,59]. These capillaries form a dense, interconnected network with specialized continuous endothelial cells joined by tight junctions, constituting the blood-brain barrier that restricts the passage of plasma proteins and large molecules, thereby maintaining the brain's microenvironment[58]. Capillary walls are supported by pericytes and encased in a basal lamina, with astrocytic end-feet further modulating barrier function and neurovascular signaling[58,60].

Cerebral arterioles, branching from pial arteries, possess a single layer of smooth muscle and are primarily responsible for regulating microvascular pressure and flow into capillaries[58,61]. These arterioles are tightly integrated into the neurovascular unit, responding to neuronal metabolic demand and contributing to functional hyperemia[58,60]. Capillaries drain into post-capillary venules, which lack smooth muscle and gradually merge into larger cortical veins, ultimately emptying into dural venous sinuses[60,61]. Venous components also participate in interstitial fluid and waste clearance, interfacing with meningeal lymphatic vessels[60].

This hierarchical and specialized vascular architecture supports precise neurovascular coupling, efficient nutrient delivery, and waste removal, all critical for maintaining brain health and function[58,60,61].

2.1.5.2 Regulation of Blood Flow:

Cerebral blood flow is strictly regulated to meet the cerebral metabolic demands.

Cerebral Autoregulation: Cerebral autoregulation (CA) is a vital neuroprotective mechanism that maintains stable cerebral blood flow (CBF) despite fluctuations in systemic blood pressure, thereby protecting the brain from hypoperfusion during hypotension and hyperperfusion during hypertension[62]. This mechanism was first described in humans by Lassen[63] and is illustrated by the triphasic "The Lassen curve" (refer Figure 2.1), which depicts how CBF responds to changes in mean arterial pressure (MAP). In the first phase, when MAP falls below the lower limit of autoregulation (LLA) (typically < 60 mmHg), the CA mechanism fails, making CBF pressure-passive and linearly dependent on MAP, resulting in cerebral hypoperfusion and ischemia[64] . The second phase is the plateau phase, where CBF remains constant across a MAP range of approximately 60–150 mmHg due to effective autoregulation. In the third phase, when MAP

exceeds the upper limit of autoregulation (ULA) (typically >150 mmHg), the autoregulatory mechanism again fails, causing CBF to increase passively with MAP and potentially leading to cerebral hyperperfusion and edema[65–67].

Figure 2.1 : The Lassen Curve of Cerebral Autoregulation

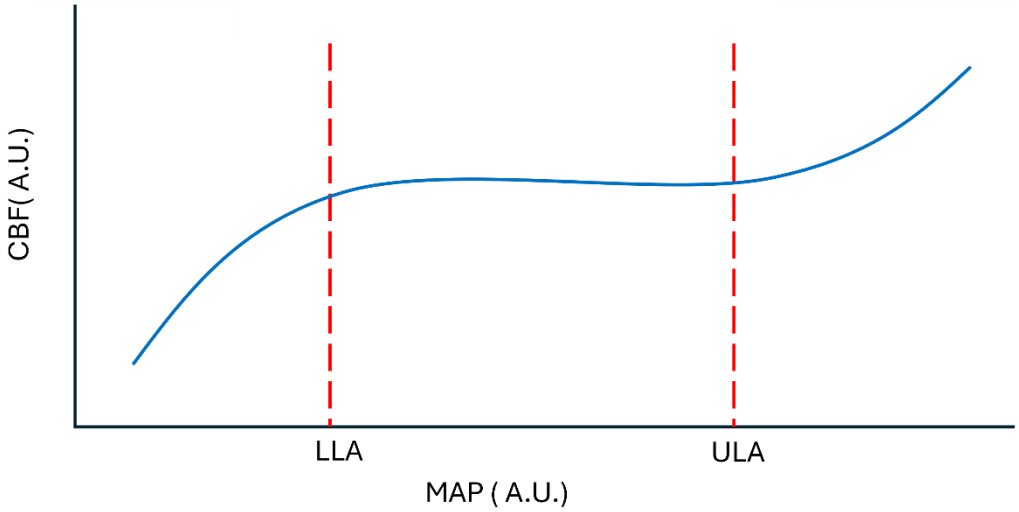

The Lassen curve of Cerebral Autoregulation: Cerebral Blood Flow (CBF) in arbitrary units (A.U.) is plotted against Mean Arterial Pressure (MAP) to demonstrate Cerebral Autoregulation (CA).

Neurovascular Coupling: Neurovascular coupling refers to the close relationship between neuronal activity and local blood flow[68,69]. Functional hyperemia, the increase in blood flow in response to neuronal activity, ensures that active brain regions receive adequate oxygen and glucose[70]. Astrocytes, neurons, and endothelial cells coordinate blood flow by releasing vasoactive substances in response to neuronal signals[71].

2.1.5.3 Oxygen Delivery and Tissue Oxygenation

The brain relies on a high rate of oxygen delivery ($\dot{Q}O_2$) to support its energy-intensive functions.

Oxygen Extraction Fraction: The Oxygen Extraction Fraction (OEF) is the proportion of oxygen removed from the blood by tissue as blood passes through the capillaries, reflecting the balance between oxygen delivery and consumption[72]. Under normal conditions, the brain maintains an OEF of approximately 30% to 40%, extracting approximately one-third of the delivered oxygen while leaving the rest in venous return[73–75]. This moderate extraction efficiency contrasts with its disproportionate metabolic demands despite constituting only 2% of body mass, and it consumes 20% of systemic oxygen[76]. This oxygen surplus provides hemodynamic redundancy,

allowing stable cerebral metabolism despite blood flow fluctuations. The brain receives 15-20% of cardiac output[76] perfusion over-extraction efficiency compared to organs like the heart (OEF >60%)[77]. This physiology reflects evolutionary optimization for continuous oxygen delivery rather than maximal extraction, crucial for maintaining neural function given the lack of oxygen reserves.

Oxygen Gradients: Oxygen diffuses from capillaries to neurons and glial cells along oxygen gradients[78]. The distance that oxygen must diffuse from the capillary to the cell influences the oxygen tension in the tissue. Factors such as blood flow, arterial oxygen content, and diffusion distance affect oxygen delivery to the brain[78].

2.1.5.4 Pathophysiology of Cerebral Microcirculation in Critical Illness

The critical illness causes significant disruptions in cerebral microcirculation, which impact oxygen and other nutrient delivery and potentially lead to severe neurological complications requiring intensive care unit management[46].

Sepsis-Associated Encephalopathy: Sepsis, a systemic inflammatory response to infection, can trigger Sepsis-Associated Encephalopathy. Sepsis-associated encephalopathy is characterized by blood-brain barrier dysfunction, neuroinflammation, and impaired cerebral microcirculatory blood flow[79]. These changes can lead to neuronal injury, cognitive impairments, and increased mortality[80]. ICU management involves addressing the underlying infection, controlling inflammation, and supporting cerebral perfusion pressure to maintain adequate oxygen delivery[81].

Acute Respiratory Distress Syndrome (ARDS): Acute Respiratory Distress Syndrome is a severe form of acute lung injury that can indirectly affect cerebral microcirculation[82]. Hypoxemia and hypercapnia associated with ARDS can impair cerebral autoregulation and increase intracranial pressure[82,83]. Moreover, mechanical ventilation strategies, while life-saving, can have adverse effects on cerebral blood flow. ICU care focuses on optimizing oxygenation and ventilation while carefully monitoring and managing intracranial pressure and cerebral perfusion[83].

Cardiac Arrest and Resuscitation: Cardiac arrest leads to global cerebral ischemia, causing severe microcirculatory damage upon restoration of circulation[84]. Reperfusion injury is characterized by inflammation, oxidative stress, blood-brain barrier disruption, and worsened neuronal damage[85]. Targeted temperature management and precise hemodynamic control are

critical components of ICU care to minimize secondary brain injury and improve neurological outcomes following cardiac arrest[86].

Severe Traumatic Brain Injury (TBI): Severe TBI often results in widespread microcirculatory dysfunction, including Blood-brain barrier breakdown, edema formation, and impaired cerebral blood flow autoregulation[87]. These irregular microvascular changes contribute to secondary brain injury, increasing morbidity and mortality[3]. ICU management strategies include intracranial pressure monitoring and control, cerebral perfusion pressure optimization, and interventions to mitigate neuroinflammation[88–91].

2.1.6 Microcirculation in Skeletal Muscle

Microcirculation in skeletal muscle can be evaluated based on several key aspects: Structural Characteristics, Regulation of Blood Flow, Oxygen Delivery and Tissue Oxygenation, and Pathophysiology of Microcirculation in Skeletal Muscle. These features collectively determine the effectiveness of oxygen and nutrient supply to meet the dynamic metabolic demands of skeletal muscle tissue.

2.1.6.1 Structural Characteristics

The skeletal muscle microvascular system is a hierarchically organized network of arterioles, capillaries, and venules that dynamically regulates oxygen delivery to meet metabolic demands. Arterioles, the primary resistance vessels, govern bulk blood flow distribution via vasomotor responses to local metabolic signals, neural input, and mechanical forces[92,93]. Capillaries form interconnected modules (CMs) of 10–20 parallel vessels originating from terminal arterioles (TAs) and draining into post-capillary venules (PCVs)[51,93]. These CMs are structurally arranged into longitudinal columns termed capillary fascicles (CFs), which align with muscle fascicles to optimize spatial coordination between perfusion and contractile activity[93]. CFs exhibit marked heterogeneity in capillary topology, with converging/diverging bifurcations creating non-uniform red blood cell hemodynamics[93].

Venules not only drain deoxygenated blood but may participate in flow regulation through pressure adjustments, particularly in paired CMs sharing common TAs or PCVs. At rest, >90% of capillaries are perfused, with RBC supply modulated by arteriolar tone and capillary-level rheological adaptations[92,93]. During exercise, CFs enhance $\dot{Q}O_2$ by increasing RBC velocity and hematocrit, while reducing flow heterogeneity to match elevated oxidative demands[92]. The CF's

modular design enables localized flow regulation, allowing skeletal muscle to sustain the increase in metabolic demand during activities[93].

2.1.6.2 Regulation of Blood Flow

Skeletal muscle blood flow is regulated by local metabolic factors, the sympathetic nervous system, and the muscle pump.

Local Metabolic Control: Vasodilation occurs in response to increased metabolic activity in skeletal muscle. Factors such as adenosine, potassium, and nitric oxide mediate this vasodilation[94].

Sympathetic Nervous System: The sympathetic nervous system causes vasoconstriction in skeletal muscle at rest[95]. During exercise, functional sympatholysis occurs, where local metabolic factors override the sympathetic vasoconstriction, leading to vasodilation and increased blood flow[94].

Muscle Pump: The muscle pump refers to the mechanical effect of muscle contraction on blood vessels. Contraction compresses vessels, increasing venous return, while relaxation dilates vessels, enhancing blood flow[96].

2.1.6.3 Oxygen Delivery and Tissue Oxygenation

Oxygen delivery to skeletal muscle is influenced by blood flow, capillary recruitment, and myoglobin.

Oxygen Extraction Fraction: The Oxygen Extraction Fraction in skeletal muscle reflects the balance between oxygen delivery and consumption (VO_2), governed by microvascular hemodynamics and capillary hematocrit dynamics[97]. At rest, approximately 80% of capillaries sustain continuous red blood cells and plasma flow, maintaining a mean capillary PO_2 of ~30 mmHg despite heterogeneous perfusion[97,98]. This ensures moderate OEF (~ 30% – 40%) through preserved diffusive oxygen conductance (DO_2) via capillary RBC spacing and interstitial PO_2 gradients. During exercise, hyperemia elevates RBC flux and velocity, increasing capillary hematocrit[97]. Longitudinal recruitment enhances oxygen delivery by extending the capillary length available for exchange by reducing inter-RBC gaps and optimizing transit time[97]. These adaptations maintain OEF efficiency (up to 80–90%) despite elevated VO_2, preventing significant declines in microvascular PO_2.

In disease states like heart failure and diabetes, impaired capillary hemodynamics reduce the proportion of RBC perfused capillaries[97,99]. This diminishes both QO_2 (impaired perfusion) and DO_2, lowering OEF and slowing VO_2 kinetics[100].

Oxygen Gradients: Oxygen diffuses from capillaries to muscle fibers along oxygen gradients[78,101,102]. Myoglobin, an oxygen-binding protein in muscle, facilitates oxygen diffusion and storage. Factors such as blood flow, capillary recruitment, and myoglobin content affect oxygen delivery to skeletal muscle[78,103].

2.1.6.4 Pathophysiology of Skeletal Muscle Microcirculation in Critical Illness.

Critical illness causes significant disruption in skeletal muscle microcirculation, compromising its ability to function optimally. This disruption causes muscle dysfunction, weakness, and poor outcomes, requiring ICU-level interventions.

Sepsis-Induced Muscle Weakness: Sepsis can cause profound muscle weakness, known as sepsis-induced muscle weakness, due to microcirculatory dysfunction, mitochondrial damage, and impaired protein synthesis[104]. Reduced capillary perfusion and increased endothelial dysfunction limit oxygen and nutrient delivery to muscle fibers, accelerating muscle wasting[64]. Early mobilization and nutritional support are essential components of ICU care to preserve muscle mass and function[105,106].

Multiple Organ Dysfunction Syndrome (MODS): Multiple Organ Dysfunction Syndrome is a common complication of critical illness, which causes the simultaneous dysfunction of multiple organ systems, including the cardiovascular and respiratory systems, which impacts tissue oxygenation[107]. Microcirculatory dysfunction in skeletal muscle contributes to overall metabolic derangement and increased mortality. ICU management focuses on supporting organ function, optimizing oxygen delivery, and controlling inflammation[108].

Prolonged Immobilization: Prolonged bed rest and immobilization in the ICU can lead to muscle atrophy and reduced microvascular density in skeletal muscle[109]. This reduced microcirculation impairs the delivery of oxygen and nutrients, exacerbating muscle weakness and delaying recovery. Early mobilization and rehabilitation programs are crucial for preventing muscle wasting and promoting functional recovery[110].

Critical Illness Polyneuropathy and Myopathy (CIPNM): Critical Illness Polyneuropathy and Myopathy are common in critically ill patients and involve nerve and muscle damage, often linked to microcirculatory abnormalities[111,112]. Reduced capillary perfusion and endothelial dysfunction contribute to nerve and muscle ischemia, leading to weakness and sensory deficits[112]. Management involves careful glycemic control, minimizing exposure to neuromuscular blocking agents, and implementing early rehabilitation strategies[111].

2.1.7 Comparative Overview of Microcirculation Physiology between Brain and Skeletal Muscle

The microvasculature of the brain and skeletal muscle exhibits key structural differences that reflect their distinct functional requirements. In the brain, capillaries are continuous, characterized by tight junctions that form the blood-brain barrier, strictly regulating the passage of substances into the brain. While skeletal muscle capillaries are also continuous, they exhibit a more porous endothelial lining to facilitate rapid nutrient delivery and waste removal during activity[113]. The permeability of skeletal muscle capillaries adapts dynamically to metabolic demands, such as during exercise

Capillary density is high in the brain to meet its constant and high metabolic demands, while in skeletal muscle, capillary density varies depending on fiber type, with oxidative fibers having a richer capillary supply than glycolytic fibers[58].

The regulation of blood flow in the brain and skeletal muscle involves distinct mechanisms tailored to their specific needs. The brain relies on strict and precise cerebral autoregulation to maintain constant blood flow despite fluctuations in blood pressure, while skeletal muscle blood flow is primarily governed by local metabolic control[58,94,114]. While both tissues respond to metabolic signals, the specific factors differ; the brain responds to CO_2, H^+, adenosine, and NO, whereas skeletal muscle responds to adenosine, potassium, and NO[94].

Cerebral autoregulation is primarily governed by myogenic mechanisms, though the autonomic nervous system also contributes to its modulation[115,116]. The influence of sympathetic and parasympathetic innervation on the neurogenic control of cerebral blood flow remains incompletely understood in the current literature[116]. Skeletal muscle microvascular autoregulation is primarily regulated by the sympathetic nervous system[58,95,117].

Functional hyperemia in the brain is mediated by neurovascular coupling, where neuronal activity directly triggers localized vasodilation to match oxygen delivery to metabolic demand. In contrast, skeletal muscle maintains basal perfusion of ~80% of capillaries at rest via continuous RBC flow, even during inactivity[97,98]. During exercise, muscle hyperemia elevates RBC flux and velocity, increasing capillary hematocrit through longitudinal recruitment optimizing oxygen extraction by reducing inter-RBC gaps[97]. This structural reserve allows skeletal muscle to amplify oxygen diffusion capacity without relying on neurovascular signaling, unlike the brain.

Cerebral perfusion pressure (CPP), defined as the difference between MAP and intracranial pressure (ICP), is primarily dependent on MAP to sustain adequate cerebral blood flow within the narrow range governed by myogenic autoregulation[116,118]**.** In contrast, skeletal muscle, the largest organ in the body acts as the main effector of systemic vascular resistance (SVR) through the influence of the sympathetic nervous system[58,95,117]. While MAP serves as the key determinant of CPP, it is itself regulated primarily by the SVR of skeletal muscle under sympathetic control[119]. Thus, although cerebral and skeletal muscle microvascular hemodynamics appear to be independently regulated via distinct autoregulatory mechanisms, the central role of MAP suggests a potential underlying interrelationship between brain and skeletal muscle perfusion that has yet to be fully explored in current literature. Although a study by Mirsajadi et al. demonstrated a moderate correlation between MAPopt values in the brain and skeletal muscle[24], it did not evaluate the physiological coherence of microvascular hemodynamics between the brain and skeletal muscle.

Microvascular dysfunction in the brain and skeletal muscle significantly impacts critical illness, worsening patient outcomes. While current academic literature has focused on organ-specific pathology, the interconnection between brain and muscle microvascular dysfunction in critical illness remains understudied[3,4]. Understanding this relationship is crucial for developing a holistic approach for ICU care and improving patient outcomes. Addressing this knowledge gap could lead to promising approaches for future research and clinical practice in ICU care, such as early treatments and disease management strategies to mitigate microvascular damage, preserve organ function, and enhance long-term outcomes in critically ill patients. Further investigation into this area may reveal new insights for optimizing personalized treatment approaches and patient care in intensive care settings.

2.2 Near-Infrared Spectroscopy (NIRS)

Near-Infrared Spectroscopy (NIRS) is a non-invasive monitoring technology that utilizes[20–22,24] specific infrared wave with wavelengths ranging from 650 to 1000 nm to investigate and monitor molecular compositions and physiological states. The origin and the evolution of NIRS can be traced back to early infrared spectroscopy developments in the 20th century. The 1990s marked a turning point with critical technological advancements that enabled the creation of portable systems capable of real-time monitoring[120,121]. The advancements in portable optics and computational models have enhanced NIRS technology into playing a significant role in real-time monitoring applications across various fields, including biomedical monitoring, agricultural monitoring, and material science[122–124].

2.2.1 Basic Principles of NIRS

The basic operational principles behind NIRS relies on light-matter interactions where near-infrared photons penetrate biological tissues. These photons released from source of NIRS sensor undergo absorption by chromophores and scattering due to cellular structures[125,126]. The scattered light is then captured by the NIRS sensor receiver and analyzed to quantify changes in absorption as a function of wavelength in the NIRS spectrum[127], which correlate directly with the concentrations of specific molecular components in the cellular structures.

The real time measurement of microcirculation in human tissue is achieved by monitoring the real time changes in the concentration of specific chromophores that serve as indicators of microvascular hemodynamics. Blood is composed of red blood cells, white blood cells, platelets, plasma, and various solutes. Among these components, hemoglobin is a key chromophore found exclusively within red blood cells, which exhibit time-dependent variability in human tissues. Thus, this variability makes hemoglobin a valuable marker for assessing microcirculatory function[128,129]. Based on oxygen-binding status, hemoglobin exists in two key chromophore states: O2Hb and HHb. These chromophores exhibit distinct optical absorption characteristics within the NIRS spectrum[126,130]. By quantifying time-dependent changes in the concentrations of O2Hb and HHb, it is possible to infer the dynamic regulation of red blood cell distribution within the microvasculature[129]. Consequently, NIRS-based monitoring of these chromophores provides a non-invasive method for assessing total hemoglobin [02Hb+HHb] concentration, fluctuations reflecting real-time changes in microvascular activity[127].

As 02Hb and HHb are the key chromophores of interest to measure microcirculation in the tissue, NIRS utilize an optical window of wavelengths between 700nm -1000nm [126,130]. This range is particularly significant as it balances tissue penetration capabilities allowing penetration depths of up to 5 cm and minimizes water absorption interference[20].

Apart from the absorption properties of the chromophore of interest, several parameters influence the accuracy and reliability of NIRS measurements[20]. The composition of the organ of interest, characterized by its layered structures/tissues, could alter photon path lengths and scattering properties. The Differential length factor (DPF) is employed to correct for these scattering effects, facilitating more accurate quantification of chromophore concentrations.

To quantitatively interpret the attenuated raw light intensities of NIRS spectrum by distinct absorption characteristics of O2Hb and HHb, mathematical modeling is applied. The Beer–Lambert Law[131,132] provides the theoretical foundation for converting measured light attenuation into meaningful estimates of concentration changes of 02Hb and HHb over time. This relationship is mathematically expressed as,

$$A = \log\left(\frac{I}{I_o}\right) = \varepsilon c l \qquad \text{----- (1)}$$

where A represents attenuation of intensity of transmitted light I_o to intensity of detected light I as a logarithmic ratio, ε denotes molar extinction coefficient, c denotes concentration, and l indicates direct path length between source and detector. However, human biological tissues present limitations due to scattering effects that distort linearity; thus, modified models are often necessary.

To address these limitations, the Modified Beer-Lambert Law[133] incorporates adjustments for wavelength-dependent scattering and DPF,

$$A = \varepsilon c l \cdot DPF + G \qquad \text{----- (2)}$$

where G accounts for scattering coefficient of the tissue and source detector configurations of the sensor. This modified equation enhances accuracy in the oxygenation monitoring by providing a more reliable framework for interpreting NIRS data.

Based on the explained theoretical foundation, different types of NIRS devices are developed utilizing distinct approaches to measure oxygenation and interpret the complex characteristics of absorption and scattering within human tissues[20,22].

Continuous Wave (CW) NIRS: Continuous Wave NIRS employs constant intensity light for measuring attenuation changes in tissue. This method is characterized by its low cost and portable systems that facilitate real-time monitoring; however, it faces limitations regarding semi-quantitative results due to unknown scattering coefficients[134] .

Time-Resolved Spectroscopy (TRS) NIRS: Time-Resolved Spectroscopy utilizes photon time of flight measurements to compute absolute absorption and scattering coefficients. This technique allows for depth resolved analysis of brain tissue oxygenation, enhancing its clinical utility in neuroimaging applications[134].

Spatially Resolved Spectroscopy (SRS) NIRS: Spatially Resolved Spectroscopy NIRS utilizes the fundamental CW NIRS principle with a single light source and multiple source-detectors to obtain multiple source-detector distances. Based on the spatial distribution of the attenuated light, SRS NIRS calculated the relative concentrations of chromophores: O2Hb and HHb. SRS NIRS is one of the widely used NIRS device systems as it provides high-time resolution with better Signal-to-noise ratio(SNR) and a technically simpler setup than TRS NIRS[135].

Frequency-Domain (FD) NIRS: Frequency-Domain NIRS operates by modulating light intensity at high frequencies ranging from 50 to 1000 MHz to resolve optical properties more effectively. FD-NIRS can measure the absolute concentration of total hemoglobin in tissue. This ability to provide absolute, rather than just relative, hemoglobin measurements significantly enhance the clinical applicability and accuracy of FD-NIRS. Recent advancements in digital parallel acquisition systems have significantly improved both the speed and accuracy of this method[134,136].

2.2.2 Applications of NIRS in Health and Biomedical Research

Due to its non-invasive nature and ability to provide high-resolution, real-time monitoring of microvascular hemodynamics, NIRS has found broad applications in health and biomedical research. The compact sensor design and portability of NIRS further facilitate ease of use across various anatomical sites. These features of NIRS sensors have contributed to its growing application in critical care settings, where continuous, localized microvascular hemodynamics monitoring is vital for assessing patient status, deriving biomarkers, and guiding therapeutic interventions.

NIRS has been extensively utilized to monitor skeletal muscle microcirculation in ICU patients, providing real-time insights into microvascular hemodynamics. A meta-analysis by Neto et al. demonstrated that lower baseline StO_2 and slower reperfusion in septic patients correlate with increased mortality, supporting the use of thenar muscle StO_2 measurement as a prognostic tool[137]. Collet et al. showed that skeletal muscle StO_2 responds rapidly to fluid resuscitation, often preceding systemic hemodynamic changes[138]. Samraj et al. demonstrated the feasibility of using NIRS to assess thenar oxygen saturation during the Vascular Occlusion Test in pediatric patients, enabling the detection of microcirculatory impairment in children with heart failure[139]. More recently, Mirsajadi et al. introduced a novel method using NIRS to derive skeletal muscle-specific optimal mean arterial pressure in ICU patients, enabling personalized blood pressure targets based on microvascular autoregulation[24]. Altogether, these applications illustrate the utility of NIRS-based microvascular monitoring in skeletal muscle for the early detection of microvascular dysfunction and individualized hemodynamic management in critical care.

Similarly, NIRS has been extensively employed for cerebral microvascular hemodynamics monitoring in the ICU. It has proven particularly useful in critically ill patients, such as those with traumatic brain injury (TBI), by enabling continuous tracking of cerebral oxygenation and autoregulation. This facilitates the early detection of secondary brain injuries and supports timely interventions[140,141]. Studies have shown that cerebral biomarkers, such as cerebrovascular reactivity, can be derived from NIRS-based regional oxygen saturation measurements and used as clinical indicators to evaluate cerebral autoregulation[142–144]. Rivera-Lara et al. further demonstrated that NIRS-derived cerebral oximetry index (COx) values are associated with increased mortality in neurocritical patients[145]. These findings underscore the value of cerebral NIRS in guiding individualized cerebral hemodynamic targets, thereby enhancing the precision and responsiveness of neurocritical care. Although many studies have focused on organ-specific microvascular hemodynamics monitoring using NIRS-derived clinical indicators and utilizing it as a prognostic tool, very few studies have explored simultaneous multi-site NIRS monitoring[24,146]. However, these limited studies did not evaluate simultaneous microvascular monitoring of the brain and skeletal muscle, nor did they evaluate the time-frequency relationships between microvascular hemodynamics across these organs. These factors highlight a distinct knowledge gap that should be further explored.

2.3 Digital Signal Processing: Overview

2.3.1 Overview of Time-Frequency Analysis

In the field of Digital Signal Processing, time-frequency analysis has been deeply explored in the research literature [147,148]. The time-frequency representation of signals enables the examination of dynamic and transient characteristics, including frequency, amplitude, phase, and correlation values. Time-frequency analysis allows for both global and local assessments of the signal with respect to time and frequency, providing a comprehensive understanding of the signal behavior[149,150].

Naturally occurring signals that are a function of time exhibit unique transient characteristics[151]. In the context of this study, Physiological signals: Near-Infrared Spectroscopy (NIRS) and Arterial Blood Pressure (ABP) are inherently non-stationary in nature and reflect dynamic and transient physiological states and responses of the human body[152–156]. Therefore, these dynamic and transient characteristics of physiological signals needed to be evaluated with higher resolution in both time and frequency domains to assess the underlying physiological processes. Such analyses are critical for evaluating complex interactions within human physiological systems and achieving a clear and accurate understanding of underlying human physiological processes.

The next sections will discuss fundamental methodologies for analyzing the frequency domain of signals and their extensions of time-frequency analysis and the time-frequency analysis representations of signals. Subsequently, the discussion will focus on the utilization of the application of time-frequency analysis to evaluate the similarities and relationships between two time series signals.

2.3.2 Fourier Transform Analysis

Fourier transform is a mathematical tool introduced by Joseph Fourier[157] for decomposing signals into an infinite but discrete set of harmonic components. Fourier transform[158] of a function of time $f(t)$ or a signal defined by,

$$f(\omega) = \int_{-\infty}^{\infty} f(t) \mathrm{e}^{-\mathrm{i}\omega \mathrm{t}}\, \mathrm{dt} \qquad \text{----- (3)}$$

where $f(\omega)$ is a function of frequency and $f(t)$ is stationary and continuous the signal. In Fourier transform analysis, it measures the circular frequency ω of $f(t)$ and transforms the time domain

function into the frequency domain function. Fourier transform produces the Fourier spectrum, which reveals information about all the frequencies in $f(t)$ and their respective intensities.

In spite of its effectiveness as a mathematical tool for analyzing the frequency spectrum of continuous stationary signals, Fourier analysis has two significant drawbacks. Firstly, the Fourier transform is not suitable for analyzing non-stationary signals, which are prevalent in most real-world scenarios. This limitation limits the applicability of Fourier analysis for signals like NIRS and ABP. Secondly, the Fourier transform provides only a global representation of frequency information, lacking local details that reflect changes in signals over time and frequency.

To address these drawbacks, the Short-Time Fourier Transform (STFT)[159–162] was introduced as an extension of the Fourier transform. The STFT analyzes the frequency content of a signal within a specific time window, denoted by $w(u)$. In mathematical expression[163] $w(u-t)$ represents the shifting of the time window function to a specific time *t* of the signal. The Short-Time Fourier Transform of a function $f(t)$ is represented as $\mathrm{F}(\omega, t)$ where ω denotes the frequency at time *t* of the time window $w(u-t)$ for the original signal. This approach allows for a more detailed examination of how frequency components evolve over time, making it particularly useful for analyzing non-stationary signals.

$$\mathrm{F}(\omega, \mathrm{t}) = \int_{-\infty}^{\infty} \mathrm{x}(\mathrm{u})\mathrm{w}(\mathrm{u}-\mathrm{t})\mathrm{e}^{-\mathrm{j}\omega\mathrm{u}}\mathrm{du} \qquad \text{----- (4)}$$

Although the STFT provides localized information about the frequency content at a specific time *t*, its time-frequency resolution depends on the size of the time window function $w(u)$. According to the Heisenberg uncertainty principle[164] , a longer time window (which corresponds to signal content with longer wavelengths) results in higher frequency resolution but reduces time resolution. In contrast, a shorter time window (which corresponds with shorter wavelengths) gives higher time resolution at the expense of frequency resolution.

The relationship between time and frequency resolution can be expressed by the Heisenberg uncertainty principle, which states:

$$\Delta\mathrm{t} \cdot \Delta\mathrm{f} \geq \frac{1}{2} \qquad \text{----- (5)}$$

where Δt represents the uncertainty in time and Δf represents the uncertainty in frequency.

Since the window function used in STFT is non-adaptive and fixed, it limits the ability to achieve a microscopic time-frequency analysis of a signal. Therefore, depending on the application requirements, methodologies that provide improved time-frequency resolution should be considered if needed.

2.3.3 Introduction to Wavelet Analysis

Physiological signals are, in general, non-stationary. Therefore, a mathematical tool with adaptive microscopic zooming capabilities that measure both dynamics and transient characteristics on both local and global scales is required to analyze these non-stationary signals with higher time-frequency resolution.

Jean Morlet, a French Geophysicist and engineer, introduced "*Wavelet transform*"[165,166], which provides a mathematical tool designed to analyze and capture high-frequency transient and low-frequency components in signals with higher time-frequency resolution. Wavelet transform is based on a family of waveform functions named '*wavelets*' generated from the translation and dilation of a base waveform function named "*Mother Wavelet* $\psi_{a,b}(t)$." The Wavelet function is defined by,

$$\psi_{a,b}(t) = \frac{1}{\sqrt{|a|}}\psi\left(\frac{t-b}{a}\right), \quad a, b \in R, \quad a \neq 0 \qquad \text{----- (6)}$$

In this mathematical expression (Eq. 6) of the wavelet function, a is defined as the scaling parameter, which measures the ratio of stretching or expansion of the scale relative to the Mother wavelet, and translation parameter b determines the time location of the wavelet in the signal. When the mother wavelet is stretched, the family of wavelet functions having $|a| < 1$ corresponds to higher frequencies. In contrast, when the mother wavelet is expanded, where wavelets with $|a| > 1$ correspond to lower-frequency components. Thus, this adaptive scaling capability of the wavelets enhances the zooming of frequencies to analyze signals with higher time-frequency resolutions. Although the time-frequency resolution of wavelets is still constrained by the Heisenberg uncertainty principle, this adaptive scaling of wavelets provides a fine-tuned time-frequency representation.

To qualify as a wavelet function, it must satisfy the "*admissibility conditions*", which includes two key requirements:

1. *Zero Mean*: The average value of the wavelet function must be zero.
2. *Unit Energy*: The total energy of the wavelet function should be normalized to one.

These conditions ensure that the wavelet can effectively analyze signals without introducing bias or distortion.

2.3.4 Wavelet Transform

The wavelet transform is defined as the convolution operation between a time-domain function $f(t)$ (such as a physiological signal) and scaled and translated versions of the mother wavelet $\psi_{a,b}(t)$. There are two primary forms of wavelet transforms: the Continuous Wavelet Transform (CWT) and the Discrete Wavelet Transform (DWT).

The CWT provides a continuous representation of the signal across all scales and translations, while the DWT employs a discrete set of scales and translations, resulting in a more compact representation. The mathematical formula for the continuous wavelet transform of a function $f(t)$ is given by:

$$W_\psi f(a,b) = \frac{1}{\sqrt{|a|}} \int_{-\infty}^{\infty} f(t)\psi^*\left(\frac{t-b}{a}\right) dt \qquad \text{----- (7)}$$

Where $W_\psi f(a,b)$ is the wavelet transformation of $f(t)$ and ψ^* is the complex conjugate of the wavelet function.

For the discrete wavelet transform, the coefficients can be represented as:

$$c_{jk} = W_\psi f\left(2^{-j}, k2^{-j}\right) \qquad \text{----- (8)}$$

where *j* and *k* are integers representing the level of decomposition and position, respectively.

2.3.4.1 Wavelet function

The characteristics of signals that can be captured and analyzed from wavelet transforms depend significantly on the type of wavelet function used[167–170]. There are several factors that should be considered when selecting a wavelet function for wavelet analysis [149,171].

I. **Real wavelets or Analytical Wavelet :** Real valued wavelet functions with zero average that can capture various features such as discontinuities and sharp spikes in signals. On the other hand, Analytical wavelets are complex valued functions whose Fourier transforms

are supported only on the positive real axis. They are particularly useful for analyzing modulated signals and can provide phase information along with amplitude and frequency, making them effective for applications such as time-frequency analysis in biomedical signal processing.

II. **Orthogonal or Non-orthogonal:** Orthogonal wavelet transform provides compact and rigid representation of signal while Non-orthogonal analysis provides smooth and continuous variation in wavelet representation. Thus, making Non-orthogonal wavelets are best suited for time-domain functions.

III. **Shape of Wavelet function waveform:** The waveform of the Mother wavelet function should closely resemble the features and characteristics of the signals it is intended to analyze, as the similarity of shape of wavelet function enhances the effectiveness of wavelet analysis by giving highly accurate interpretation of the signal's properties.

As explained above, an analytical wavelet like the *Morlet* wavelet, is better suited for analyzing physiological time series signals (such as NIRS) compared to the *Haar* wavelet. The *Morlet* wavelet with its complex and non-orthogonal properties able to capture oscillatory patterns present in physiological signals allows for a more accurate representation of frequency, amplitude, and phase characteristics.

2.3.4.2 Wavelet Based Approach of Comparative Analysis of Non-Stationary Time Series

Comparative analysis of time series signals reveals the associations and relationships between the processes that generate these time series. In the case of stationary time series, global statistical measures can effectively analyze these associations, relationships, and similarities between processes. However, a higher-dimensional spare representation of the data is required for non-stationary time series to extract and analyze the associations, relationships, and similarities between the processes that generate signals[172,173]. For example, physiological signals generated from different organs can reflect unique non-stationarity characteristics due to various internal and external factors[174]. Therefore, understanding the comparative analysis of these signals could evaluate the inter-relationships and associations between those organs.

Statistical methods such as covariance[175,176], cross-correlation[177], Dynamic Time Warping (DTW)[178,179], and Piecewise Aggregate Approximation (PAA)[180] can be utilized for comparative analysis between two signals. However, methods like cross-correlation, DTW, and PAA are

inadequate for identifying similarities at the same time point in two-time series, as their calculations are based on shifted signals. While covariance can reveal the relationship between two signals, it only provides information in the time domain without any time-frequency representation.

To conduct a meaningful comparative analysis of two time series in the time-frequency domain, it is essential to incorporate time-frequency representations of the signals. As discussed in earlier sections, Fourier analysis and wavelet analysis are better candidates for this purpose. Wavelet analysis, in particular, offers superior time-frequency representation. Thus, the following section will focus on the comparative analysis of two signals using wavelet-based approaches.

2.3.4.3 Cross-Wavelet Transform

The cross-wavelet transform, introduced by Liu et al.[181] evaluates the covariance between two time series signals in the time-frequency spectrum. The cross-wavelet transformation is defined as follows:

$$\mathrm{W_{XY}(s) = X(s) \cdot Y(s)^*} \qquad \text{----- (9)}$$

where $W_{XY}(s)$ denotes the cross-wavelet coefficients, and $X(s)$ and $Y(s)$ are the wavelet coefficients of the time series signals $x(t)$ and $y(t)$ using the same mother wavelet. The $Y(s)^*$ denotes the complex conjugate of $Y(s)$. The cross-wavelet transform provides a time-frequency representation similar to wavelet power, and it is required that the same mother wavelet is used for the wavelet transformation of both time series signals $x(t)$ and $y(t)$. Depending on whether the chosen mother wavelet is real or analytic, the cross-wavelet transformation will be complex or real. If the cross-wavelet transform is complex, its absolute value $|W_{XY}(s)|$: Cross-wavelet power (Eq. 9) or its squared absolute value (Eq. 10) are typically used for visualization and analysis[171,182].

$$\left|W_{xy}(S)\right|^2 = |X(S) \cdot \mathrm{Y}(S)^*|^2 \qquad \text{----- (10)}$$

A significant value in $|W_{XY}(s)|$ occurs when the two-time series signals $x(t)$ and $y(t)$, exhibit higher energy at the same frequency and at the same time. Similar to covariance in the time domain, the cross-wavelet transform captures this combined energy dynamics of the non-stationary time series in a time-frequency representation. The local phase difference between the two signals does not impact these transient energy characteristics.

2.3.4.4 Wavelet Semblance

The phasic relationship between two-time series gives insight into the inter-dependency of these time series signals. Extracting these phasic relationships between time series in time-frequency representation gives a better understanding of the signals and their underlying processes. The local phase θ of a complex $W_{xy}(S)$ is given by its argument[171,181].

$$\theta = \arg\left(W_{xy}(S)\right) = \tan^{-1}\left(\frac{\mathrm{Im}\left(W_{xy}(S)\right)}{\mathrm{Re}\left(W_{xy}(S)\right)}\right) \qquad \text{----- (11)}$$

The local phase θ, as defined by (Eq. 11), measures the phasic relationship between two-time series in a time-frequency representation, with values ranging from $-\pi$ to $+\pi$. To achieve a standardized numerical measure of this phasic relationship with improved resolution, the Wavelet Semblance[183] $WS(S)$ (Eq. 12) was introduced.

$$WS(S) = \cos^{n}(\theta) \qquad \text{----- (12)}$$

In this equation, n represents a non-zero odd integer ($n > 1$). Higher values of n increase the resolution and sensitivity of the semblance measure, with values of +1 indicating a correlated relationship, 0 indicating no correlation, and -1 indicating an inversely correlated relationship.

However, since wavelet energy information does not account for the local phase relationship, wavelet semblance provides a standardized, energy-independent measure between two signals. Nonetheless, the absence of wavelet energy data can introduce noise sensitivity in wavelet semblance. Therefore, (Eq. 13) provide formula incorporating wavelet energy can enhance the analysis by providing a time-frequency representation that reflects both local phase relationships and local energy[183].

$$\mathrm{D(S)} = \left|\mathrm{W_{xy}(S)}\right|.\cos^{\mathrm{n}}(\theta) \qquad \text{----- (13)}$$

2.3.4.5 Wavelet Coherence

Although cross-wavelet transformation provides a co-variance of wavelet energy between two-time series in time-frequency representation, it does not reflect normalized local energy dynamics with respect to the time-frequency spectrum.

Normalization of the cross-wavelet transform provides a measure similar to the normalized correlation coefficient between two-time series. This normalization accounts for sample size, meaning it utilizes data points from the time-frequency spectrum of the cross-wavelet transform coefficients. The normalization process of the cross-wavelet transform, known as Wavelet Coherence[171,181,184] $WC(s)$, is defined as the squared absolute value of the smoothed time-frequency spectrum of the cross-wavelet transform for time series signals $x(t)$ and $y(t)$, normalized by their respective smoothed wavelet power spectrums. The mathematical expression for Wavelet Coherence is given by,

$$\mathrm{WC(s)} = \frac{|\langle \mathrm{W_{XY}(s)} \rangle|^2}{\langle |\mathrm{W_X(s)}|^2 \rangle \langle |\mathrm{W_Y(s)}|^2 \rangle} \qquad \text{----- (14)}$$

In this equation, $\langle \cdot \rangle$ indicates smoothing in both the frequency and time domains. In the numerator, the cross-wavelet transformation is smoothed in both the real and imaginary components before taking its absolute value. For the denominator, the smoothing operation is applied after calculating the absolute wavelet power spectra. Since the cross-wavelet transform preserves covariance properties[181,184]**,** Wavelet Coherence is an accurate representation of the coefficient of determination[181,182,184] (R^2) for linear relationships in the time-frequency domain between two-time series signals.

As Wavelet coherence is a normalized measure, its value ranges from zero to one. In a given time-frequency space of two-time series, a value of zero indicates no linear relationship, while a value of one signifies perfect linear coupling. Values between zero and one represent varying degrees of linear relationship, with the specific value indicating the strength of the coupling.

2.3.4.6 Significant Analysis for Wavelet Coherence and Wavelet Semblance

Significance testing is crucial for interpreting results from wavelet analysis because it helps to distinguish meaningful relationships from random noise. In many cases, seemingly large peaks in wavelet-based quantities can be mere artifacts of randomness[171,182]. Therefore, significance tests establish a basis for accepting or rejecting a result with a degree of confidence. The null hypothesis (H0) for significance tests in this context is often based on the statistically significant thresholds generated using Monte Carlo simulations with red noise models[171]. This involves generating a large number of surrogate datasets, which mimic the statistical properties of the original time series, specifically using an autoregressive AR(1) process to account for red noise characteristics.

By calculating wavelet-based quantities like wavelet coherence across these surrogate datasets and comparing them to the original data, it can derive significance levels based on the distribution of wavelet-based quantities' values from the surrogates. Typically, around 1000 surrogate pairs are generated to ensure robust estimates of significance levels, allowing researchers to ascertain where the observed values of wavelet-based quantity exceed what would be expected by chance alone.

The phase angle of the cross-wavelet transform, which represents the local phase difference between two time series at a given scale and time, is uniformly distributed for two independent Gaussian noise series[185,186]. This uniform distribution means that the phase angle is scattered across the entire range of ($-\pi$, $+\pi$) without concentrating around any particular value[187]. Because of this, it is not possible to establish significance levels for the phase angle itself [185]. In other words, it's difficult to determine if an observed phase angle is meaningful or simply due to random chance[187]. Due to this issue the significance test of the wavelet-based quantity like wavelet coherence acts as a proxy for assessing the meaningfulness of phasic relationship measures like wavelet semblance between two time series signals. This approach helps to identify genuine physical relationships between time series while disregarding random fluctuations[188].

2.3.5 Application of Wavelet Analysis in Physiological Time Series data

Wavelet analysis has emerged as a powerful mathematical tool for time series analysis, offering a high-resolution, multi-scale framework that effectively addresses the limitations of conventional approaches such as the Fourier Transform and Short-Time Fourier Transform. Unlike these traditional methods, which assume signal stationarity and provide limited temporal resolution, wavelets are inherently well-suited for analyzing non-stationary data. They enable the detection of transient phenomena, the characterization of localized non-stationarities, and the tracking of evolving frequency components over time. This ability to achieve precise time-frequency localization is particularly vital when analyzing real-world signals, where dynamic and irregular changes in signal properties are common.

Applications of wavelet analysis on time series gained widespread attention when Torrence and Compo et al. introduced wavelet analysis as a robust methodology for evaluating climate variability across multiple time scales in geoscience[171], with an emphasis on practical applications and a step-by-step guide for the utilization and quantification of wavelet analysis in the time series analysis. Building on this foundation, Grinsted et al. demonstrated the utility of wavelet-based

techniques particularly cross-wavelet, wavelet semblance, wavelet coherence measures for analyzing co-variability and dynamic interdependencies among geophysical signals[189]. These methodological advancements have been instrumental in uncovering cyclic, periodic, and coupled behavior in complex geoscientific datasets. Thus, the successful application of wavelet analysis in geoscience has catalyzed its adoption in various other research domains, notably within the biomedical and health sciences research.

Wavelet analysis has emerged as a powerful mathematical tool for analyzing physiological time series data, particularly in critical care settings as wavelets provide superior time-frequency resolution for non-stationary signals like NIRS and ABP, making them ideal for capturing the dynamic nature of bio-physiological processes.

Highton et al. demonstrated the application of wavelet analysis to assess cerebral autoregulation in brain injured patients under intensive care. Their study employed wavelet transform to examine the dynamic relationships between spontaneous oscillations in mean arterial pressure and cerebral tissue oxygenation saturation, identifying time-scale dependent nature of cerebral autoregulation that correlated with neurological outcomes[27]. This multimodal approach enabled the detection of cerebrovascular reactivity that might be missed using conventional spectral analysis.

Similarly, Garg et al. applied wavelet coherence analysis to investigate the physiological interdependence between cardiovascular and postural control systems under orthostatic stress[190]. Their innovative application revealed previously unrecognized dynamic interactions between blood pressure regulation and postural sway, demonstrating the interplay between the cardiovascular and postural systems while maintaining the homeostasis under orthostatic challenge. The wavelet-based methodology was crucial for uncovering these relationships as it allowed for the characterization of oscillatory components across a wide frequency range (0.01-0.1 Hz), capturing both rapid and slow regulatory processes.

In the context of neuromonitoring in ICU settings, Tian et al. employed wavelet coherence to assess regional differences in cerebral hemodynamics and autoregulation in neonates with mild encephalopathy[25,26]. Their studies have demonstrated that frontal-posterior heterogeneity in cerebral hemodynamics in neonates with mild encephalopathy, revealing regional differences in pressure autoregulation despite having intact global cerebral autoregulation[25]. This spatial heterogeneity would be difficult to detect using traditional spectral analysis methods, highlighting

the value of wavelet-based approaches in capturing the complex spatiotemporal dynamics of cerebral physiology.

Hermans et al. applied wavelet coherence analysis to assess neurovascular coupling in neonates with hypoxic-ischemic encephalopathy by removing the confounding effects of arterial oxygen saturation when analyzing the relationship between EEG and regional cerebral oxygen saturation[191]. Their findings showed that decreased neurovascular coupling was associated with worse MRI outcomes.

Wavelet analysis has also proven valuable in identifying early markers of patient deterioration in critical care settings. The ability to detect subtle changes in physiological signal patterns that precede clinical deterioration offers the potential for earlier intervention. As demonstrated by Bernjak and Stefanovska in their analysis of laser Doppler flowmetry signals, wavelets enable the resolution of oscillatory components at different time scales simultaneously, providing insights into the complex dynamics of microvascular blood flow that could indicate impending cardiovascular instability[192].

The application of these wavelet-based techniques has significantly advanced our understanding of complex physiological interactions in critical care settings, offering potential for advancing personalized care and improving clinical outcomes in critically ill patients.

2.4 Review of literature on evaluating Physiological coherence of microvascular hemodynamics between brain and skeletal muscle.

Current literature demonstrates significant advancements in microvascular hemodynamics as a critical factor in tissue oxygenation and organ dysfunction during critical illness, yet studies remain substantially focused on organ-specific parameters rather than systemic coordination[15,16,18,23]. While studies using hr-NIRS have established prognostic value for cerebral (rSO_2) and skeletal muscle (StO_2) oxygenation metrics independently[15–19], the physiological coherence of microvascular hemodynamics between these systems defined as their synchronized hemodynamic behavior remains poorly characterized. Notably, no studies have systematically evaluated time-frequency relationships or dynamic coupling between brain and skeletal muscle microcirculation despite their distinct autoregulatory mechanisms and shared dependence on systemic blood pressure[193].

Existing studies of the physiological coherence of microvascular hemodynamics have primarily examined either intra-organ synchrony (e.g., between cerebral regions) or isolated correlations with macro-hemodynamic variables like MAP[23,25–27]. While Mirsajadi et al. demonstrated technical feasibility in deriving organ-specific MAPopt values from hr-NIRS, their study did not analyze time-frequency coherence dynamics between organs or assess how these relationships differ across populations[24]. Furthermore, advanced signal processing methods like wavelet coherence and wavelet semblance, which were successfully applied to study neurovascular coupling and cardiovascular interactions, have not been extended to evaluate brain-skeletal muscle microvascular coordination[23,25–27,194,195].

Despite these technological and methodological advances, a critical knowledge gap persists in the literature regarding evaluating physiological coherence of microvascular hemodynamics between brain and skeletal muscle with cross-population comparisons. To date, no studies have directly contrasted patterns of brain–skeletal muscle microvascular coherence between ICU patients and healthy controls or between ICU survivors and non-survivors. This notable omission significantly limits the clinical translation of coherence metrics, as the altered brain–skeletal muscle microvascular coherence may serve as an early indicator of systemic microvascular dysregulation that precedes either the onset of organ failure or subsequent recovery. Additionally, although

organ-specific microvascular hemodynamic metrics currently demonstrate reliable indicators of patient outcome, the potential utility of brain–skeletal microvascular coherence as a biomarker for personalized hemodynamic management remains unexplored. Addressing this gap could provide crucial insights for guiding individualized interventions during critical illness, thereby improving patient outcomes.

2.5 Conclusion of Literature review and Rationale for Thesis

Considering the hypotheses and objectives outlined in the Introduction chapter, it is crucial to emphasize the current literature-based understanding of the physiological connection between cerebral autoregulation and the autoregulatory mechanisms of skeletal muscle microcirculation. Cerebral perfusion pressure and cerebral blood flow are tightly regulated by cerebral autoregulation, with MAP as the primary determinant. Importantly, MAP is predominantly governed by systemic vascular resistance of skeletal muscle under sympathetic nervous system control. Therefore, changes in skeletal muscle microvascular resistance can directly alter MAP, subsequently affecting CPP and engaging cerebral autoregulatory mechanisms. This cascade establishes a directional physiological link wherein systemic blood pressure acts as the central hemodynamic intermediary between cerebral and peripheral microcirculatory dynamics.

Both the brain and skeletal muscle depend on precisely regulated microcirculation to maintain adequate oxygen and nutrient delivery. In the brain, microcirculation is characterized by a high capillary density and precise autoregulatory control, which protects brain function from fluctuations in blood pressure. In contrast, skeletal muscle microcirculation exhibits dynamic microvascular adaptations responsive to metabolic demand, particularly during exercise or critical illness. Despite these distinct regulatory strategies, both brain and skeletal muscle microvascular hemodynamic mechanisms are vulnerable to systemic hemodynamic disturbances, highlighting the critical importance of coordinated blood flow regulation and microcirculatory integrity across organ systems.

Blood flow and microcirculation in both the brain and skeletal muscle can be non-invasively assessed through surrogate measures of total hemoglobin variation using high-resolution Near-Infrared Spectroscopy. hr-NIRS quantifies real-time changes in O2Hb and HHb concentrations, providing a direct index of microvascular blood volume and tissue oxygenation. Thus, hr-NIRS

technology enables simultaneous monitoring of microcirculatory dynamics in the brain and skeletal muscle, alongside systemic blood pressure, facilitating the evaluation of inter-organ physiological coherence of microvascular hemodynamics in both healthy and disease states.

Advanced signal processing techniques, particularly wavelet-based metrics such as wavelet coherence and wavelet semblance, provide high-resolution mathematical approaches for analyzing the time-frequency and time-phasic relationships between these physiological time series. These analysis provide quantification of both the strength and synchrony of microvascular coupling, capturing dynamic and transient interactions that are not discernible with traditional analyses. By applying these approaches, it becomes possible to interpret the underlying causal and temporal relationships between brain and skeletal muscle microcirculation and their coupling with systemic blood pressure.

While recent advances in non-invasive monitoring and signal processing have expanded our ability to assess microvascular hemodynamics in both healthy and critically ill populations, all previous literature lacks the understanding of the physiological coherence of microvascular hemodynamics between the brain and skeletal muscle, as well as cross-population comparisons of this physiological coherence. This represents a critical knowledge gap due to the lack of comprehensive, cross-population studies into how brain and skeletal muscle microvascular hemodynamics are coordinated and how these interactions may differ between health and disease states. Therefore, addressing this gap could yield critical insights for individualized interventions during critical illness and improve patient outcomes.

To address this gap, this thesis leverages advanced wavelet-based metrics, wavelet coherence, and wavelet semblance to analyze time-frequency and phase relationships among physiological signals from the brain, skeletal muscle, and systemic blood pressure. This approach enables rigorous testing of the following hypotheses:

- **HYPOTHESIS # 1.1: The physiological coherence of microvascular hemodynamics between the brain and skeletal muscle, and with systemic blood pressure, is significantly altered in ICU patients compared to healthy controls.**

- **HYPOTHESIS # 1.2: The ICU non-survivors exhibit significantly altered physiological coherence of microvascular hemodynamics between the brain and skeletal muscle and with systemic blood pressure, compared to ICU survivors.**

Thus, this thesis enables the quantification and comparison of dynamic brain-skeletal muscle microvascular interactions and their association with systemic blood pressure across critically ill and healthy populations, providing a robust framework for identifying novel biomarkers and advancing personalized hemodynamic management in critical care.

3 CHAPTER 3 - METHODOLOGY

3.1 Study Details

This prospective observational cohort study was conducted with recruitments from ICU patient populations and Healthy participants.

3.1.1 ICU patients

Recruitment of ICU patients was conducted at the adult Medical and Surgical ICUs of Health Science Centre, Winnipeg from May 2023 to June 2024. All research procedures and protocols for ICU patient recruitment were approved by the Shared Health Approval Committee SH2021-147 (November 21, 2021), and by the University of Manitoba, Biomedical Research Ethics Board HS25043 (September 15, 2021), for the study entitled "MIMICSS: Microvascular Monitoring in Circulatory Shock in Sepsis: Longitudinal Observational Cohort Study" in accordance with the Declaration of Helsinki; the study was registered at clinicaltrials.gov (NCT05985525).

Critically ill adult ICU patients were enrolled for this study within 24 hours of ICU admission if they were mechanically ventilated and had a Body Mass Index (BMI) <= 40. Due to the non-invasive nature of the study, microvascular perfusion monitoring of the eligible patients started with deferred consent. Written informed consent was obtained from the substitute decision maker of the patient or directly from the patient if they regained consciousness in the ICU. ICU patient monitoring was done in Days 1, 3, and 8 of their ICU stay. Patient demographics, medical history, and laboratory results were collected from the electronic health record and patient chart.

Healthy participants were recruited from the general population of Winnipeg between May 2024 and July 2024. The inclusion criterion of a BMI of 40 or lower was established to minimize variability among comparative populations of ICU patients. All research procedures and protocols for the recruitment and data collection of these healthy participants were approved by the University of Manitoba Health Research Ethics Board approval HE2022-0058(March 31, 2023; amendment approved February 12, 2024). Written informed consent was obtained from the healthy participants before the data collection started. In addition to microvascular monitoring, participant demographics, medical history, laboratory values, and resting status (sleeping or awake for healthy participants) of the monitoring period were recorded.

3.2 Study Design

3.2.1 Microvascular Monitoring

This study used high-resolution Near-infrared spectroscopy devices to monitor microvascular perfusion by measuring changes in the concentration of Oxy-hemoglobin(O2Hb), Deoxy-hemoglobin (HHb), and Total hemoglobin (HbT), as well as the Tissue Saturation Index (TSI) of skeletal muscle and brain. All NIRS signals are recorded continuously at 10 Hz.

Microvascular Hemoglobin Content (MHC), introduced by Mendelson et al [129], represents the total amount of hemoglobin contained in the red blood cells in the tissue microcirculation illuminated by the NIRS system. Technically MHC is equivalent to HbT and the time-dependent variability of this metric reflects the dynamic nature of hemoglobin distribution regulation within microcirculation. Thus, this study used HbT variability as the primary hemodynamic metric for monitoring microvascular perfusion in the ICU.

Microvascular perfusion monitoring of skeletal muscle and brain is done using two types of NIRS sensors. As illustrated in Figure 3.1, PortaMon (Artinis Medical Systems, Netherlands) NIRS

Figure 3.1: Demonstration of the hr-NIRS setup

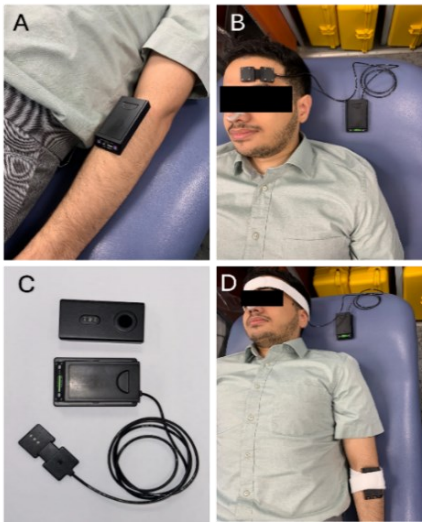

Demonstration of the hr-NIRS setup: (A) PortaMon applied to the brachioradialis; (B) PortaLite applied to the forehead (frontal cortex); (C) both systems shown with source-detector configurations; (D) both systems applied with straps to secure their placement. This figure is adapted with permission from Mirsajadi A, et al. Microvascular Autoregulation in Skeletal Muscle. Critical Care Explorations 6(7):p e1111, July 2024. | DOI: 10.1097/CCE.0000000000001111

sensor was placed on the Brachioradialis of skeletal muscle; PortaLite (Artinis Medical Systems, Netherlands) NIRS sensor was placed on the frontal cortex 3-4 cm above the eyebrow

(i.e. frontal cortex)[24]. The differential path length of NIRS sensors was configured based on the organ they were used to monitor; for the skeletal muscle, DPF is set to 4.0 and for the frontal cortex, DPF value was set according to the recommended values by the manufacturer based on the literature [196]. The sampling frequency of both hr-NIRS sensors was set at 10 Hz to monitor rapid dynamic changes in microvascular blood flow and hemoglobin distribution with high temporal resolution. These hr-NIRS sensors utilize the spatially resolved spectroscopy technique using three light transmitters (30, 35. 40 mm) and one receiver configuration where each pair of transmitter-receiver measures relative changes in O2Hb, HHb and HbT. The 40 mm distance between transmitter and receiver was used for HbT to maximize the tissue penetration depth of the NIRS signal. Utilizing three transmitter-receiver configuration allows the approximation of the tissue scattering coefficient and the calculate the TSI with absolute values of O2Hb, HHb.

Figure 3.2 shows a diagram of the microvascular monitoring instrumentation setup for ICU patients. In this system, sensor readings of NIRS sensor devices were transmitted through Bluetooth in real-time into OxySoft (Artinis Medical Systems, Netherlands), a software designed for NIRS data analysis and recording. Concurrently, Arterial Blood Pressure (ABP) was measured using an invasive arterial catheter, calibrated to the right atrium's reference point as per standard care procedures. This ABP data was continuously acquired from the bedside monitor into the recording computer using a DT9804 (Data Translation, Marlboro, MA) data acquisition module at a sampling rate of 100 Hz. NIRS data were extracted in real-time from OxySoft through the Lab Streaming Layer (LSL) [197] and aggregated and recorded with ABP physiological data series at 100 Hz in ICM+ software (Cambridge Enterprises, Cambridge, United Kingdom). The recording sampling rate at ICM+ software was set at 100 Hz in order to accommodate the sampling rate of ABP. Before initiating the microvascular monitoring, the finger capillary refill test was conducted on each patient, and the tissue thickness of the brachioradialis muscle was measured using the standard ultrasound and linear probe (Sonosite, Toronto, ON, Canada).

Figure 3.2: Microvascular Monitoring Instrumentation Setup for ICU patients

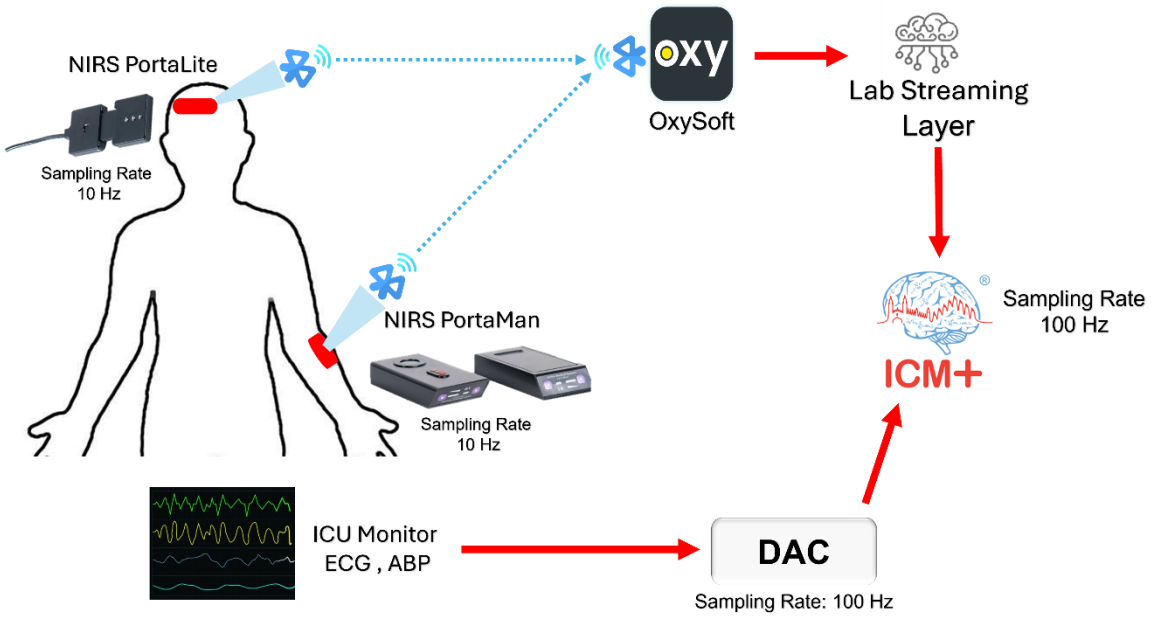

Microvascular Monitoring Instrumentation Setup for ICU patients: Schematic representation of the real-time data acquisition system combining Near-Infrared Spectroscopy (NIRS) and Arterial Blood Pressure (ABP) monitoring. NIRS signals, sampled at 10 Hz, were transmitted via Bluetooth to OxySoft software, then streamed to ICM+ using the Lab Streaming Layer (LSL). Simultaneously, ABP was measured invasively and digitized at 100 Hz using a DT9804 data acquisition module. Both data streams were synchronized and recorded in ICM+ at a unified sampling rate of 100 Hz.

3.2.2 Microvascular Monitoring Instrumentation Setup for Healthy Participants

Microvascular perfusion monitoring of healthy participants was conducted in a similar configuration as ICU patients where PortaMon was used for the brachioradialis of skeletal muscle and PortaLite was used for the frontal cortex of the brain. Sensor readings of NIRS sensor devices were transmitted through Bluetooth in real-time into OxySoft and streamed into ICM+ via the LSL. Streamed NIRS data were recorded in ICM+ with a sampling rate of 10 Hz. Microvascular monitoring of healthy participants was conducted for a minimum of 60 minutes while they were in a horizontal resting posture, lying on a bed. Participants were instructed to avoid crossing their legs and to minimize movement during the monitoring period.

Monitoring of continuous blood pressure physiological signals from healthy participants was conducted using a non-invasive dual finger cuff system from the Human NIBP Nano monitoring

system (ADInstruments, USA). The monitored Non-Invasive Blood Pressure (NIBP) signals were transmitted to the PowerLab data acquisition system (ADInstruments, USA) and these NIBP signals were acquired continuously and recorded in real-time using the LabChart software (ADInstruments, USA) at a sampling rate of 200 Hz. The instrumentation setup of microvascular and NIBP monitoring of healthy participants is shown in Figure 3.3.

Since NIRS and NIBP signals were recorded separately, event markers were simultaneously added to each using their respective recording software, ICM+ for NIRS and LabChart for NIBP. Once the recordings were completed, these event markers were used to integrate the NIRS time series with the NIBP time series at a sampling rate of 10 Hz.

Prior to microvascular monitoring, the skinfold thickness of the brachioradialis was measured using a skinfold caliper to assess adipose tissue thickness.

Figure 3.3: Microvascular Monitoring Instrumentation Setup for healthy participants

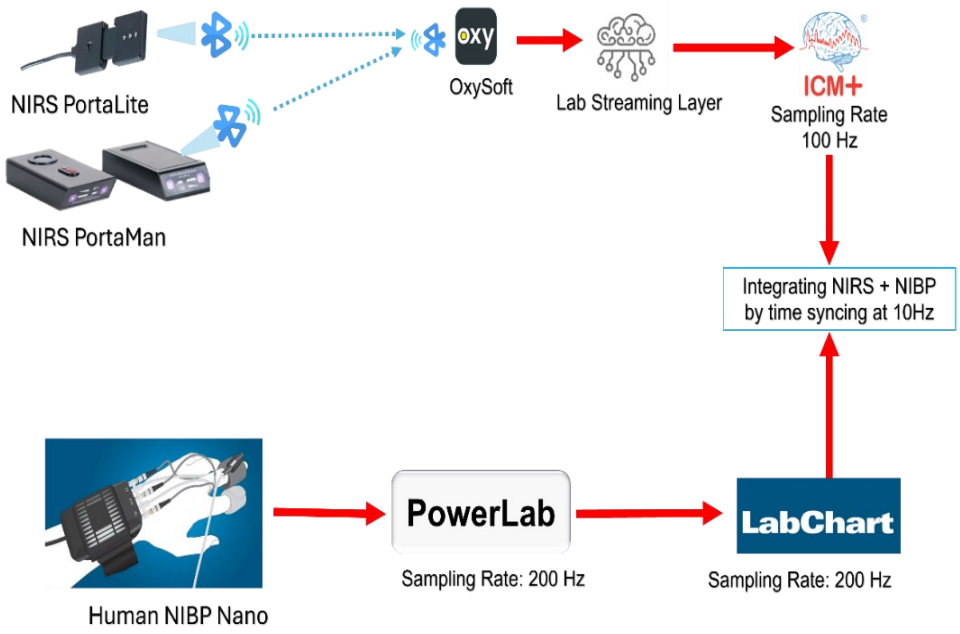

Microvascular Monitoring Instrumentation Setup for healthy participants: Instrumentation setup illustrating the simultaneous monitoring of cerebral and skeletal muscle perfusion using NIRS sensors (PortaLite on the frontal cortex, PortaMon on the brachioradialis), and continuous non-invasive blood pressure (NIBP) monitoring using a dual finger cuff system. NIRS signals were streamed via Bluetooth to OxySoft and recorded in ICM+ at 10 Hz, while NIBP signals were captured by PowerLab and recorded in LabChart at 200 Hz. Event markers synchronized both streams post-recording for integrated time-series analysis.

3.3 Data Preprocessing

All the recorded data of ICU patients and healthy participants were preprocessed to remove artifacts and down-sampled with anti-aliasing filtering by following the preprocessing pipeline described in Figure 3.4**.** Physiological data mainly contained artifacts due to various sources such as movement, environmental interference, or biological noise. For this study, NIRS data were mainly affected by the motion of the patient and those motion artifacts are easily detected by visually inspecting. Approaches include signal filtering, artifact rejection algorithms, independent component analysis (ICA), adaptive filtering methods, time series data mining and Machine learning/Deep Learning tested but manual removal of artifacts with visual inspection were highly effective than other autonomous approaches.

Figure 3.4: Raw Time Series Preprocessing Pipeline

Raw Time Series Preprocessing Pipeline: Preprocessing pipeline for NIRS, ABP, and NIBP signals, including manual artifact removal via visual inspection using ICM+ software, followed by anti-aliasing filtering (0–4.5 Hz) and down sampling to 10 Hz

Manual artifact removal was highly effective but time-consuming due to the need for visual inspection of the entire recording. To enhance efficiency, an unsupervised time series data mining method was employed to assist in manual artifact removal[198]. The method uses z-normalized Euclidean distances between all subsequences in the time series data (NIRS and ABP/NIBP) and their nearest neighbors to detect anomalies, including motion artifacts, microvascular autoregulation anomalies, and environmental interference. This method has a success rate of 99% in detecting motion artifacts and environmental interferences, yet due to the unsupervised nature of this method, it cannot separate microvascular autoregulation anomalies from the rest of the artifacts. Thus, timestamps of all identified anomalies were used as reference points to localize motion artifacts and environmental interferences and manually remove them by visual inspection. Manual removal of artifacts was done using the artifact remover tool of ICM+ software. Once artifact were removed, data were exported as comma-separated values (.csv) from ICM+ for the analysis. Down sampling and anti-aliasing filtering were done by python based pre-processing script.

3.3.1 Data Processing and Data Analysis

To evaluate the physiological coherence between skeletal muscle and brain, this study analyzed time-frequency and time-phasic coherence between microvascular perfusions of skeletal muscle and brain, as well as microvascular perfusions of skeletal muscle and brain with ABP/NIBP. Thus, this study investigated the following physiological signal pairs.

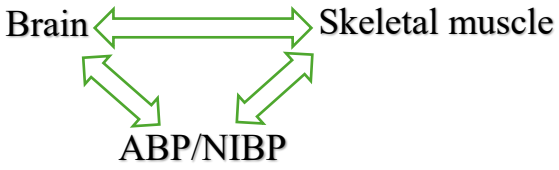

1. HbT- Brain vs HbT Skeletal muscle
2. HbT- Brain vs ABP/NIBP
3. HbT- Skeletal muscle vs ABP/NIBP

Wavelet-based methods have been utilized to evaluate physiological coherence as wavelet analysis provides enhanced time-frequency localization for signals[25,27,191,194]. Thus, wavelet coherence was used to evaluate time-frequency coherence and wavelet-based semblance was used to evaluate time-phasic coherence of muscle and brain by analyzing microvascular perfusion with HbT time series and ABP/NIBP time series.

3.3.2 Wavelet Analysis

Wavelet analysis is preferred for analyzing NIRS data due to several advantages. Firstly, wavelet transform methods offer superior time-frequency resolution for non-stationary biological signals compared to traditional Fourier methods, allowing for a more detailed analysis of NIRS signals [199]. Additionally, wavelet analysis excels in noise removal and background correction, crucial for enhancing the quality of NIRS data [200]. Moreover, wavelet-based techniques are effective in removing global physiological noise from NIRS signals, improving the accuracy of the analysis [201]. Overall, the adaptability and efficiency of wavelet analysis make it a powerful tool for processing and interpreting NIRS data in various applications, offering enhanced insights and improved signal quality compared to other methods.

Wavelet coherence analysis is utilized for evaluating the physiological coherence of the brain, muscles, and systemic blood pressure due to its ability to provide time-localized information about data in both time and frequency domains. This method allows for the measurement of the time-varying correlation between two simultaneous signals, incorporating the effect of frequency and amplitude as quantified values ranging from 0 to 1, where 0 represents no coherence and 1 represents full coherence. Wavelet coherence analysis is particularly effective in assessing neural coupling and synchrony between brain regions, offering insights into functional relationships and

coherence within specific wavelength ranges [202,203]. By capturing coherent oscillatory behavior in NIRS signals, wavelet coherence analysis enhances the understanding of microvascular dynamics and physiological interactions. For this study, wavelet coherence computation was implemented as explained by Torrence and Compo [204] with Morlet mother wavelet.

Wavelet semblance analysis is preferred for NIRS analysis to assess the time-phasic relationship in physiological coherence of the brain and muscles due to its ability to handle nonstationary and dynamic signals effectively. This technique, utilizing wavelet coherence and semblance, provides high time-frequency resolution, making it suitable for analyzing complex physiological states like cerebral autoregulation after brain injury[27,205,206]. Therefore, calculating wavelet semblance as a measure of instantaneous phase difference allows for a detailed examination of the spectral features involved in the microcirculatory relationship between brain, muscle, and systemic blood pressure.

Computation of physiological coherence of brain and muscle with wavelet analysis followed 3 main steps:

1. Finding overlapping time series segments of selected physiological signal pairs,
2. Generating Wavelet coherence / Wavelet-based semblance
3. Calculating the percentage of time above the statistically significant coherence/semblance threshold for selected physiological signal pairs.

3.3.3 Segment stitching

Due to the variability of motion artifacts and other artifacts occurrence between head and body, artifact cleaned NIRS HbT time series of brain and muscle have discontinued segments. To evaluate time–frequency and time-phasic coherence, HbT time series segments should be aligned in the time domain. Thus, from discontinued segments of brain and muscle HbT time series, overlapping segments are extracted by computing matching overlapping. These computed segments are indexed based on their position in the time series to facilitate the organization and subsequent analysis of the extracted segments. To minimize the edge effects of wavelet transformation, overlapped segments with a time duration of 30 min > were selected for coherence analysis. Example of this process is shown in Figure 3.5.

Figure 3.5: Visualization of NIRS time series plots

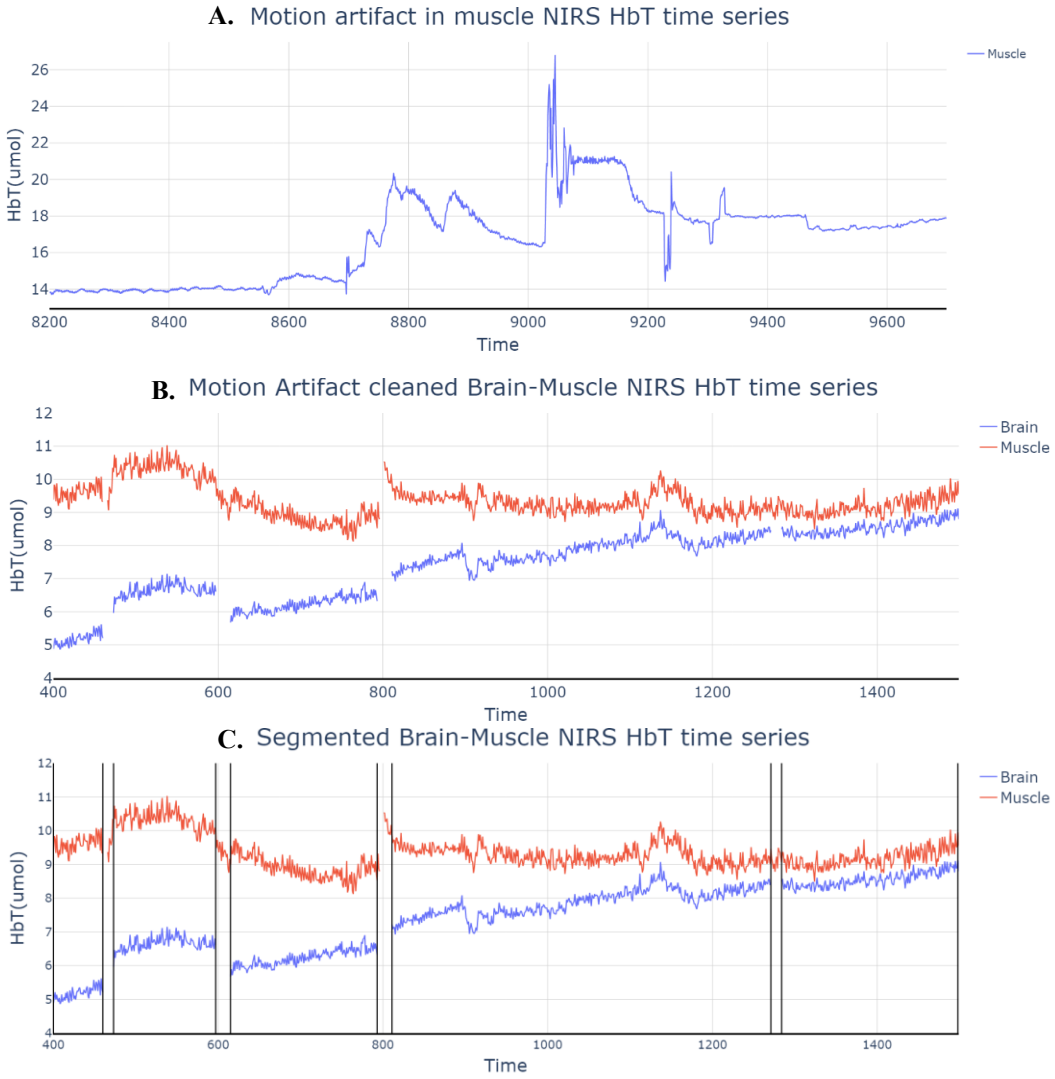

Visualization of NIRS time series plots : (A) Muscle NIRS HbT time series showing motion artifacts. (B) Motion artifact-cleaned and time-aligned HbT signals from brain and muscle, illustrating discontinuities due to artifact removal. (C) Segmented overlapping HbT time series used for coherence analysis, with vertical lines indicating the selected overlapped segments

In the next step, wavelet coherence and wavelet semblance of overlapped brain and muscle HbT NIRS time series segments of a specific recording were computed. From these wavelet coherence and wavelet semblance matrixes of each segment, coherence/semblance in frequency ranges 0.005 Hz - 3.1 Hz were extracted. Figure 3.6 presents a time-frequency heatmap of wavelet coherence for a selected segment of overlapped brain and muscle HbT NIRS time series.

Figure 3.6: Wavelet Coherence Heatmap

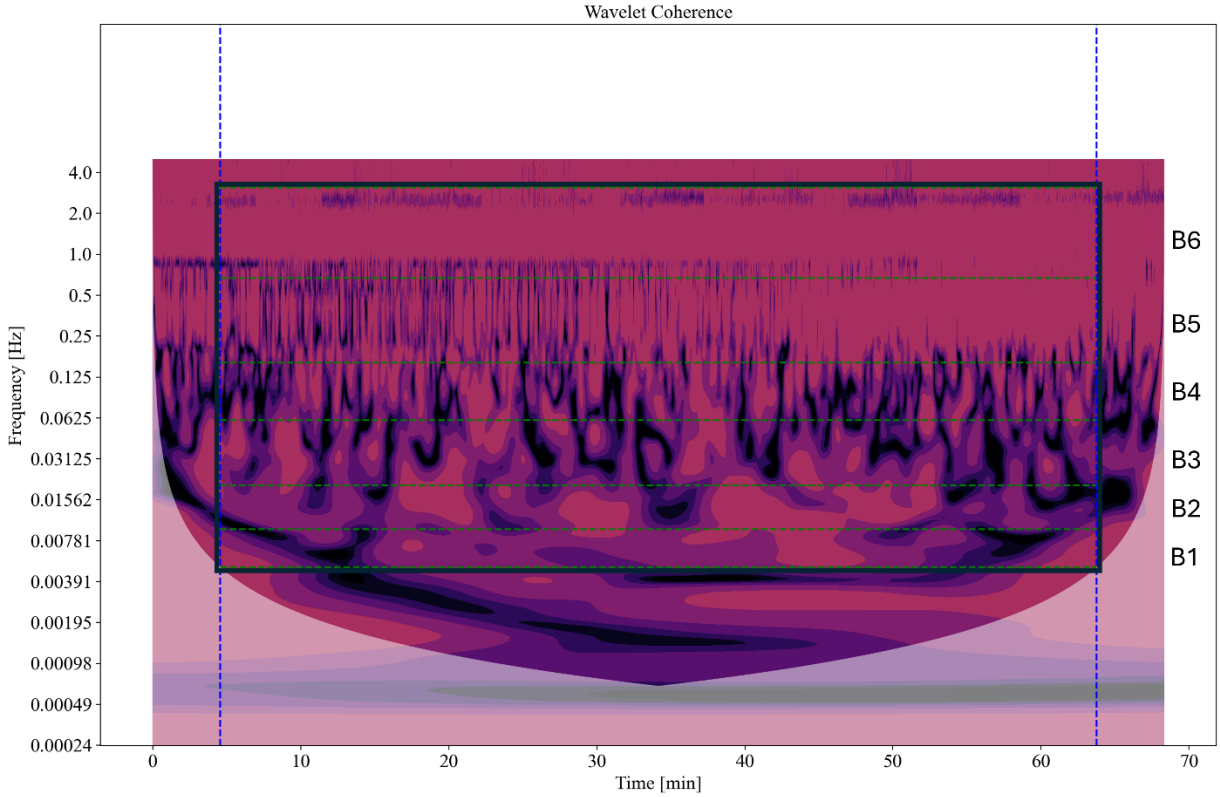

Wavelet Coherence Heatmap: Wavelet coherence analysis between overlapped brain and skeletal muscle HbT time series, highlighting key sub-frequency bands. Dashed green lines delineate physiological frequency ranges: Endothelial (B2), Neurogenic (B3), Myogenic (B4), Respiratory (B5), and Cardiac (B6). The central region outlined in black excludes edge effects, ensuring accurate coherence interpretation within the specified frequency bands.

According to the findings of studies[207,208], the above-selected frequent ranges are significant for analyzing cardiovascular dynamics in the NIRS time series. Then, edge effects were removed from those matrixes as explained in Grinsted et al[189], and wavelet coherence and wavelet semblance matrixes of each segment were combined according to the segment time index. Finally, unique wavelet coherence and wavelet semblance data were generated to analyze time–frequency and time-phasic coherence of a specific recording. This process was utilized to generate wavelet coherence and wavelet semblance of all recordings of the ICU patients/healthy participants for above stated three physiological signal pairs (Brain- Muscle, Brain-ABP/NIBP, Muscle-ABP/NIBP).

Wavelet coherence analysis matrices data were divided into six distinct frequency bands to differentiate between peripheral and central hemodynamic regulatory mechanisms. These six

frequency bands, derived from pharmacological iontophoresis studies of human skin, are proposed to represent specific physiological processes in blood flow regulation[129,207–211]. As shown in Table 3.1, the lower frequency bands, Endothelial (B2), Neurogenic (B3), and Myogenic (B4) reflect microvascular hemodynamic mechanisms. In contrast, the higher frequency bands correspond to central regulatory processes, with the Respiratory band (B5) capturing breathing-related oscillations and the Cardiac band (B6) representing heart rate-associated fluctuations within the microcirculation[129,207,209].

Table 3.1: Frequency bands used in wavelet coherence analysis

Frequency band	Frequency ranges (Hz)
B0	0 – 0.005
B1—Metabolic	0.005 – 0.0095
B2—Endothelial	0.0095 – 0.02
B3—Neurogenic	0.02 – 0.06
B4—Myogenic	0.06 – 0.16
B5—Respiratory	0.16 – 0.667
B6—Cardiac	0.667 – 3.1

Frequency bands used in wavelet coherence analysis to distinguish between peripheral and central hemodynamic regulatory mechanisms: Lower frequency bands: Endothelial (B2), Neurogenic (B3), and Myogenic (B4) represent peripheral (microvascular) regulatory mechanisms. Higher frequency bands reflect central regulation, with the Respiratory band (B5) capturing breathing-related oscillations and the Cardiac band (B6) corresponding to heart rate-related fluctuations within the microcirculation. These frequency bands are derived from pharmacological iontophoresis studies of human skin and are associated with specific physiological processes involved in blood flow regulation.

From these six frequency bands, only the Endothelial (B2), Neurogenic (B3), Myogenic (B4), Respiratory (B5), and Cardiac (B6) frequency bands were analyzed to evaluate physiological coherence in microvascular hemodynamics. To comprehensively assess microvascular dynamics, the three lower-frequency bands, Endothelial (B2), Neurogenic (B3), and Myogenic (B4), were analyzed both as individual components and collectively as the "Microvascular frequency band (MV)" (frequency range: 0.0095 Hz to 0.16 Hz).

From these extracted wavelet coherence matrices of each frequency band, average wavelet coherence over time was computed for each data point in the time domain. The above explained

physiological time series segmentation process and frequency bands were utilized to compute significant wavelet semblance based on significant wavelet coherence.

3.4 Derivation of Statistically significant coherence thresholds

To distinguish genuine physiological coherence from background noise, statistically significant coherence threshold between skeletal muscle and brain was determined using Monte Carlo simulations with 30 min red noise pairs. The red noise pairs were generated using the same AR(1) coefficients as the input physiological time series (ABP, muscle NIRS, and brain NIRS). Analysis of the AR(1) coefficient distributions revealed non-normal distributions for Brain HbT, Muscle HbT, and ABP/NIBP signals, with significant differences between ABP/NIBP and both NIRS HbT series. Figure 3.7 illustrates these distributions of AR(1) coefficients of physiological time series.

Figure 3.7: Distribution of AR (1) Coefficients for Brain HbT, Muscle HbT, and ABP/NIBP Signals

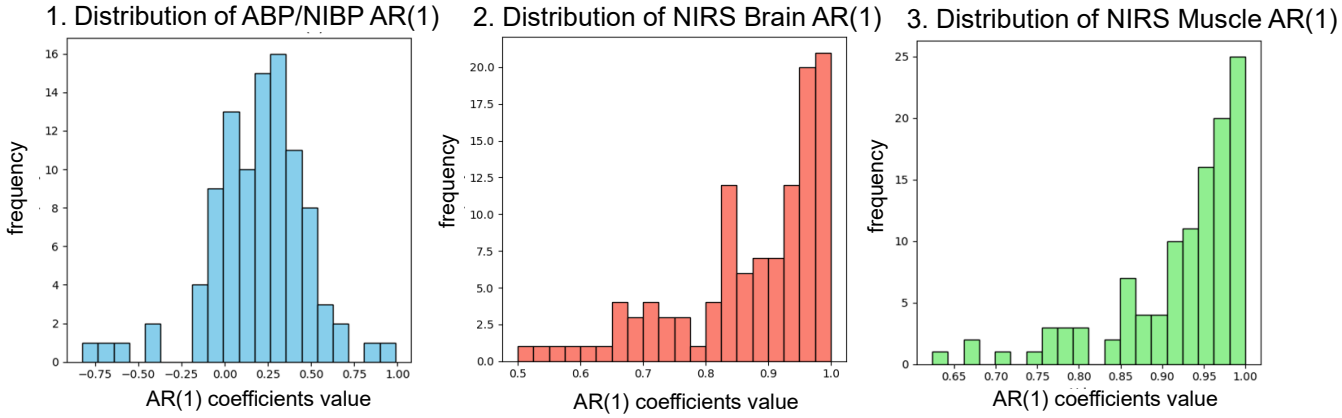

These histograms depict the distributions of first-order autoregressive AR(1) coefficients for Arterial Blood Pressure (ABP)/Non-Invasive Blood Pressure (NIBP), brain near-infrared spectroscopy (NIRS) hemoglobin total (HbT), and muscle NIRS HbT physiological time series. These coefficients were estimated to match the temporal autocorrelation properties of the original signals and were used to generate red noise surrogates in Monte Carlo simulations for coherence thresholding.

For each physiological signal pair, 1000 red noise pairs were generated in the frequency range of 0.005 - 4.5 Hz. These pairs were used to calculate coherence thresholds using Monte Carlo simulation. Statistical thresholds for wavelet coherence were based on the average of values greater than 95% of simulated coherence values for each pair. Only coherence values outside the cone of influence were considered for this simulation. This methodology ensures that the simulated red noise accurately represents the temporal characteristics of the original physiological time

series, allowing for a more reliable distinction between genuine physiological coherence and noise-induced correlations.

The significant coherence thresholds exhibit variability across the frequency range of 0.0095 Hz to 4.5 Hz, with notable fluctuations observed in the microvascular frequency band, as illustrated in Figure 3.8. To facilitate band-specific analysis, frequency-based thresholds were employed to determine significant wavelet coherence for each of the physiological frequency bands: Endothelial (B2), Neurogenic (B3), Myogenic (B4), Respiratory (B5), and Cardiac (B6). This approach allows for a thorough examination of wavelet coherence within each specific frequency range, assessing for the distinct characteristics of each frequency band. These frequency-based thresholds are presented in Table 3.2

Figure 3.8: Variability of Significant Coherence Thresholds across the Frequency Range

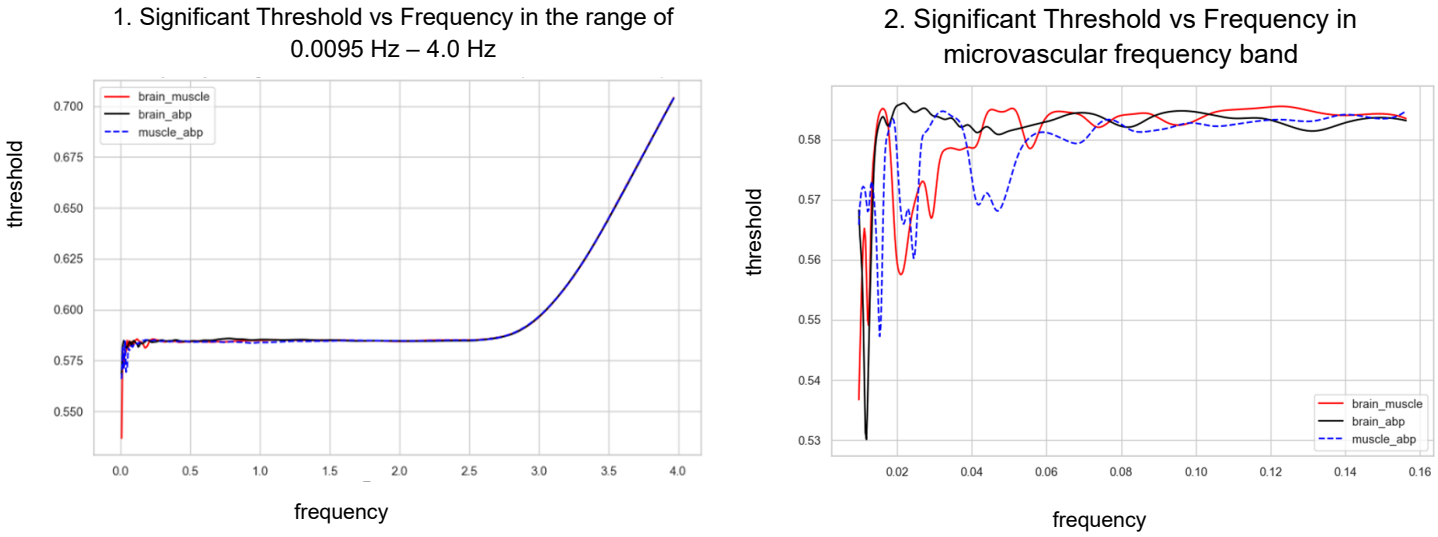

Variability of significant coherence thresholds across the frequency range: The figure illustrates the distribution of significant coherence thresholds across the overall frequency range of 0.0095 Hz to 4.5 Hz and within the Microvascular frequency range of 0.0095 Hz – 0.16 Hz.

Table 3.2: Significant Coherence Thresholds of Frequency Bands

Frequency band	Physiological pair		
	Brain-Muscle	Brain-ABP/NIBP	Muscle-ABP/NIBP
Endothelial (B2),	0.576	0.579	0.577
Neurogenic (B3),	0.575	0.583	0.575
Myogenic (B4),	0.584	0.583	0.582
Microvascular (B2-B4)	0.576	0.579	0.576
Respiratory (B5)	0.584	0.584	0.584
Cardiac (B6)	0.585	0.585	0.584

Significant coherence thresholds of frequency bands: Significant coherence thresholds are presented for each physiological frequency band, including Endothelial (B2), Neurogenic (B3), Myogenic (B4), Respiratory (B5), and Cardiac (B6). These thresholds facilitate band-specific identification of significant wavelet coherence within the analyzed frequency ranges.

3.4.1 Significant Wavelet Coherence Quantification

Based on the derived significance thresholds for coherence, the percentage of time above the threshold of B2 – B6 and the Microvascular frequency bands were computed for each recording of all patients/healthy participants. These "*percentage of time above the significant coherence durations of wavelet coherence — %signfCoherenceDuration"* is defined as:

$$\%\text{sigfCoherenceDuration} = \left(\frac{\text{time above significant coherence}}{\text{total time of computed coherence}} \times 100\right) \quad \text{----- (15)}$$

3.4.2 Significant Wavelet Semblance Quantification

Significant wavelet semblance was determined based on significant wavelet coherence to ensure the reliability of phase relationships between two physiological time series. Individual wavelet semblance values with significant wavelet coherence values were extracted, while wavelet semblance values with non-significant wavelet coherence were excluded. Frequency-based wavelet coherence thresholds presented in Table II were used to determine significant wavelet semblance in specific frequency bands. This method is adapted from the wavelet semblance-based pressure reactivity index (wPRx) calculation, as described by Liu et al[195], but focuses on frequency band-specific time-phasic relationships of HbT time series of the brain, skeletal muscle, and systemic blood pressure.

As illustrated in Figure 3.9, binary masking was employed to extract significant wavelet semblance values. Then, for each frequency band, the grand average of these significant wavelet semblance values was calculated across all segments of physiological time series pairs within a specific recording. *"Significant Wavelet Semblance"* values were utilized to quantify the degree of phase locking (i.e. time-dependent correlation) between skeletal muscle and brain in each frequency band.

Figure 3.9: Time-Frequency Plots on Deriving Significant Wavelet Semblance based on Significant Wavelet Coherence

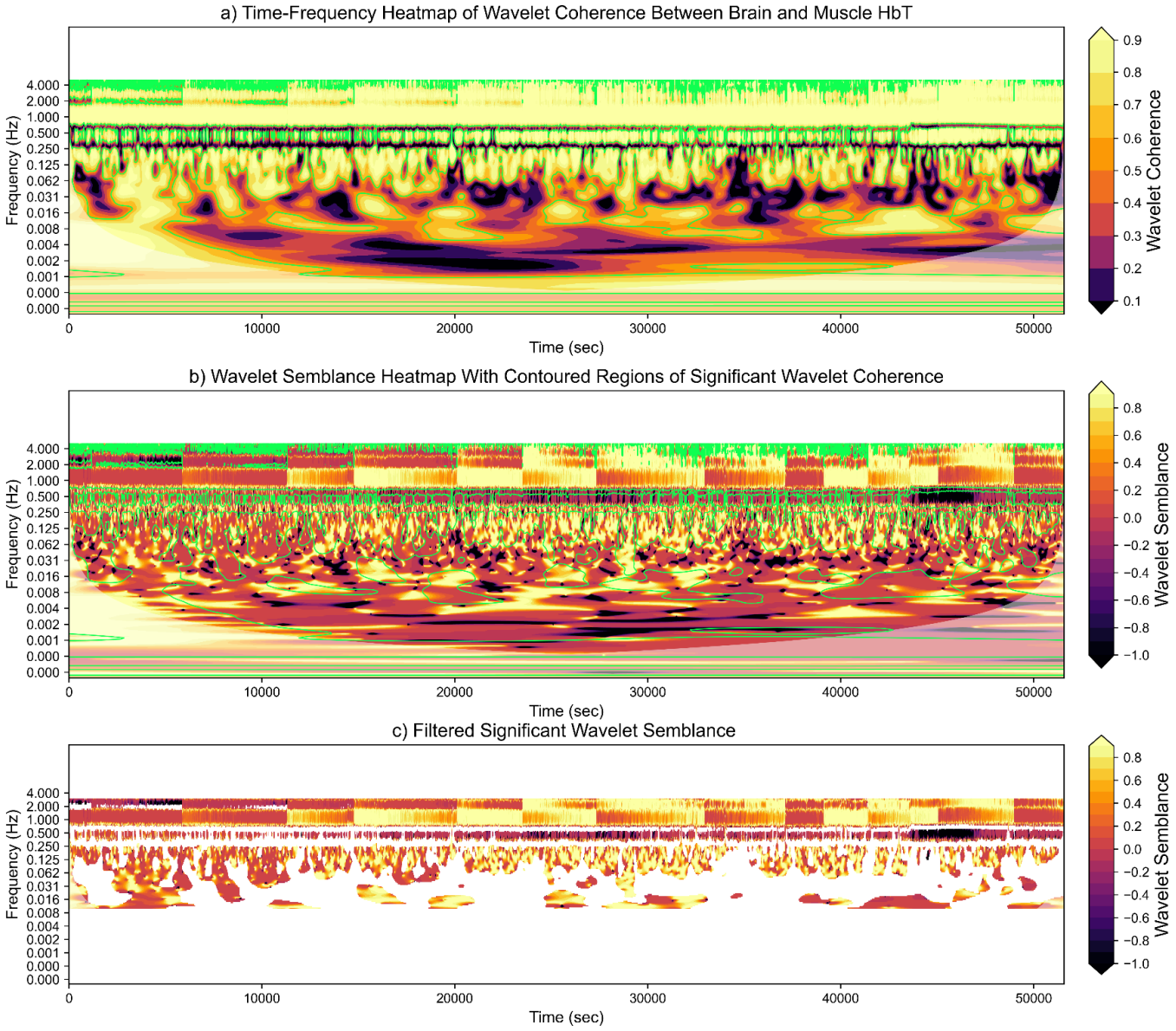

Time-frequency plots on deriving significant wavelet semblance based on significant wavelet coherence: (a) The top plot presents the time-frequency heatmap of wavelet coherence between brain and muscle total hemoglobin (HbT) time series. Regions where the wavelet coherence exceeds the significance threshold-indicating significant coupling between the signals are marked with contours. (b) The middle plot shows the corresponding wavelet semblance heatmap, with contours outlining regions where wavelet coherence exceeds the significance threshold. These contours highlight the time-frequency zones where phase relationships between the signals are considered statistically reliable, based on the frequency-specific thresholds outlined in Table II. (c) The bottom plot displays the significant wavelet semblance, generated by applying a binary mask to retain only semblance values within regions of significant coherence. This filtered heatmap quantifies the degree of time-dependent phase locking between the brain and muscle HbT time series, restricted to periods and frequency bands where statistically significant coupling is present.

3.5 Categorization of ICU Patient Population Cohorts

In this study, ICU patient population cohorts were defined based on clinical outcomes and the specific days on which physiological monitoring data were collected during the ICU stay. Patient data were extracted from the first day (Day 1) of ICU admission to establish a baseline cohort. This Day 1 cohort was subsequently stratified into two subgroups according to ICU outcomes: survivors (patients discharged alive from the ICU) and non-survivors (patients who died during their ICU stay). In addition to Day 1 data, further cohorts were constructed based on patient data collected on the third day (Day 3) of ICU admission. The structure of the cohorts thus enabled a comparative analysis of patient progression over time, as well as an assessment of the relationship between early clinical indicators and ultimate patient outcomes.

3.6 Statistical Analysis

Statistical analyses were conducted to assess the physiological coherence of microvascular hemodynamics between the brain and skeletal muscle, as well as their associations with systemic blood pressure, thereby directly addressing the research hypotheses : **Hypothesis 1.1**: *The physiological coherence of microvascular hemodynamics between the brain and skeletal muscle, and with systemic blood pressure, is significantly altered in ICU patients compared to healthy controls,* and ***Hypothesis 1.2****: The ICU non-survivors exhibit significantly altered physiological coherence of microvascular hemodynamics between the brain and skeletal muscle, and with systemic blood pressure, compared to ICU survivors.*

Statistical analyses were performed using two primary metrics derived from wavelet coherence analysis: (1) *the percentage of time above the significant wavelet coherence duration - %signfCoherenceDuration* and (2) *Significant Semblance*, where all these values are calculated for each frequency band and physiological signal pair across all recordings.

To assess Hypothesis 1.1, this study compared the *%signfCoherenceDuration* and *Significant Semblance* values between healthy controls and ICU patients on Day 1 of monitoring. Analyses focused on both Microvascular (B2–B4) and Cardiac (B6) frequency bands for three physiological signal pairs: (i) Brain–Skeletal muscle, (ii) Brain–ABP/NIBP, and (iii) Skeletal Muscle–ABP/NIBP. Thereby, directly addressing the hypothesized alteration of physiological coherence

of microvascular hemodynamics in ICU patients compared with healthy individuals. Additionally, subgroup comparisons between ICU survivors and non-survivors versus healthy controls were conducted to contextualize the observed alterations relative to the baseline physiological states of healthy controls.

In line with Hypothesis 1.2, As a secondary analysis, this study evaluated differences in *%signfCoherenceDuration* and *Significant Semblance* values between ICU survivors and ICU non-survivors, again focusing on both Microvascular and Cardiac frequency bands of all three physiological signal pairs.

Additionally, this study evaluated the changes in coherence measures (%signfCoherenceDuration and Significant Semblance) between Day 1 and Day 3 within the ICU patient cohort. This longitudinal evaluation aimed to explore potential temporal dynamics in microvascular coherence during critical illness.

For this study, data was assessed for normality and determined to be non-parametric. Therefore, comparisons of all analyses utilized using the Mann–Whitney U test. No correction for multiple testing was taken, although secondary and longitudinal analyses should be interpreted as exploratory.

4 CHAPTER 4 - RESULTS

4.1 Population Demographics and Microvascular Monitoring Characteristics

4.1.1 ICU population

This study analyzed 40 ICU patients, with demographic details summarized in Table 4.1. Among these patients, physiological data from 31, 26, and 26 patients on Day 1 of ICU stay, and 11, 5, and 7 patients on Day 3, were included for analyzing the physiological signal pairs: Brain–Skeletal Muscle, Brain–ABP, and Skeletal Muscle–ABP, respectively. The overlapping distribution of patients across these physiological signal pairs on Day 1, which was used to evaluate physiological coherence in microcirculation hemodynamics visualized in the Venn diagram in Figure 4.1. During the study period, 383 patients were screened, and 54 patients were enrolled. Patient screening, recruitment, and filtering for the physiological coherence in microcirculation hemodynamics are illustrated in Figure 4.2.

Figure 4.1: Overlap of Patients Population

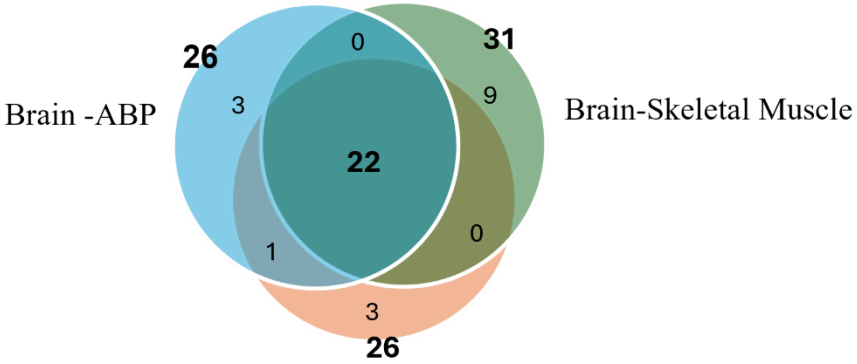

Overlap of Patients Across Brain–Skeletal Muscle, Brain–ABP, and Skeletal Muscle–ABP Physiological Signal Pair Analyses on Day 1 of ICU Stay

This ICU patient population comprised 23 males (57.50%) and 17 females (42.50%). The age distribution of this cohort ranged from 20 to 87 years, with a mean age of 60.53 ± 16.68 years. 22 of 40 patients (55.0%) had a diagnosis of sepsis. 32 of 40 patients (80.00%) had some forms of pre-existing cardiovascular comorbidity, including hypertension, diabetes, vascular disease, or heart failure. The median *(IQR) norepinephrine* dose was 0.12 µg/kg/min (0.04–0.17 µg/kg/min) during the recording period; 36 of 40 patients (90.00%) were also on vasopressin. The median (IQR) serum lactate levels were 3.00 mmol/L (1.40–3.25mmol/L) and capillary refill time was

normal (< 3 s) for 36 of 40 patients (90.00%). Adipose tissue thickness overlying the brachioradialis muscle was 3.43 ± 1.26 mm (n = 38 patients, two patients with missing data). Sensors were placed on the forearm and forehead ipsilaterally in 28 patients and contralaterally in 12 patients (n=40).

Figure 4.2: One Arm CONSORT Diagram of MIMICSS

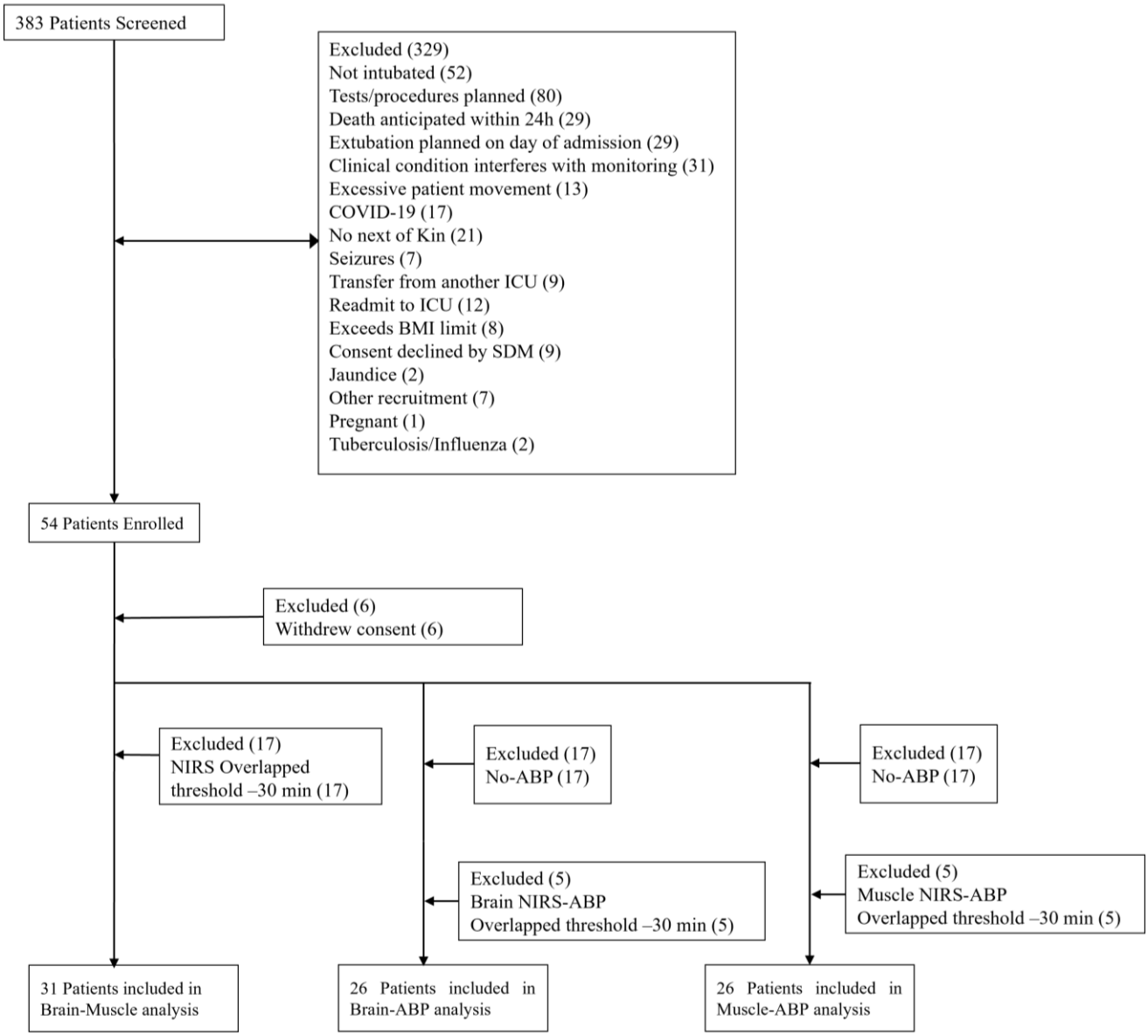

One Arm CONSORT diagram: MIMICSS Observational Study on Physiological Coherence in Microvascular Hemodynamics between Brain and Skeletal Muscle of Day 1 ICU Stay.

The average duration of patient recordings was 386.41 ± 152.36 minutes. Following the initial preprocessing of the artifact removal, the physiological time series had an average duration of 59.17 ± 28.32 minutes.

Table 4.1: Demographics for the ICU Patients

Patients Demographic	*n = 40*
Age (yr)	60.53 ± 16.68
Female	17/40
Sepsis	22/40
Norepinephrine dose (μg/kg/min)	0.12 (0.04 - 0.17)
Vasopressin	36/40
Lactate (mmol/L)	3.00 (1.40 –3.25)
Acute Physiology and Chronic Health Evaluation II score	16.83 (14.50 – 19.50)
Capillary refill time < 3 s	36/40
Heart rate	91.84 ± 20.59

Demographics for the ICU patients in the final dataset included for analysis. Data are present as mean ± SD, median (IQR), or proportion of the total cohort (n = 40).

4.1.2 Healthy Population

In this study, a total of 15 healthy participants were recruited from the community, consisting of 9 (60%) males and 6 (40%) females. The age distribution ranged from 21 to 75 years, with a mean age of 41.20 ± 19.96 years. Participants had an average height of 168.82 ± 7.06 cm, an average weight of 69.52 ± 11.34 kg, and an average Body Mass Index (BMI) of 24.44 ± 4.13 kg m^{-2}. Their average resting heart rate was recorded at 72.60 ± 11.84 beats per minute. Capillary refill time was normal for all participants. The adipose tissue thickness of the brachioradialis muscle, measured using a skinfold caliper had an average of 3.75 ± 1.51 mm.

Microvascular monitoring of all healthy participants (n = 15) was conducted using NIRS sensors placed on the forearm and forehead ipsilaterally. Simultaneous collection of Non-Invasive Blood Pressure (NIBP) data was achieved in 12 out of 15 participants. The average recording time for healthy participants in the resting phase was 66.56 ± 9.19 minutes (IQR: 60.47 min - 72.14 min). After initial preprocessing to remove artifacts, 73% of the signal duration from all recordings of healthy participants was determined to be suitable for analysis. The summary statistics of total

duration of signals used for significant coherence analysis, following overlapping signal segment processing and the removal of the cone of influence from wavelet analysis, are presented in Table 4.2.

Table 4.2: Summary Statistics of Processed Signal Pair Durations for Significant Coherence Analysis

Signal pairs	*mean*	*std*	*min*	*Q1*	*Q3*	*max*
Brain-Muscle (min)	57.96	13.24	40.71	50.28	63.02	82.75
Brain-NIBP (min)	49.97	10.39	31.33	44.40	52.20	67.76
Muscle-NIBP (min)	49.97	10.39	31.33	44.40	52.20	67.76

4.2 Evaluation of Physiological Coherence in Microvascular Hemodynamics between Brain and Skeletal Muscle using Wavelet Coherence and Wavelet Semblance Analysis

Evaluation of physiological coherence in microvascular hemodynamics between the brain and skeletal muscle, along with their coupling to systemic blood pressure was assessed by quantifying the time-frequency and time-phasic relationships of microvascular perfusion in the brain and skeletal muscle and with ABP/NIBP. Quantified statistically significant microvascular hemodynamics coherence measures: *%signfCoherenceDuration* and *Significant Semblance* were computed as explained in methodology with frequency band-specific wavelet coherence thresholds. These metrics were evaluated across three physiological signal pairs: (i) Brain–Skeletal Muscle, (ii) Brain–ABP/NIBP, and (iii) Skeletal Muscle–ABP/NIBP.

The Results chapter is structured to address the study's two primary hypotheses directly. First, Section 4.3 evaluates *Hypothesis 1.1*, comparing the physiological coherence of microvascular hemodynamics between ICU patients and healthy controls to determine whether critical illness alters brain-skeletal muscle and systemic microvascular hemodynamics coherence patterns. Next, Section 4.5 addresses *Hypothesis 1.2*, focusing on differences between ICU survivors and non-survivors to assess whether these microvascular coherence measures are associated with clinical outcomes. Each subsection presents wavelet coherence and semblance findings across the Cardiac (B6) and Microvascular bands (B2–B4) frequency bands accompanied by statistical summaries, graphs, and interpretive insights. Together, these analyses aim to characterize the alterations of

physiological coherence of microvascular hemodynamics in critical illness and its potential clinical implications.

4.3 Comparative Analysis of Physiological Coherence of Microvascular Hemodynamics between ICU Population Cohorts and Healthy Control Population

This section evaluates Hypothesis 1.1 by comparing microvascular hemodynamic coherence metrics: *%signfCoherenceDuration* and *Significant Semblance* between ICU cohorts and healthy control populations across the Microvascular (B2–B4) and Cardiac (B6) frequency bands. The analysis focuses on three physiological signal pairs: (i) Brain–Skeletal Muscle, (ii) Brain–ABP/NIBP, and (iii) Skeletal Muscle–ABP/NIBP. Results are organized by these signal pairs and stratified by frequency bands, presenting a comparative analysis of coherence metrics between ICU patients on Day 1 of the study and healthy controls.

4.3.1 Wavelet Coherence Analysis: ICU Patients vs. Healthy Controls

In the wavelet coherence analysis of ICU patients on day 1 of ICU stay compared to healthy controls, the ICU population exhibited a significantly lower *%signfCoherenceDuration* values for the Brain–Skeletal Muscle pair in the cardiac frequency band compared to healthy controls (83.01%, IQR 56.89% – 97.34% vs. 97.14%, IQR 93.19% – 98.61%; $p = 0.0415$). No statistically significant differences were observed in the *%signfCoherenceDuration* for the Brain–Skeletal Muscle pair in the Microvascular frequency band. For the Skeletal Muscle–ABP/NIBP pair, ICU patient population on day 1 ICU stay demonstrated a significantly higher *%signfCoherenceDuration* in the Microvascular frequency band compared to healthy controls (5.14%, IQR 2.05%–10.02% vs. 0.40%, IQR 0.00%–1.97%; $p = 0.0055$). No significant differences were observed in the cardiac frequency band for the Skeletal Muscle–ABP/NIBP pair. Additionally, no significant differences were observed in either the cardiac or microvascular frequency bands for the Brain–ABP/NIBP pair. These comparisons are visualized using interleaved scatter plots in Figure 4.3. Summary statistics and corresponding significance tests for the Cardiac and Microvascular frequency bands are presented in Table 4.3.

Figure 4.3: Distribution of Significant Wavelet Coherence between ICU Patients vs Healthy Controls.

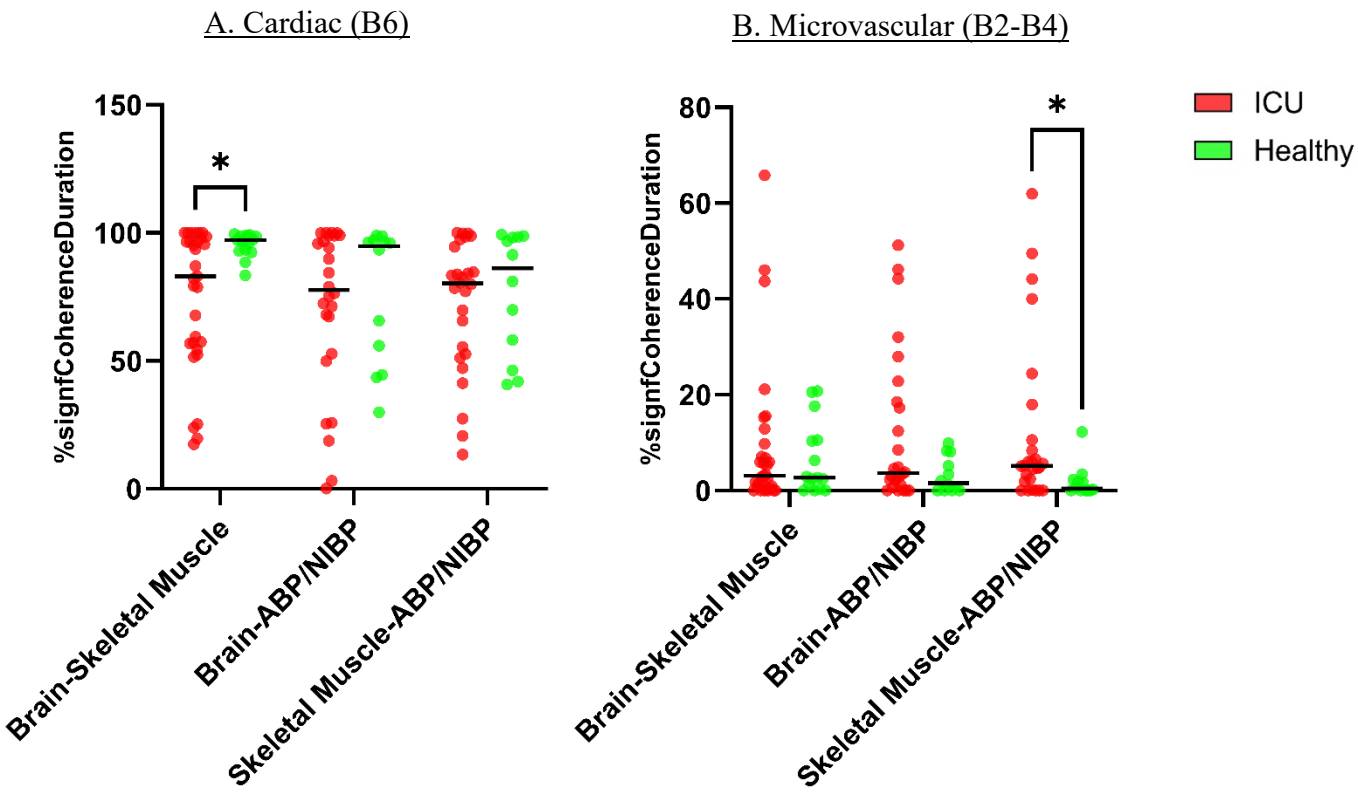

Distribution of Significant Wavelet Coherence (*%signfCoherenceDuration*) in ICU patients of Day 1 vs. Healthy controls across (A) Cardiac frequency band (B6) and (B) Microvascular frequency bands (B2–B4) for Brain–Skeletal Muscle(ICU: n = 31, Healthy: n = 15), Brain–ABP/NIBP(ICU: n = 26, Healthy: n = 12), and Skeletal Muscle–ABP/NIBP(ICU: n = 26, Healthy: n = 12) signal pairs. Interleaved scatter plots display individual data points, with median values indicated. Asterisks (*) indicate statistically significant group differences ($p < 0.05$, Mann–Whitney U test).

Table 4.3: Comparative Analysis of Wavelet Coherence of ICU Patients vs. and Healthy Controls

Frequency bands	Brain – Muscle	
	Healthy (15)	ICU (31)
Microvascular (B2–B4)	2.72% (0.79% - 10.46%)	3.07% (0.71% - 8.44%)
Cardiac (B6) **	97.14% (93.19% - 98.61%)	83.01% (56.89% - 97.34%)
	Brain - ABP	
	Healthy (12)	ICU (26)
Microvascular (B2–B4)	1.58% (0% - 5.91%)	3.66% (1.40% - 18.19%)
Cardiac (B6)	94.78% (53.11% - 96.75%)	77.71% (56.39% - 98.35%)
	Muscle - ABP	
	Healthy (12)	ICU (26)
Microvascular (B2–B4) **	0.40% (0% - 1.97%)	5.14% (2.05% - 10.02%)
Cardiac (B6)	86.21% (55.19% - 98.21%)	80.27% (53.41% - 92.05%)

Comparative analysis of Wavelet Coherence (*%signfCoherenceDuration*) between ICU patients (Day 1) and healthy controls across three physiological signal pairs: Brain–Skeletal Muscle, Brain–ABP/NIBP, and Skeletal Muscle–ABP/NIBP within the Cardiac (B6) and Microvascular (B2–B4) frequency bands. Data are presented as median (IQR). Statistical comparisons were conducted using the Mann–Whitney U non-parametric test. Asterisks (**) indicate statistically significant differences at $p < 0.05$.

4.3.2 Wavelet Semblance Analysis: ICU Patients vs. Healthy Controls

The semblance analysis observed significant differences between ICU patient cohorts of day 1 ICU stay and healthy controls in the cardiac frequency band for all three physiological signal pairs: Brain–Skeletal Muscle, Brain–ABP/NIBP and Skeletal Muscle–ABP/NIBP. ICU patients exhibited significantly lower semblance for the Brain–Skeletal Muscle pair compared to healthy controls (0.37, IQR 0.21–0.54 vs. 0.71, IQR 0.59 – 0.75; $p = 0.0000$). Similarly, the Brain–ABP/NIBP pair showed significantly lower negative semblance in ICU patients compared to controls (-0.36, IQR -0.44 – -0.26 vs. -0.03, IQR -0.08 – 0.00; $p = 0.0006$). The Skeletal Muscle–ABP/NIBP pair also demonstrated significantly lower negative semblance among ICU patients relative to healthy controls (-0.34, IQR -0.45 – -0.21 vs. -0.04, IQR -0.23 – 0.021; $p = 0.0073$). No significant differences in semblance were observed between the groups for any physiological signal pairs in the Microvascular frequency band. Figure 4.4 illustrates these comparisons, and full summary statistics and significance testing results are presented in Table 4.4.

Figure 4.4: Distribution of Wavelet Semblance between ICU Patients vs. Healthy Controls

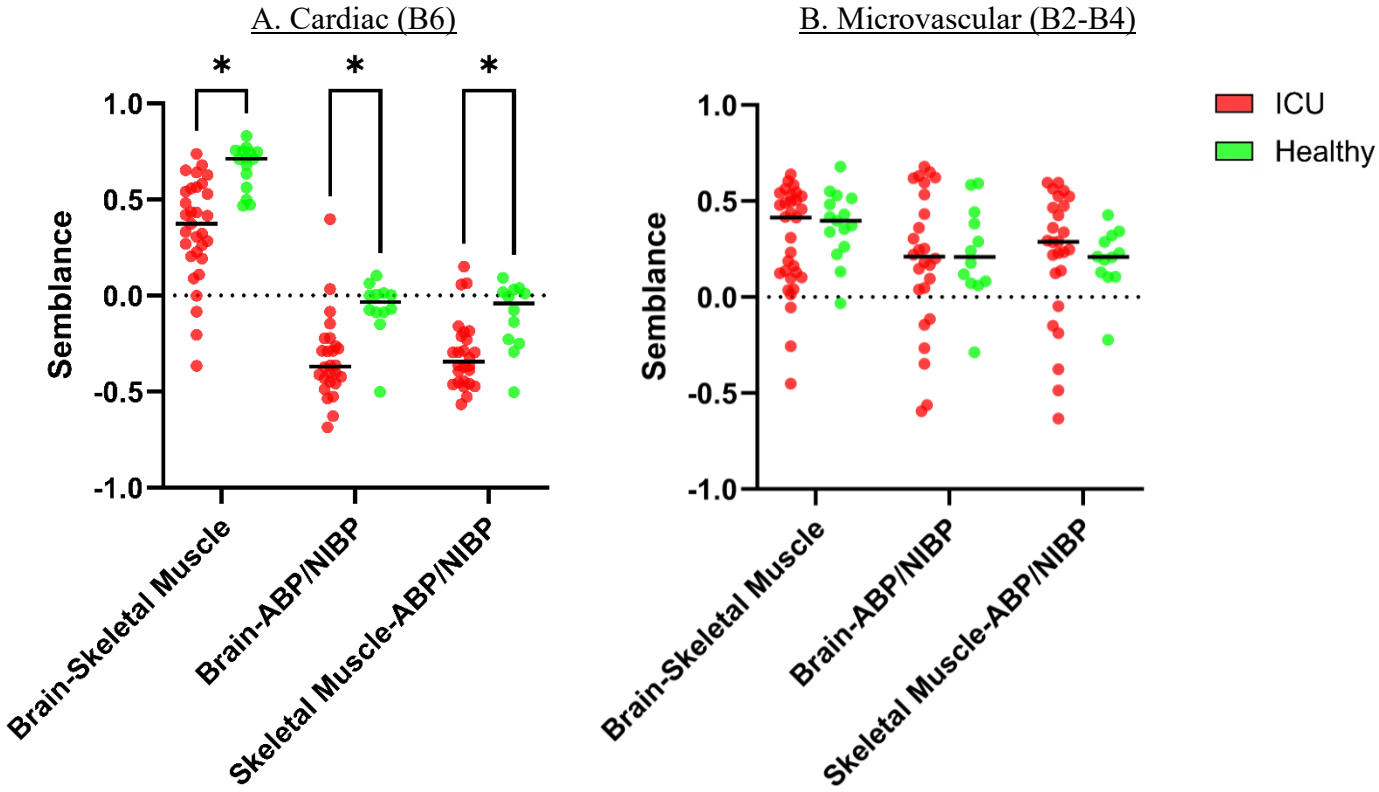

Distribution of wavelet semblance in ICU patients (Day 1) vs. Healthy controls across (A) Cardiac frequency band (B6) and (B) Microvascular frequency bands (B2–B4) for Brain–Skeletal Muscle(ICU: $n = 31$, Healthy: $n = 15$), Brain–ABP/NIBP(ICU: $n = 26$, Healthy: $n = 12$), and Skeletal Muscle–ABP/NIBP(ICU: $n = 26$, Healthy: $n = 12$) signal pairs. Interleaved scatter plots display individual data points, with median values indicated. Asterisks (*) indicate statistically significant group differences ($p < 0.05$, Mann–Whitney U test).

Table 4.4: Comparative Analysis of Wavelet Semblance of ICU Patients vs. Healthy Control

Frequency bands	Brain – Muscle	
	Healthy (15)	ICU (31)
Microvascular (B2–B4)	0.39 (0.30 – 0.49)	0.41 (0.11 – 0.51)
Cardiac (B6) **	0.71 (0.59 – 0.75)	0.37 (0.21 – 0.54)
	Brain - ABP	
	Healthy (12)	ICU (26)
Microvascular (B2–B4)	0.20 (0.08 – 0.39)	0.21 (0.04 – 0.50)
Cardiac (B6) **	-0.034 (-0.08 – 0.00)	-0.36 (-0.44 – -0.26)
	Muscle - ABP	
	Healthy (12)	ICU (26)
Microvascular (B2–B4)	0.20 (0.12 – 0.29)	0.28 (0.12 – 0.47)
Cardiac (B6) **	0.04 (-0.23 – 0.021)	-0.34 (-0.45 – -0.21)

Comparative analysis of wavelet semblance between ICU patients (Day 1) and healthy controls across three physiological signal pairs: Brain–Skeletal Muscle, Brain–ABP/NIBP, and Skeletal Muscle–ABP/NIBP within the Cardiac (B6) and Microvascular (B2–B4) frequency bands. Data are presented as median (IQR). Statistical comparisons were conducted using the Mann–Whitney U non-parametric test. Asterisks (**) indicate statistically significant differences at $p < 0.05$.

Exploratory subgroup analyses comparing ICU survivors and non-survivors against healthy controls were conducted to provide additional context for interpreting the observed time-frequency and time-phase alterations relative to baseline physiological states of healthy controls. Given the exploratory nature of this study and its primary focus on overall ICU population dynamics, these supplementary comparisons are presented as supporting data in Appendix Tables A.1-A.4.

4.4 Analysis of Statistical Significance between Microvascular Frequency Sub-Bands.

The microvascular frequency band consists of three physiologically distinct sub-frequency bands: Endothelial (B2), Neurogenic (B3), and Myogenic (B4). Evaluating statistical differences among these sub-bands is critical for Hypothesis 1.2, as it allows for a more granular understanding of how specific regulatory mechanisms of microvascular hemodynamics, such as endothelial function, autonomic regulation, and vascular smooth muscle activity, may be differentially impaired in critically ill patients and associated with mortality. Among these, the Endothelial (B2) frequency band showed a significantly lower *%signfCoherenceDuration* measure compared to the Myogenic (B4) frequency band (0%, IQR 0%–2.50% vs. 11.40%, IQR 5.50%–26.44%; $p = 0.0000$) and the Neurogenic (B3) frequency band (0%, IQR 0%–2.50% vs. 4.04%, IQR 2.74%–

9.97%; p = 0.004) in the Muscle-NIBP signals of the healthy population. No significant differences were observed in other physiological signal pairs within the healthy population. Additionally, no significant differences were found in the wavelet coherence of all three physiological signal pairs in the ICU population. No significant differences in significant semblance were observed among the microvascular sub-frequency bands across both populations. These findings imply that in critical illness, the disruption of microvascular coherence may affect all microvascular control mechanisms uniformly, which could obscure outcome related distinctions unless sub-band specific analysis is performed.

4.5 Comparative Analysis of Physiological Coherence of Microvascular Hemodynamics: ICU Non-Survivors vs. ICU Survivors

This section evaluates Hypothesis 1.2 by comparing microvascular hemodynamic coherence metrics: *%signfCoherenceDuration* and *Significant Semblance* between ICU non-survivors and ICU survivors across the Microvascular (B2–B4), Cardiac (B6), and selected Sub-Microvascular frequency bands, to assess whether microvascular coherence is selectively altered in non-survivors during the early phase of critical illness (Day 1 of ICU stay). The analysis focuses on three physiological signal pairs: (i) Brain–Skeletal Muscle, (ii) Brain–ABP, and (iii) Skeletal Muscle–ABP. This comparative analysis builds upon the observations from Hypothesis 1.1, where ICU population showed distinct microvascular coherence patterns relative to healthy controls, suggesting that physiological coherence may be differentially disrupted depending on the ICU patient outcome trajectory. Results are therefore organized by signal pair and frequency band, presenting a targeted comparative analysis of coherence metrics according to ICU patient outcomes (survived or deceased) to more precisely characterize the microvascular hemodynamic alterations associated with mortality.

4.5.1 Wavelet Coherence Analysis: ICU Survivors vs. Non-Survivors

Analysis of wavelet coherence measure: *%signfCoherenceDuration* identified a significant difference between ICU survivors and non-survivors within the Endothelial (B2) frequency band of the Brain-Skeletal Muscle physiological signal pair, with survivors demonstrating significantly lower coherence values compared to non-survivors (8.65%, IQR 2.86%–15.10% vs. 15.15%, IQR 11.93%–24.25%; p = 0.03). No statistically significant differences were observed in other frequency bands or physiological signal pairs between survivors and non-survivors. Comparative

summary statistics of coherence values in the three physiological signal pairs for the Endothelial frequency band, Microvascular frequency band, and cardiac frequency band are presented in Table 4.5, and these comparisons are illustrated in Figure 4.5.

Figure 4.5: Distribution of Wavelet Coherence between ICU Survivors vs. Non-Survivors.

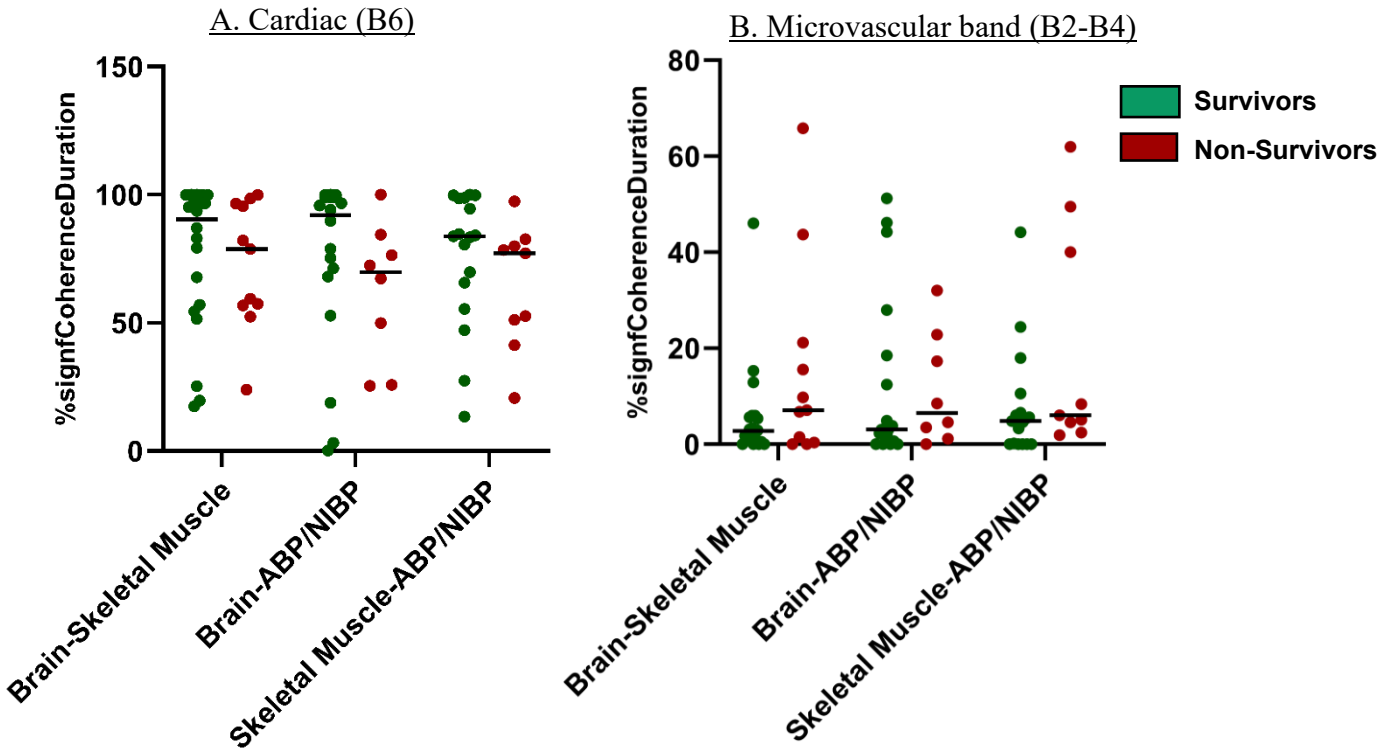

Distribution of wavelet coherence in ICU survivors vs. ICU non-survivors across (A) Cardiac frequency band (B6) and (B) Microvascular frequency bands (B2–B4) for Brain–Skeletal Muscle(Survivors: n = 20, Non-Survivors: n = 11), Brain–ABP(Survivors: n = 18, Non-Survivors: n = 8), and Skeletal Muscle–ABP(Survivors: n = 17, Non-Survivors: n = 9) signal pairs. Interleaved scatter plots display individual data points, with median values indicated. Asterisks (*) indicate statistically significant group differences ($p < 0.05$, Mann–Whitney U test).

Table 4.5: Comparative Analysis of Wavelet Coherence between ICU Survivors vs. Non-Survivors

Frequency bands	Brain – Muscle	
	Survivors (20)	Non-Survivors (11)
Endothelial (B2) **	8.63% (2.87% - 15.11%)	15.15% (11.94% - 24.26%)
Microvascular (B2–B4)	2.79% (0.83% - 5.72%)	7.13% (0.92% - 18.36%)
Cardiac	90.38% (56.37% - 98.43%)	78.76% (57.07%-96.05%)
	Brain - ABP	
	Survivors (18)	Non-Survivors (8)
Endothelial (B2)	10.31% (2.89% - 23.04%)	14.18% (11.15% - 19.80%)
Microvascular (B2–B4)	3.09% (1.00% - 16.97%)	6.51% (2.94% - 18.68%)
Cardiac	92.00% (68.85% - 98.96%)	69.83% (43.91%- 78.46%)
	Muscle - ABP	
	Survivors (17)	Non-Survivors (9)
Endothelial (B2)	8.08% (0.83% - 18.74%)	19.94% (12.47% - 25.47%)
Microvascular (B2–B4)	4.81% (0.04% - 6.59%)	6.05% (4.58% - 40.05%)
Cardiac	83.78% (65.73% - 98.54%)	77.20% (51.23% - 79.99%)

Comparative analysis of wavelet coherence between ICU survivors and non-survivors across the Endothelial (B2), Microvascular (B2–B4), and Cardiac (B6) frequency bands based on Day 1 ICU monitoring data. Data are presented as median (IQR). Statistical comparisons were conducted using the Mann–Whitney U non-parametric test. Asterisks (**) indicate statistically significant differences at $p < 0.05$.

4.5.2 Wavelet Semblance Analysis: ICU Survivors vs. Non-Survivors

Significant semblance analysis of the Skeletal Muscle–ABP signal pair revealed significant differences between ICU survivors and non-survivors across multiple frequency bands. ICU Non-survivors demonstrated significantly higher semblance compared to survivors in the Endothelial (B2) (0.27, IQR 0.22–0.48 vs. 0.01, IQR −0.13–0.12; $p = 0.0388$), Neurogenic (B3) (0.55, IQR 0.33–0.59 vs. 0.26, IQR −0.22–0.33; $p = 0.0153$), and Microvascular (B2–B4) (0.52, IQR 0.24–0.56 vs. 0.23, IQR −0.14–0.33; $p = 0.0205$) frequency bands. Conversely, in the Cardiac (B6) frequency band, non-survivors exhibited significantly lower negative semblance compared to survivors (−0.44, IQR −0.47 to −0.38 vs. −0.28, IQR −0.36 to −0.18; $p = 0.0043$). No statistically significant differences in semblance values were observed for any frequency bands in the Brain–Skeletal Muscle and Brain–ABP physiological signal pairs.

Tables 4.6–4.8 summarize the significant semblance values across the Microvascular frequency bands, their sub-frequency bands, and the Cardiac frequency band for the three physiological signal pairs. Figure 4.6 illustrates the distribution of semblance values of the Microvascular and

cardiac frequency bands across the Brain–Skeletal Muscle, Brain–ABP, and Skeletal Muscle–ABP signal pairs.

Figure 4.6: Distribution of Wavelet Semblance between ICU Survivors vs. Non-Survivors.

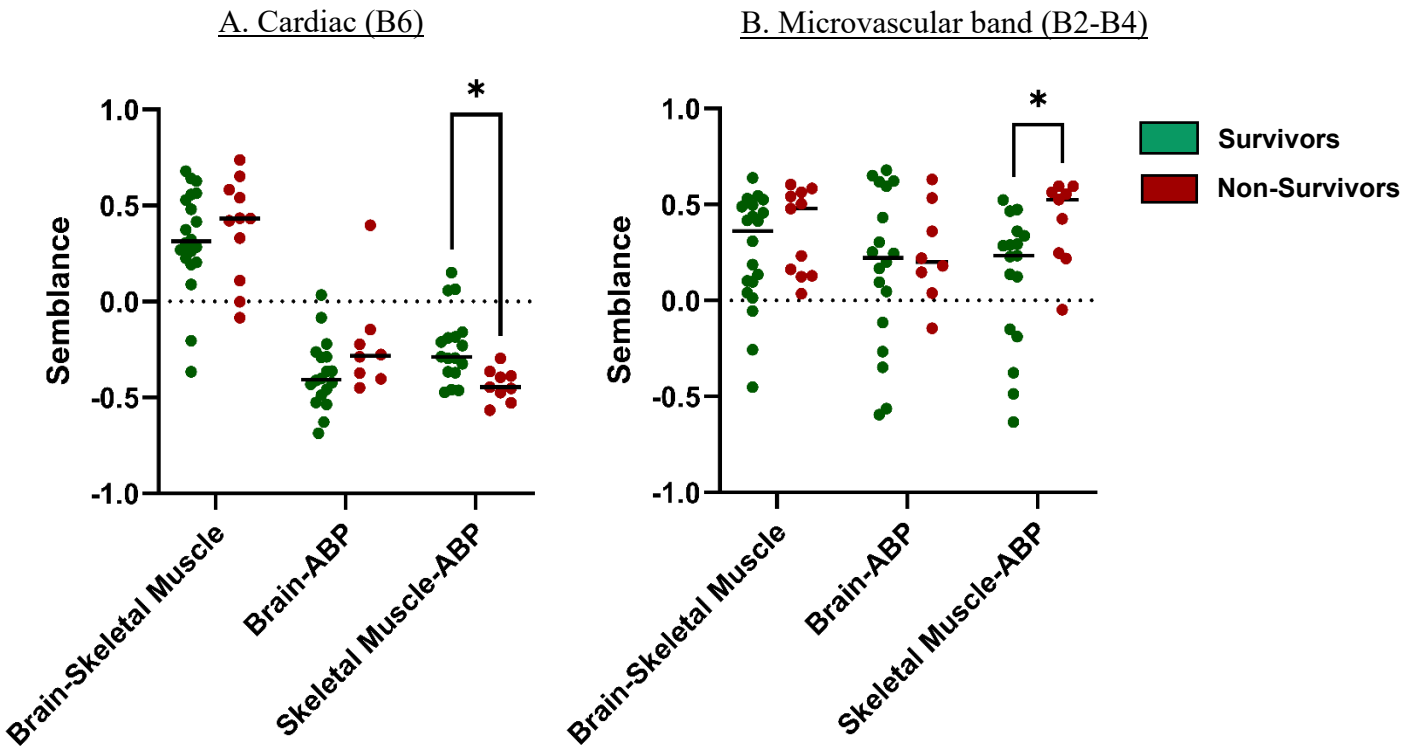

Distribution of wavelet semblance in ICU survivors vs. ICU non-survivors across (A) Cardiac frequency band (B6) and (B) Microvascular frequency bands (B2–B4) for Brain–Skeletal Muscle(Survivors: n = 20, Non-Survivors: n = 11), Brain–ABP(Survivors: n = 18, Non-Survivors: n = 8), and Skeletal Muscle–ABP(Survivors: n = 17, Non-Survivors: n = 9) signal pairs. Interleaved scatter plots display individual data points, with median values indicated. Asterisks (*) indicate statistically significant group differences ($p < 0.05$, Mann–Whitney U test).

Table 4.6: ICU Outcome Analysis of Wavelet Semblance in Brain–Skeletal Muscle

Frequency bands	Brain – Skeletal Muscle	
	Survivors (B2: n = 19, 20)	Non-Survivors (11)
Endothelial (B2)	0.1919 (-0.0297 - 0.4918)	0.3878 (0.1581 - 0.5685)
Neurogenic (B3)	0.3797 (0.0347 - 0.483)	0.3804 (0.208 - 0.543)
Myogenic (B4)	0.3657 (0.2584 - 0.4651)	0.1432 (-0.0486 - 0.5791)
Microvascular(B2-B4)	0.362 (0.0835 - 0.4905)	0.48 (0.146 - 0.5535)
Cardiac (B6)	0.3143 (0.2209 - 0.5359)	0.433 (0.2197 - 0.5611)

Summary statistics and significant testing data of significant semblance of Brain-Muscle in the Endothelial (B2), Neurogenic (B3), Myogenic (B4), Microvascular(B2-B4) and Cardiac (B6) frequency bands between ICU survivors vs. non-survivors based on Day 1 ICU monitoring data. Data are presented as median (IQR). Statistical comparisons were conducted using the Mann–Whitney U non-parametric test. Asterisks (**) indicate statistically significant differences at $p < 0.05$.

Table 4.7: ICU Outcome Analysis of Wavelet Semblance in Brain–ABP

Frequency bands	Brain – ABP	
	Survivors (B2: n = 16, 18)	Non-Survivors (8)
Endothelial (B2)	0.0647 (-0.5111 – 0.4709)	0.247 (-0.1608 – 0.4776)
Neurogenic (B3)	0.2051 (-0.0843 – 0.5241)	0.4207 (0.2893 – 0.4607)
Myogenic (B4) **	0.3442 (0.1319 – 0.5143)	0.1607 (-0.2929 – 0.3394)
Microvascular(B2-B4)	0.2228(-0.0741 – 0.5546)	0.201 (0.1199 – 0.4041)
Cardiac (B6)	-0.4059 (-0.4797 – -0.2888)	-0.2817 (-0.3804 – -0.204)

Summary statistics and significant testing data of significant semblance of Brain-ABP in the Endothelial (B2), Neurogenic (B3), Myogenic (B4), Microvascular(B2-B4) and Cardiac (B6) frequency bands between ICU survivors vs. non-survivors based on Day 1 ICU monitoring data. Data are presented as median (IQR). Statistical comparisons were conducted using the Mann–Whitney U non-parametric test. Asterisks (**) indicate statistically significant differences at $p < 0.05$.

Table 4.8: ICU Outcome Analysis of Wavelet Semblance in Skeletal Muscle–ABP

Frequency bands	Skeletal Muscle - ABP	
	Survivors (B2: n = 16, 17)	Non-Survivors (9)
Endothelial (B2) **	0.0136 (-0.1312 – 0.1225)	0.2769 (0.2232 – 0.4851)
Neurogenic (B3) **	0.262 (-0.2225 – 0.3351)	0.5592 (0.3304 – 0.5943)
Myogenic (B4)	0.3305 (0.0519 – 0.4646)	0.3847 (0.1073 – 0.4982)
Microvascular(B2-B4) **	0.2336 (-0.1495 – 0.3378)	0.5256 (0.2469 – 0.5635)
Cardiac (B6) **	-0.2878 (-0.3664 – -0.1834)	-0.4462 (-0.475 – -0.3882)

Summary statistics and significant testing data of significant semblance of Skeletal Muscle-ABP in the Endothelial (B2), Neurogenic (B3), Myogenic (B4), Microvascular(B2-B4) and Cardiac (B6) frequency bands between ICU survivors vs. non-survivors based on Day 1 ICU monitoring data. Data are presented as median (IQR). Statistical comparisons were conducted using the Mann–Whitney U non-parametric test. Asterisks (**) indicate statistically significant differences at $p < 0.05$.

4.6 Comparison of Physiological Coherence in Microvascular Hemodynamics between Day 1 and Day 3 of ICU patients

Analysis of physiological coherence in microvascular hemodynamics of the ICU population, comparing Day 1 and Day 3 ICU monitoring data, showed no statistically significant differences in wavelet semblance and wavelet coherence measures across the Cardiac and Microvascular frequency bands. This analysis was conducted on patients with artifact-free microvascular monitoring data available for both Day 1 and Day 3. Sample sizes for the physiological signal pairs were: Brain–Skeletal Muscle (n = 9), Brain–ABP (n = 6), and Skeletal Muscle–ABP (n = 6). The corresponding interleaved scatter plots illustrating Day 1 versus Day 3 values for each physiological signal pair and frequency band are presented in Figure 4.10.

Figure 4.7: ICU Patient Analysis: Day 1 vs. Day 3

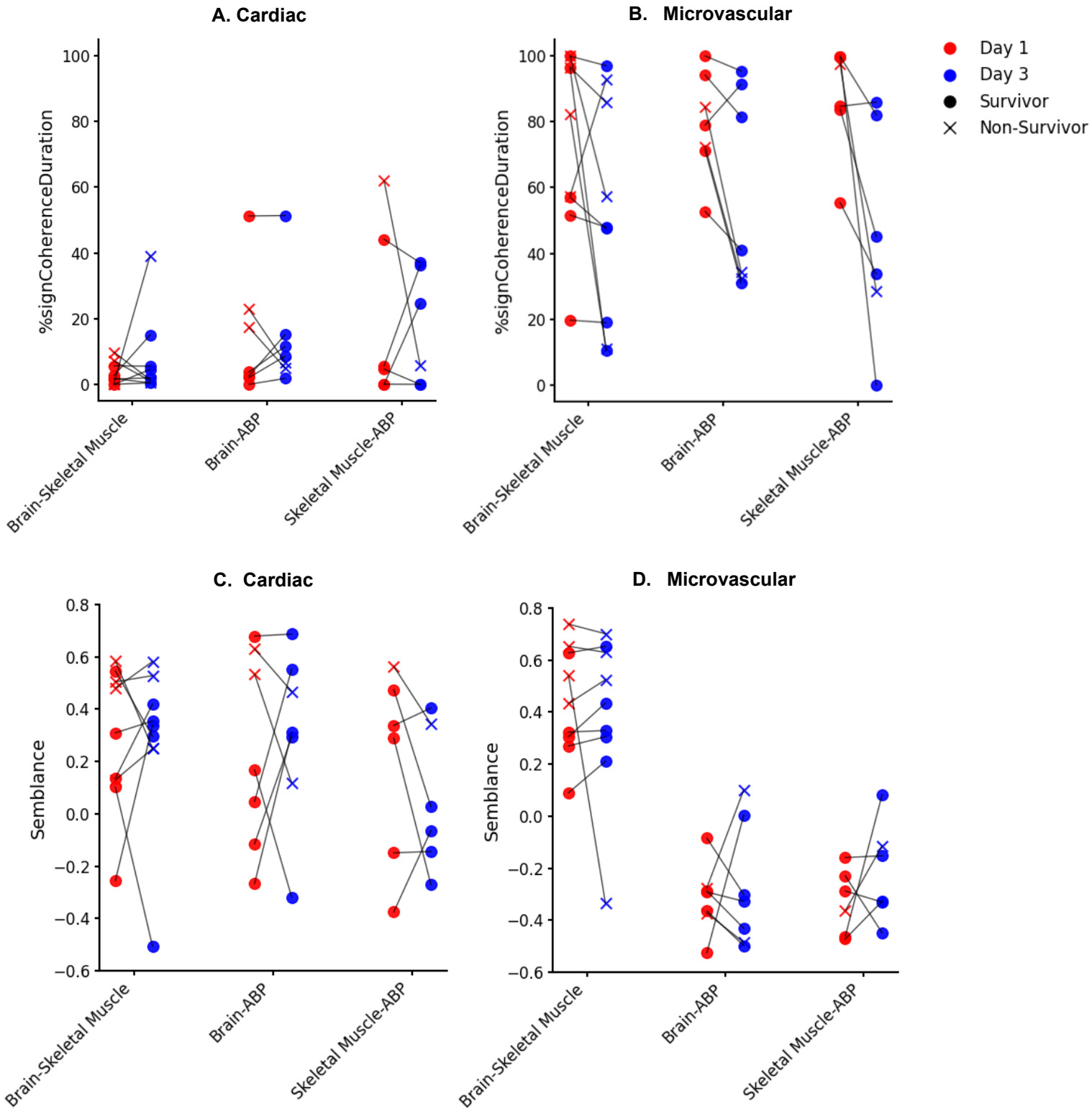

Interleaved scatter plots comparing wavelet coherence and wavelet semblance values on Day 1 and Day 3 of ICU monitoring across the Cardiac and Microvascular frequency bands. Data are shown for patients with artifact-free recordings in the following physiological signal pairs: Brain–Skeletal Muscle (n = 9), Brain–ABP (n = 6), and Skeletal Muscle–ABP (n = 6).

5 CHAPTER 5 - DISCUSSION

This study represents the first comprehensive investigation to systematically evaluate the physiological coherence of microvascular hemodynamics between brain and skeletal muscle using high-resolution near-infrared spectroscopy and their coupling with systemic blood pressure, utilizing wavelet-based signal processing techniques. By employing wavelet coherence and semblance analyses across multiple frequency bands that reflect distinct physiological regulatory processes, this research establishes a novel methodological framework for quantifying dynamic brain-skeletal muscle microvascular coherence and their coupling to systemic blood pressure in both critically ill ICU patients and healthy controls. This study addresses two primary research hypotheses: whether microvascular hemodynamic coherence is altered in critically ill patients compared to healthy controls (Hypothesis 1.1), and whether these coherence patterns differ between ICU survivors and non-survivors (Hypothesis 1.2).

The findings from this study make several important theoretical contributions to understanding microvascular physiology. First, it establishes that the physiological coherence of microvascular hemodynamics between brain and skeletal muscle is significantly altered during critical illness, challenging the assumption of uniform microvascular dysregulation across organs. Second, this study demonstrates that excessive phase-locked synchronization between skeletal muscle microcirculation and systemic blood pressure observed in ICU non-survivors compared to ICU survivors is associated with poor clinical outcomes, suggesting a potential pathophysiological mechanism of multi-organ dysfunction.

5.1 Summary of Findings

5.1.1 Hypothesis 1.1: Physiological coherence of microvascular hemodynamics alterations in ICU patients compared to healthy controls

The results of the analyses provide strong evidence supporting Hypothesis 1.1, demonstrating significant alterations in physiological coherence of microvascular hemodynamics between brain and skeletal muscle in ICU patients compared to healthy controls. ICU patients exhibited significantly reduced duration of significant wavelet coherence *(%signfCoherenceDuration*) and diminished phase synchrony (*Significant Semblance*) between brain and skeletal muscle microcirculation in the cardiac frequency band (B6: 0.667-3.1 Hz) compared to healthy controls

(refer Tables 4.3 and 4.4, Figures 4.3 and 4.4). This pattern of impaired coherence between brain and skeletal muscle microcirculation was particularly pronounced in ICU non-survivors, who demonstrated further reductions in both time-frequency coupling and phase synchrony compared to healthy controls in the Cardiac (B6) frequency band (refer Appendix Tables A.2 and A.4). Additionally, wavelet semblance analysis identified significantly disrupted phase synchrony across all three physiological signal pairs: Brain-Skeletal Muscle, Brain-ABP, and Skeletal Muscle-ABP in the Cardiac (B6) frequency band among ICU patients compared to healthy controls (refer Tables 4.4 and Figures 4.4).

5.1.2 Hypothesis 1.2: ICU non-survivors would demonstrate significantly altered physiological coherence of microvascular hemodynamics compared to ICU survivors.

The key findings revealed that ICU Non-survivors have significantly higher semblance values in the Skeletal Muscle-ABP physiological signal pair across the Microvascular frequency band, indicating abnormal and excessive phase synchrony between peripheral microcirculation and systemic blood pressure (refer Table 4.8 and Figure 4.6). In contrast, the remaining signal pairs, Brain-Skeletal Muscle and Brain-ABP, showed no significant time-phasic relationships (refer Table 4.6-4.7 and Figure 4.6). This excessive synchronization was prominently observed in skeletal muscle but not in brain, reflecting the fundamental differences in autoregulatory mechanisms between these organs.

Furthermore, analysis of time-frequency coupling (*%signifCoherenceDuration*) revealed no significant differences between ICU survivors and non-survivors across all three physiological signal pairs (Brain-Skeletal Muscle, Brain-ABP, Skeletal Muscle-ABP) in either Cardiac or Microvascular frequency bands (refer Tables 4.5 and Figure 4.5).

5.2 Comparison with Previous Literature

The finding of this study shows reduced brain-skeletal muscle coherence in ICU patients aligns with previous research on organ-specific microvascular regulation during critical illness. Mirsajadi et al. demonstrated a moderate correlation between NIRS-derived optimal mean arterial pressure values for brain and skeletal muscle, suggesting distinct regulatory mechanisms[24]. This study revealed that both ICU patients and healthy populations exhibit higher time-frequency coupling duration (*%signfCoherenceDuration*) and phase-locked (*Significant Semblance*) relationships

within the cardiac frequency band between the brain and skeletal muscle (see Table 4.3 and Table 4.6). These findings indicate the presence of coordinated and synchronized cardiovascular oscillations derived from the central heart rate, observed within the local hemodynamics of both organs, supporting the moderate brain-muscle MAP correlation observed by Mirsajadi et al.

However, this study extends those findings by revealing that healthy controls exhibit significantly greater *%signfCoherenceDuration* and *Significant Semblance* values in the cardiac frequency band compared to ICU patients. This suggests that the coordination and synchronization of cardiovascular oscillations between these organs becomes decoupled in critical illness, potentially reflecting impaired autoregulatory mechanisms and compromised systemic physiological integration. Altogether, this study extends previous NIRS-based organ-specific MAP correlation studies, providing a more nuanced understanding of microvascular hemodynamic interactions across populations. The methodological shift from time-domain pressure correlation analysis to dynamic time-frequency characterization offers deeper insights into the temporal evolution of organ-specific regulatory mechanisms of microvascular hemodynamics during critical illness.

Building on this broader characterization, the observation of altered skeletal muscle-ABP coherence in non-survivors builds upon findings by Das et al. and Peng et al., who reported associations between tissue oxygenation parameters and adverse outcomes[15,16]. However, this study advances beyond these time domain analysis to characterize dynamic time-frequency microvascular interactions, providing deeper insights into the pathophysiological mechanisms underlying poor outcomes in critically ill patients.

Further supporting this perspective, a study conducted by Mohammadzadeh et al. utilizing wavelet coherence analysis with optical intrinsic signal imaging (OISi) in stroke rat models revealed significant reductions in wavelet coherence between the motor and somatosensory cortices in ischemic hemispheres compared to healthy controls[212]. These findings suggest disrupted functional connectivity and diminished synchronization of cerebral hemodynamic oscillations post-stroke. Thus, wavelet coherence analysis proved to be a sensitive method for detecting frequency-specific connectivity alterations between healthy and pathological states.

Complementing these interspecies and pathological comparisons, the findings of this study also align with Hermans et al.'s investigation into neurovascular coupling[191]. Although both studies employed wavelet coherence to assess physiological relationships, the current research uniquely

explored multi-organ microvascular coherence across a broader range of frequency bands (0.0095–0.16 Hz for microvascular and 0.667–3.1 Hz for cardiac), compared to Hermans et al.'s narrower 0.25–1 mHz focus. Both studies, however, converge on the conclusion that coherence is significantly diminished in adverse clinical conditions, emphasizing the potential of wavelet-based metrics as biomarkers of systemic physiological integrity.

Expanding this analytical scope, the present study also extends the work of Highton et al., who demonstrated dynamic cerebrovascular slow-wave relationships in brain-injured patients using wavelet coherence[27]. While both studies leverage wavelet coherence analysis, the current analysis focuses on brain-skeletal muscle interactions, moving beyond cerebral autoregulation alone. Methodologically, this study advances the application of wavelet semblance analysis to capture phase relationships across both microvascular and cardiac bands. Notably, the identification of higher Skeletal Muscle-ABP wavelet semblance as a significant differentiator between ICU survivors and non-survivors suggests (refer Tables 4.8 and Figures 4.6) that peripheral-central vascular excessive coupling may serve as a critical prognostic marker. This distinction emphasizes the clinical value of integrating multi-site NIRS monitoring to uncover systemic vascular dysfunction not detectable through cerebral focused assessments alone.

Further highlighting the importance of spatial and frequency-specific analysis, Tian et al. demonstrated regional heterogeneity in cerebral hemodynamics using multichannel NIRS in neonates, where MRI detected abnormalities corresponded with localized discrepancies in wavelet coherence measurements[25,26]. Their findings emphasize how coherence metrics can vary across spatial domains and reflect underlying pathological states. Similarly, the present study identifies frequency specific differences in physiological coherence between microvascular signal pairs: brain, skeletal muscle and ABP/NIBP, with ICU patients exhibiting significantly altered coherence patterns compared to healthy controls in microvascular and cardiac frequency bands. These findings reinforce the importance of considering dynamic microvascular interactions between organs.

5.3 Interpretation of Results

Having established the relationship between these findings and existing literature, the physiological significance and clinical implications of the observed microvascular coherence alterations provide a critical foundation for interpreting the results and support the future

applicability of the research hypotheses presented in this thesis. Therefore, Tables 5.1 and 5.2 provide a structured summary of the key findings observed in wavelet coherence and semblance metrics, thereby offering a coherent framework for interpreting these complex dynamics.

Table 5.1: Key Findings Matrix of ICU Patients vs. Healthy Controls.

ICU patients vs. Healthy Control				
Analysis Type	***Frequency bands***	*Physiological Signal pair*		
		Brain-Skeletal Muscle	*Brain-ABP/NIBP*	*Skeletal Muscle-ABP/NIBP*
Wavelet Coherence	**Microvascular**	✕	✕	↑*
	Cardiac	↓*	✕	✕
Wavelet Semblance	Microvascular	✕	✕	✕
	Cardiac	↓*	↓*	↓*

The matrix shows the statistical significance and direction of physiological signal pairs coherence changes in ICU patients relative to healthy controls. ↑* = significantly increased coherence in ICU patients; ↓* = significantly decreased coherence in ICU patients; ✕ = no significant difference ($p < 0.05$, Mann-Whitney U test). Arrows indicate actual directional changes in wavelet coherence and semblance values. ABP = Arterial Blood Pressure; NIBP = Non-invasive Blood Pressure.

Table 5.2 : Key Findings Matrix of ICU Survivors vs. Non-Survivors.

ICU Non-Survivors vs. Survivors				
Analysis Type	***Frequency band***	*Physiological Signal pair*		
		Brain-Skeletal Muscle	Brain-ABP/NIBP	*Skeletal Muscle-ABP/NIBP*
Wavelet Coherence	Microvascular	✕	✕	✕
	Cardiac	✕	✕	✕
Wavelet Semblance	**Microvascular**	✕	✕	↑*
	Cardiac	✕	✕	↓*

The matrix shows the statistical significance and direction of physiological signal pairs coherence changes in ICU Non-Survivors relative to ICU Survivors. ↑* = significantly increased coherence in ICU non-Survivors; ↓* = significantly decreased coherence in ICU non-Survivors; ✕ = no significant difference (all comparisons $p < 0.05$, Mann-Whitney U test). Arrows indicate actual directional changes in wavelet coherence and semblance values. ABP = Arterial Blood Pressure; NIBP = Non-invasive Blood Pressure.

The significant reduction in wavelet coherence and wavelet semblance of Cardiac band between brain and skeletal muscle in ICU patients suggests a fundamental disruption of rapid hemodynamic coupling mechanisms during critical illness compared to healthy controls (refer Tables 4.3-4.4 and Figures 4.3-4.4). The cardiac frequency band represents a central, unifying hemodynamic signal originating from centrally coordinated and synchronized cardiovascular rhythms of the heart, which are transmitted throughout the entire cardiovascular system of the body as pressure and flow waves. In the healthy state, this central cardiac signal creates highly synchronized hemodynamic oscillations across different organs, resulting in strong coherence between brain and skeletal muscle microcirculation in the cardiac frequency band.

During critical illness, this central unifying cardiac signal becomes altered. As demonstrated in the findings of this study (refer Tables 5.1), alteration of central unifying cardiac signal leads to the decoupling of coordinated and synchronized cardiovascular oscillations between brain and skeletal muscle, potentially reflecting impaired autoregulatory mechanisms and disrupted physiological integration. The selective nature of these disruptions, where some coherence patterns (such as the

microvascular frequency band) are preserved while others (cardiac frequency band) are disrupted (refer Tables 4.3-4.4 and Figures 4.3-4.4), suggests that critical illness affects specific regulatory mechanisms rather than causing uniform microvascular dysfunction.

The excessive synchronization between skeletal muscle and systemic blood pressure in both cardiac and microvascular frequency bands, observed in ICU non-survivors compared to ICU survivors, represents a particularly important finding (refer Tables 4.8 and Figures 4.6). This pattern contrasts with the similar physiological signal pair, Brain–ABP, which did not show any significant time-phasic relationships (refer Tables 4.7 and Figures 4.6), highlighting the specific vulnerability of skeletal muscle microvascular hemodynamics in critically ill patients.

The excessive synchronization was significantly observed in skeletal muscle rather than in the brain due to fundamental differences in autoregulatory capacity between these organs. The brain maintains robust cerebral autoregulation, enabling it to preserve microvascular independence from systemic blood pressure fluctuations, even during critical illness. In contrast, skeletal muscle acts as the primary effector of systemic vascular resistance under sympathetic nervous system control and becomes pathologically coupled to systemic hemodynamics when skeletal muscle microvascular regulatory mechanisms fail. This pattern may indicate the loss of local autoregulatory control within the skeletal muscle of ICU non-survivors, resulting in passive pressure-dependent perfusion that compromises the skeletal muscle microcirculation's ability to maintain adequate tissue oxygenation despite fluctuations in systemic hemodynamics. Such maladaptive coupling could contribute to the development of multiple organ dysfunction syndrome by failing to protect tissues from harmful pressure variations.

The frequency-specific nature of these alterations provides insights into the underlying physiological mechanisms. The Microvascular frequency band (0.0095-0.16 Hz) comprises Endothelial, Neurogenic, and Myogenic regulatory mechanisms, while the Cardiac frequency band (0.667-3.1 Hz) reflects rapid cardiovascular oscillations. The differential patterns observed across these frequency ranges suggest that critical illness selectively impairs specific aspects of microvascular regulation while potentially preserving others (refer Tables 5.1 and 5.2).

5.4 Study Limitations

Several methodological constraints limit the interpretation and generalizability of these results. The sample size, particularly for subgroup analyses of ICU survivors and non-survivors, limited the statistical power to detect differences between these groups. This may have contributed to the partial support for Hypothesis 1.2 and the reduced ability to detect nuanced but clinically meaningful differences.

The observational experiment design of this research inherently limits the ability to determine causality between microvascular coherence alterations and clinical outcomes, allowing only for the identification of associative relationships.

The heterogeneous characteristics of the ICU population, including varying diagnoses, comorbidities, and vasopressor requirements, introduce potential confounding variables that could independently influence microvascular function, apart from critical illness severity. While this heterogeneity reflects the reality of ICU populations, it complicates the interpretation of results and their attribution to specific pathophysiological mechanisms.

Technical limitations included challenges with motion artifacts in NIRS recordings, requiring manual artifact removal despite the assistance from automated methods. This process was time-consuming and potentially introduced subjective bias in data selection. The penetration depth of NIRS signals is limited by the thickness of adipose tissue (muscle) and superficial extra-cerebral tissue (brain), which can affect signal quality and comparability between subjects. Although this study excluded patients with a BMI greater than 40 and involved measuring adipose tissue thickness, variations within the acceptable range could still influence the analysis.

The single-center design and specific ICU population studied may limit external validity. Additionally, the healthy control group was younger on average than the ICU population, which could have contributed to observed differences between groups independent of critical illness status.

The analysis presented in this discussion synthesizes that microvascular coherence patterns between brain and skeletal muscle are fundamentally altered during critical illness, with distinct signatures associated with patient outcomes. These findings challenge existing paradigms of uniform microvascular dysregulation and demonstrate the clinical utility of wavelet-based signal

processing in characterizing dynamic physiological relationships in microvascular hemodynamics. The methodological framework established through this research provides a foundation for future investigations into personalized therapeutic strategies based on individual patterns of cross-organ microvascular dysfunction.

6 CHPATER 6 – CONCLUSION

This study establishes, for the first time, that the physiological coherence of microvascular hemodynamics between the brain and skeletal muscle, as well as their relationship with systemic blood pressure, is altered during critical illness, with distinct alterations in coherence is associated with ICU patient outcomes. Through the application of wavelet-based signal processing techniques to high-resolution near-infrared spectroscopy data, this research provides novel insights into the dynamic coordination of microvascular regulation across organ systems.

The primary findings demonstrate that ICU patients exhibit significantly reduced coherence duration and disrupted phase synchrony between brain and skeletal muscle microcirculation in the cardiac frequency band compared to healthy controls, supporting Hypothesis 1.1. This represents the first quantitative characterization of cross-organ microvascular coherence alterations during critical illness, revealing that disease states selectively impair specific regulatory mechanisms within microvascular hemodynamics rather than causing uniform microvascular dysfunction.

Regarding patient outcomes, ICU non-survivors demonstrated excessive synchronization between skeletal muscle microcirculation and systemic blood pressure in the microvascular and cardiac frequency bands, providing support for Hypothesis 1.2. These findings suggest that maladaptive microvascular coupling, characterized by loss of local autoregulatory control and passive pressure-dependent perfusion, may contribute to poor clinical outcomes.

This research makes several important contributions to the field of biomedical engineering and critical care medicine. Methodologically, it establishes a novel analytical framework combining high-resolution NIRS monitoring with wavelet coherence and semblance analyses to quantify dynamic microvascular interactions across organ systems. This approach advances beyond traditional single-organ monitoring approaches to provide both local and system-level understanding of microvascular regulations.

Physiologically, the study challenges the assumption of uniform microvascular dysregulation during critical illness by demonstrating organ-specific and frequency-specific alterations in coherence patterns. The identification of excessive skeletal muscle-systemic pressure coupling in non-survivors provides new insights into potential mechanisms underlying multiple organ dysfunction syndrome.

Clinically, these findings lay the groundwork for developing novel biomarkers for risk stratification and outcome prediction in critical care settings. The demonstrated ability to differentiate between survivors and non-survivors based on microvascular coherence patterns suggests the potential for early identification of patients at high risk of poor outcomes, enabling timely therapeutic interventions.

7 CHPATER 7 – FUTURE DIRECTION

The theoretical contributions and methodological framework established in this study provide a foundation for several important future research directions that could advance both the scientific understanding and clinical application of microvascular coherence monitoring while systematically addressing the limitations observed in the current study.

Therefore, to systematically advance both theoretical understanding and clinical application, future studies should prioritize larger, multi-center study designs that include predefined subgroups based on ICU admission diagnoses. Such an approach would enhance statistical robustness and facilitate a more granular understanding of how varying critical illness etiologies influence microvascular hemodynamics coherence. Additionally, longitudinal studies with more frequent and systematic monitoring throughout the ICU stay are essential for mapping the temporal progression of microvascular dynamics and assessing their responsiveness to clinical interventions. The incorporation of complementary physiological monitoring techniques, such as transcranial Doppler ultrasonography or tissue oxygen tension assessments, could enrich the interpretation of NIRS-derived data and strengthen the physiological validity of observed coherence patterns. Furthermore, examining and evaluating the temporal relationships between microvascular hemodynamics coherence and established biomarkers of organ dysfunction, such as lactate clearance or inflammatory cytokines, may offer deeper insights into the pathophysiological mechanisms at play and improve the clinical utility of coherence as a clinical indicator.

To improve the quality and accuracy of NIRS monitoring data, future studies should consider integrating advanced optical technologies such as time-domain NIRS. or Diffuse Correlation Spectroscopy (DCS). These advanced optical technologies offer significant advantages over conventional CW-NIRS by enabling absolute quantification of microvascular blood flow and enhancing depth resolution. Such capabilities would allow for a more accurate and nuanced characterization of microvascular dynamics, thereby potentially increasing the clinical relevance and applicability of NIRS based findings. In addition, incorporating auxiliary sensors, such as gyroscopes to detect patient movement and temperature sensors to monitor local thermal conditions, could help to identify motion artifacts and assess the influence of temperature fluctuations on NIRS signals in real-time.

Moreover, the development of automated, explainable machine learning (XML)-driven methods integrated with data mining techniques and digital signal processing holds significant potential for improving artifact detection and signal correction in NIRS data. These advanced approaches could streamline preprocessing workflows, enhance the objectivity and reproducibility of data handling, and offer greater transparency in analytical decisions. By minimizing the reliance on manual correction, such systems can reduce human error and bias, ultimately leading to more reliable and clinically actionable insights.

While the current study focused on analyzing global microvascular coherence metrics across entire recording periods for time-frequency and time-phasic microvascular relationships, future studies should focus on evaluating the feasibility of developing real-time anomaly detection algorithms capable of identifying transient alterations in microvascular coherence patterns. By implementing higher temporal resolution analysis windows and adaptive threshold detection methods, future research could enable the early identification of emerging cross-organ microvascular dysfunction before clinically apparent deterioration occurs. Such advances would facilitate the development of predictive monitoring systems that could alert clinicians to impending organ dysfunction based on subtle changes in microvascular coherence patterns, potentially enabling proactive therapeutic interventions.

REFERENCES

1. Caro CG. *The Mechanics of the Circulation*. Cambridge University Press; 2012.

2. Guven G, Hilty MP, Ince C. Microcirculation: Physiology, Pathophysiology, and Clinical Application. *Blood Purification*. 2019;49(1-2):143-150. doi:10.1159/000503775

3. Froese L, Batson C, Gomez A, Dian J, Zeiler FA. The Limited Impact of Current Therapeutic Interventions on Cerebrovascular Reactivity in Traumatic Brain Injury: A Narrative Overview. *Neurocrit Care*. 2021;34(1):325-335. doi:10.1007/s12028-020-01003-4

4. Mendelson AA, Erickson D, Villar R. The role of the microcirculation and integrative cardiovascular physiology in the pathogenesis of ICU-acquired weakness. *Front Physiol*. 2023;14. doi:10.3389/fphys.2023.1170429

5. Sakka SG. Hemodynamic Monitoring in the Critically Ill Patient – Current Status and Perspective. *Front Med (Lausanne)*. 2015;2:44. doi:10.3389/fmed.2015.00044

6. Valeanu L, Bubenek-Turconi SI, Ginghina C, Balan C. Hemodynamic Monitoring in Sepsis—A Conceptual Framework of Macro- and Microcirculatory Alterations. *Diagnostics (Basel)*. 2021;11(9):1559. doi:10.3390/diagnostics11091559

7. Pinsky MR, Payen D. Functional hemodynamic monitoring. *Crit Care*. 2005;9(6):566-572. doi:10.1186/cc3927

8. Muzaffar SN, Pradhan A, Siddiqui SS, Roy S, Suresh T. Monitoring Macro- and Microcirculation in the Critically Ill: A Narrative Review. *Avicenna J Med*. 2023;13(3):138-150. doi:10.1055/s-0043-1772175

9. Verdant CL. From bench to bedside. *Critical Care*. 2012;16(4):136. doi:10.1186/cc11394

10. Ince C. The microcirculation is the motor of sepsis. *Crit Care*. 2005;9(Suppl 4):S13-S19. doi:10.1186/cc3753

11. Ait-Oufella H, Lemoinne S, Boelle PY, et al. Mottling score predicts survival in septic shock. *Intensive Care Med*. 2011;37(5):801-807. doi:10.1007/s00134-011-2163-y

12. Dumas G, Lavillegrand JR, Joffre J, et al. Mottling score is a strong predictor of 14-day mortality in septic patients whatever vasopressor doses and other tissue perfusion parameters. *Crit Care*. 2019;23(1):211. doi:10.1186/s13054-019-2496-4

13. Hariri G, Joffre J, Leblanc G, et al. Narrative review: clinical assessment of peripheral tissue perfusion in septic shock. *Ann Intensive Care*. 2019;9:37. doi:10.1186/s13613-019-0511-1

14. Zampieri FG, Damiani LP, Bakker J, et al. Effects of a Resuscitation Strategy Targeting Peripheral Perfusion Status versus Serum Lactate Levels among Patients with Septic Shock. A

Bayesian Reanalysis of the ANDROMEDA-SHOCK Trial. *Am J Respir Crit Care Med*. 2020;201(4):423-429. doi:10.1164/rccm.201905-0968OC

15. Das BP, Sharma M, Bansal S, Philip M, Umamaheswara Rao GS. Prognostic Value of Tissue Oxygen Monitoring and Regional Cerebral Oxygen Saturation Monitoring and Their Correlation in Neurological Patients with Sepsis: A Preliminary, Prospective, Observational Study. *J Neurosurg Anesthesiol*. 2020;32(1):77-81. doi:10.1097/ANA.0000000000000563

16. Peng Q, Zhang L, Ai M, Huang L, Ai Y. Clinical values of cerebral oxygen saturation monitoring in patients with septic shock. *Zhong Nan Da Xue Xue Bao Yi Xue Ban*. 2021;46(11):1212-1219. doi:10.11817/j.issn.1672-7347.2021.200905

17. Feng Q, Ai M, Huang L, Peng Q, Ai Y, Zhang L. Relationship Between Cerebral Hemodynamics, Tissue Oxygen Saturation, and Delirium in Patients With Septic Shock: A Pilot Observational Cohort Study. *Front Med (Lausanne)*. 2021;8:641104. doi:10.3389/fmed.2021.641104

18. Mesquida J, Gruartmoner G, Espinal C. Skeletal Muscle Oxygen Saturation (StO2) Measured by Near-Infrared Spectroscopy in the Critically Ill Patients. *Biomed Res Int*. 2013;2013:502194. doi:10.1155/2013/502194

19. Bennett SR, Abukhodair AW, Alqarni MS, Fernandez JA, Fernandez AJ, Bennett MR. Outcomes in Cardiac Surgery Based on Preoperative, Mean Intraoperative and Stratified Cerebral Oximetry Values. *Cureus*. 13(8):e17123. doi:10.7759/cureus.17123

20. Bakker A, Smith B, Ainslie P, et al. Near-Infrared Spectroscopy. In: *Applied Aspects of Ultrasonography in Humans*. IntechOpen; 2012. doi:10.5772/32493

21. Huang Z, Zhang H, Huang Z, Zhang H. *Near-Infrared Spectroscopy Technique and Its Application in Biomedical Fields*. IntechOpen; 2025. doi:10.5772/intechopen.1006840

22. Barstow TJ. Understanding near infrared spectroscopy and its application to skeletal muscle research. *J Appl Physiol (1985)*. 2019;126(5):1360-1376. doi:10.1152/japplphysiol.00166.2018

23. Fan JL, Wu TY, Lovering AT, Nan L, Bang WL, Kayser B. Differential Brain and Muscle Tissue Oxygenation Responses to Exercise in Tibetans Compared to Han Chinese. *Front Physiol*. 2021;12:617954. doi:10.3389/fphys.2021.617954

24. Mirsajadi A, Erickson D, Alias S, et al. Microvascular Autoregulation in Skeletal Muscle Using Near-Infrared Spectroscopy and Derivation of Optimal Mean Arterial Pressure in the ICU: Pilot Study and Comparison With Cerebral Near-Infrared Spectroscopy. *Critical Care Explorations*. 2024;6(7):e1111. doi:10.1097/CCE.0000000000001111

25. Tian F, Sepulveda P, Kota S, et al. Regional heterogeneity of cerebral hemodynamics in mild neonatal encephalopathy measured with multichannel near-infrared spectroscopy. *Pediatr Res*. 2021;89(4):882-888. doi:10.1038/s41390-020-0992-5

26. Tian F, Tarumi T, Liu H, Zhang R, Chalak L. Wavelet coherence analysis of dynamic cerebral autoregulation in neonatal hypoxic-ischemic encephalopathy. *Neuroimage Clin*. 2016;11:124-132. doi:10.1016/j.nicl.2016.01.020

27. Highton D, Ghosh A, Tachtsidis I, Panovska-Griffiths J, Elwell CE, Smith M. Monitoring Cerebral Autoregulation After Brain Injury: Multimodal Assessment of Cerebral Slow-Wave Oscillations Using Near-Infrared Spectroscopy. *Anesth Analg*. 2015;121(1):198-205. doi:10.1213/ANE.0000000000000790

28. Peate I. Anatomy and physiology, 8. The circulatory system. *British Journal of Healthcare Assistants*. 2018;12(2):62-67. doi:10.12968/bjha.2018.12.2.62

29. Pittman RN. The Circulatory System and Oxygen Transport. In: *Regulation of Tissue Oxygenation*. Morgan & Claypool Life Sciences; 2011. Accessed February 7, 2025. https://www.ncbi.nlm.nih.gov/books/NBK54112/

30. Wilcken DEL. Physiology of the normal heart. *Medicine*. 2010;38(7):336-339. doi:10.1016/j.mpmed.2010.03.014

31. Faoro V, Forton K, Faoro V, Forton K. Pulmonary Vascular Reserve and Aerobic Exercise Capacity. In: *Interventional Pulmonology and Pulmonary Hypertension - Updates on Specific Topics*. IntechOpen; 2019. doi:10.5772/intechopen.88399

32. Pulmonary artery banding. *The Journal of Thoracic and Cardiovascular Surgery*. 1984;88(5):645-653. doi:10.1016/S0022-5223(19)35431-5

33. Diez-Silva M, Dao M, Han J, Lim CT, Suresh S. Shape and Biomechanical Characteristics of Human Red Blood Cells in Health and Disease. *MRS Bulletin*. 2010;35(5):382-388. doi:10.1557/mrs2010.571

34. Tombak A. Introductory Chapter: Erythrocytes - Basis of Life. In: *Erythrocyte*. IntechOpen; 2019. doi:10.5772/intechopen.88847

35. Vieira-de-Abreu A, Campbell RA, Weyrich AS, Zimmerman GA. Platelets: versatile effector cells in hemostasis, inflammation, and the immune continuum. *Semin Immunopathol*. 2012;34(1):5-30. doi:10.1007/s00281-011-0286-4

36. Rhodes CE, Denault D, Varacallo M. Physiology, Oxygen Transpor. Published online 2023. Accessed February 7, 2025. https://www.ncbi.nlm.nih.gov/books/NBK538336

37. Hilpert P, Fleischmann RG, Kempe D, Bartels H. The Bohr effect related to blood and erythrocyte pH. *American Journal of Physiology-Legacy Content*. 1963;205(2):337-340. doi:10.1152/ajplegacy.1963.205.2.337

38. Jensen FB. Red blood cell pH, the Bohr effect, and other oxygenation-linked phenomena in blood O2 and CO2 transport. *Acta Physiologica Scandinavica*. 2004;182(3):215-227. doi:10.1111/j.1365-201X.2004.01361.x

39. Secomb TW. Hemodynamics. *Compr Physiol*. 2016;6(2):975-1003. doi:10.1002/cphy.c150038

40. Physiology and pathobiology of the microcirculation. *American Journal of Otolaryngology*. 1988;9(6):264-277. doi:10.1016/S0196-0709(88)80035-8

41. Abbas K, Lu Y, Bavishi S, et al. A Simple Review of Small Vessel Disease Manifestation in the Brain, Retina, and Kidneys. *J Clin Med*. 2022;11(19):5546. doi:10.3390/jcm11195546

42. Kwiatkowska E, Kwiatkowski S, Dziedziejko V, Tomasiewicz I, Domański L. Renal Microcirculation Injury as the Main Cause of Ischemic Acute Kidney Injury Development. *Biology (Basel)*. 2023;12(2):327. doi:10.3390/biology12020327

43. De Backer D, Donadello K, Taccone FS, Ospina-Tascon G, Salgado D, Vincent JL. Microcirculatory alterations: potential mechanisms and implications for therapy. *Ann Intensive Care*. 2011;1:27. doi:10.1186/2110-5820-1-27

44. De Backer D, Orbegozo Cortes D, Donadello K, Vincent JL. Pathophysiology of microcirculatory dysfunction and the pathogenesis of septic shock. *Virulence*. 2014;5(1):73-79. doi:10.4161/viru.26482

45. Moore JPR, Dyson A, Singer M, Fraser J. Microcirculatory dysfunction and resuscitation: why, when, and how. *Br J Anaesth*. 2015;115(3):366-375. doi:10.1093/bja/aev163

46. Østergaard L, Granfeldt A, Secher N, et al. Microcirculatory dysfunction and tissue oxygenation in critical illness. *Acta Anaesthesiol Scand*. 2015;59(10):1246-1259. doi:10.1111/aas.12581

47. Gourdin M, Dubois P, Gourdin M, Dubois P. Impact of Ischemia on Cellular Metabolism. In: *Artery Bypass*. IntechOpen; 2013. doi:10.5772/54509

48. Kim WY, Ivan M. Molecular responses to hypoxia: ancient pathways, clinical promises. *J Cell Mol Med*. 2009;13(9a):2757-2758. doi:10.1111/j.1582-4934.2009.00882.x

49. Mayer K, Trzeciak S, Puri NK. Assessment of the adequacy of oxygen delivery. *Current Opinion in Critical Care*. 2016;22(5):437. doi:10.1097/MCC.0000000000000336

50. Ellis CG, Jagger J, Sharpe M. The microcirculation as a functional system. *Crit Care*. 2005;9 Suppl 4(Suppl 4):S3-8. doi:10.1186/cc3751

51. Segal SS. Regulation of blood flow in the microcirculation. *Microcirculation*. 2005;12(1):33-45. doi:10.1080/10739680590895028

52. Jones S, D'Silva A, Bhuva A, et al. Improved Exercise-Related Skeletal Muscle Oxygen Consumption Following Uptake of Endurance Training Measured Using Near-Infrared Spectroscopy. *Front Physiol*. 2017;8:1018. doi:10.3389/fphys.2017.01018

53. Pittman RN. Oxygen Transport in the Microcirculation and Its Regulation. *Microcirculation*. 2013;20(2):117-137. doi:10.1111/micc.12017

54. Korthuis RJ. *Skeletal Muscle Circulation*. Morgan & Claypool Life Sciences; 2011. Accessed February 8, 2025. http://www.ncbi.nlm.nih.gov/books/NBK57141/

55. Ballabh P, Braun A, Nedergaard M. The blood-brain barrier: an overview: structure, regulation, and clinical implications. *Neurobiol Dis*. 2004;16(1):1-13. doi:10.1016/j.nbd.2003.12.016

56. Blood–Brain Barrier: Physiological and Functional Considerations. In: *Handbook of Developmental Neurotoxicology*. Academic Press; 2018:229-236. doi:10.1016/B978-0-12-809405-1.00020-1

57. Longden TA, Zhao G, Hariharan A, Lederer WJ. Pericytes and the Control of Blood Flow in Brain and Heart. *Annual Review of Physiology*. 2023;85(Volume 85, 2023):137-164. doi:10.1146/annurev-physiol-031522-034807

58. Cipolla MJ. *The Cerebral Circulation*. Morgan & Claypool Life Sciences; 2009. Accessed February 8, 2025. http://www.ncbi.nlm.nih.gov/books/NBK53081/

59. Pardridge W. Targeted delivery of protein and gene medicines through the blood–brain barrier. *Clinical Pharmacology & Therapeutics*. 2015;97(4):347-361. doi:10.1002/cpt.18

60. Agarwal N, Carare RO. Cerebral Vessels: An Overview of Anatomy, Physiology, and Role in the Drainage of Fluids and Solutes. *Front Neurol*. 2021;11. doi:10.3389/fneur.2020.611485

61. Hoque MM, Abdelazim H, Jenkins-Houk C, Wright D, Patel BM, Chappell JC. The Cerebral Microvasculature: Basic and Clinical Perspectives on Stroke and Glioma. *Microcirculation*. 2021;28(3):e12671. doi:10.1111/micc.12671

62. Lassen NA. Control of cerebral circulation in health and disease. *Circ Res*. 1974;34(6):749-760. doi:10.1161/01.res.34.6.749

63. Lassen NA. Cerebral blood flow and oxygen consumption in man. *Physiol Rev*. 1959;39(2):183-238. doi:10.1152/physrev.1959.39.2.183

64. Hossmann KA. Pathophysiology and therapy of experimental stroke. *Cell Mol Neurobiol*. 2006;26(7-8):1057-1083. doi:10.1007/s10571-006-9008-1

65. Kelly DF, Kordestani RK, Martin NA, et al. Hyperemia following traumatic brain injury: relationship to intracranial hypertension and outcome. *J Neurosurg*. 1996;85(5):762-771. doi:10.3171/jns.1996.85.5.0762

66. Lassen NA. The luxury-perfusion syndrome and its possible relation to acute metabolic acidosis localised within the brain. *Lancet*. 1966;2(7473):1113-1115. doi:10.1016/s0140-6736(66)92199-4

67. Martin NA, Patwardhan RV, Alexander MJ, et al. Characterization of cerebral hemodynamic phases following severe head trauma: hypoperfusion, hyperemia, and vasospasm. *J Neurosurg*. 1997;87(1):9-19. doi:10.3171/jns.1997.87.1.0009

68. Girouard H, Iadecola C. Neurovascular coupling in the normal brain and in hypertension, stroke, and Alzheimer disease. *Journal of Applied Physiology*. 2006;100(1):328-335. doi:10.1152/japplphysiol.00966.2005

69. Phillips AA, Chan FH, Zheng MMZ, Krassioukov AV, Ainslie PN. Neurovascular coupling in humans: Physiology, methodological advances and clinical implications. *J Cereb Blood Flow Metab*. 2016;36(4):647-664. doi:10.1177/0271678X15617954

70. Nippert AR, Biesecker KR, Newman EA. Mechanisms Mediating Functional Hyperemia in the Brain. *Neuroscientist*. 2018;24(1):73-83. doi:10.1177/1073858417703033

71. Howarth C. The contribution of astrocytes to the regulation of cerebral blood flow. *Front Neurosci*. 2014;8. doi:10.3389/fnins.2014.00103

72. Lundberg A, Lind E, Olsson H, Helms G, Knutsson L, Wirestam R. Comparison of MRI methods for measuring whole-brain oxygen extraction fraction under different geometric conditions at 7T. *Journal of Neuroimaging*. 2022;32(3):442-458. doi:10.1111/jon.12975

73. Qin Q, Grgac K, van Zijl PCM. Determination of whole-brain oxygen extraction fractions by fast measurement of blood T2 in the jugular vein. *Magn Reson Med*. 2011;65(2):471-479. doi:10.1002/mrm.22556

74. Ito H, Kanno I, Kato C, et al. Database of normal human cerebral blood flow, cerebral blood volume, cerebral oxygen extraction fraction and cerebral metabolic rate of oxygen measured by positron emission tomography with 15O-labelled carbon dioxide or water, carbon monoxide and oxygen: a multicentre study in Japan. *Eur J Nucl Med Mol Imaging*. 2004;31(5):635-643. doi:10.1007/s00259-003-1430-8

75. Yamaguchi T, Kanno I, Uemura K, et al. Reduction in regional cerebral metabolic rate of oxygen during human aging. *Stroke*. 1986;17(6):1220-1228. doi:10.1161/01.STR.17.6.1220

76. Jiang D, Lu H. Cerebral oxygen extraction fraction MRI: Techniques and applications. *Magn Reson Med*. 2022;88(2):575-600. doi:10.1002/mrm.29272

77. Murao M, Kudomi N, Mitamura K, et al. Appearance time of blood in the brain as a possible indicator of oxygen extraction fraction: a feasibility study. *EJNMMI Res*. 2024;14:97. doi:10.1186/s13550-024-01160-z

78. Tsai AG, Johnson PC, Intaglietta M. Oxygen Gradients in the Microcirculation. *Physiological Reviews*. 2003;83(3):933-963. doi:10.1152/physrev.00034.2002

79. Kuperberg SJ, Wadgaonkar R. Sepsis-Associated Encephalopathy: The Blood–Brain Barrier and the Sphingolipid Rheostat. *Front Immunol*. 2017;8. doi:10.3389/fimmu.2017.00597

80. Iacobone E, Bailly-Salin J, Polito A, Friedman D, Stevens RD, Sharshar T. Sepsis-associated encephalopathy and its differential diagnosis. *Critical Care Medicine*. 2009;37(10):S331. doi:10.1097/CCM.0b013e3181b6ed58

81. Rivera-Lara L. The role of impaired brain perfusion in septic encephalopathy. *Critical Care*. 2019;23(1):54. doi:10.1186/s13054-018-2299-z

82. Huang M, Gedansky A, Hassett CE, et al. Pathophysiology of Brain Injury and Neurological Outcome in Acute Respiratory Distress Syndrome: A Scoping Review of Preclinical to Clinical Studies. *Neurocrit Care*. 2021;35(2):518-527. doi:10.1007/s12028-021-01309-x

83. Matthay MA, Zemans RL. The Acute Respiratory Distress Syndrome: Pathogenesis and Treatment. *Annu Rev Pathol*. 2011;6:147-163. doi:10.1146/annurev-pathol-011110-130158

84. Walker AC, Johnson NJ. Critical Care of the Post–Cardiac Arrest Patient. *Cardiology Clinics*. 2018;36(3):419-428. doi:10.1016/j.ccl.2018.03.009

85. L L, X W, Z Y. Ischemia-reperfusion Injury in the Brain: Mechanisms and Potential Therapeutic Strategies. *Biochem Pharmacol (Los Angel)*. 2016;5(4):213. doi:10.4172/2167-0501.1000213

86. Sonnier M, Rittenberger JC. State-of-the-art considerations in post-arrest care. *JACEP Open*. 2020;1(2):107-116. doi:10.1002/emp2.12022

87. Haddad SH, Arabi YM. Critical care management of severe traumatic brain injury in adults. *Scandinavian Journal of Trauma, Resuscitation and Emergency Medicine*. 2012;20(1):12. doi:10.1186/1757-7241-20-12

88. Czosnyka M, Smielewski P, Kirkpatrick P, Menon DK, Pickard JD. Monitoring of cerebral autoregulation in head-injured patients. *Stroke*. 1996;27(10):1829-1834. doi:10.1161/01.str.27.10.1829

89. Carney N, Totten AM, O'Reilly C, et al. Guidelines for the Management of Severe Traumatic Brain Injury, Fourth Edition. *Neurosurgery*. 2017;80(1):6. doi:10.1227/NEU.0000000000001432

90. Chesnut R, Aguilera S, Buki A, et al. A management algorithm for adult patients with both brain oxygen and intracranial pressure monitoring: the Seattle International Severe Traumatic Brain Injury Consensus Conference (SIBICC). *Intensive Care Med*. 2020;46(5):919-929. doi:10.1007/s00134-019-05900-x

91. Hawryluk GWJ, Aguilera S, Buki A, et al. A management algorithm for patients with intracranial pressure monitoring: the Seattle International Severe Traumatic Brain Injury Consensus Conference (SIBICC). *Intensive Care Med*. 2019;45(12):1783-1794. doi:10.1007/s00134-019-05805-9

92. Mendelson AA, Milkovich S, Hunter T, et al. The capillary fascicle in skeletal muscle: Structural and functional physiology of RBC distribution in capillary networks. *The Journal of Physiology*. 2021;599(8):2149-2168. doi:10.1113/JP281172

93. Poole DC. Spatial matching of microvascular oxygen delivery to demand in skeletal muscle: Has the missing link been found? *The Journal of Physiology*. 2021;599(8):2127-2128. doi:10.1113/JP281518

94. Gliemann L, Vestergaard Hansen C, Rytter N, Hellsten Y. Regulation of skeletal muscle blood flow during exercise. *Current Opinion in Physiology*. 2019;10:146-155. doi:10.1016/j.cophys.2019.05.001

95. Thomas GD, Segal SS. Neural control of muscle blood flow during exercise. *Journal of Applied Physiology*. 2004;97(2):731-738. doi:10.1152/japplphysiol.00076.2004

96. Casey DP, Hart EC. Citation for: Cardiovascular function in humans during exercise: role of the muscle pump. *The Physiological Society*. Accessed February 8, 2025. https://physoc.onlinelibrary.wiley.com/action/showCitFormats?doi=10.1113%2Fjphysiol.2008.162123&mobileUi=0

97. Kindig CA, Richardson TE, Poole DC. Skeletal muscle capillary hemodynamics from rest to contractions: implications for oxygen transfer. *J Appl Physiol (1985)*. 2002;92(6):2513-2520. doi:10.1152/japplphysiol.01222.2001

98. Richardson TE, Kindig CA, Musch TI, Poole DC. Effects of chronic heart failure on skeletal muscle capillary hemodynamics at rest and during contractions. *J Appl Physiol (1985)*. 2003;95(3):1055-1062. doi:10.1152/japplphysiol.00308.2003

99. Poole DC, Hirai DM, Copp SW, Musch TI. Muscle oxygen transport and utilization in heart failure: implications for exercise (in)tolerance. *Am J Physiol Heart Circ Physiol*. 2012;302(5):H1050-1063. doi:10.1152/ajpheart.00943.2011

100. Zamani P, Rawat D, Shiva-Kumar P, et al. Effect of inorganic nitrate on exercise capacity in heart failure with preserved ejection fraction. *Circulation*. 2015;131(4):371-380; discussion 380. doi:10.1161/CIRCULATIONAHA.114.012957

101. Pittman RN. Influence of Microvascular Architecture on Oxygen Exchange in Skeletal Muscle. *Microcirculation*. 1995;2(1):1-18. doi:10.3109/10739689509146755

102. Salathe EP, Gorman AD. Modeling Oxygen concentration in skeletal muscle. *Mathematical and Computer Modelling*. 1997;26(4):91-102. doi:10.1016/S0895-7177(97)00147-7

103. Wittenberg BA, Wittenberg JB. Transport of oxygen in muscle. *Annu Rev Physiol*. 1989;51:857-878. doi:10.1146/annurev.ph.51.030189.004233

104. Callahan LA, Supinski GS. Sepsis-induced myopathy. *Critical Care Medicine*. 2009;37(10):S354. doi:10.1097/CCM.0b013e3181b6e439

105. Puthucheary Z, Harridge S, Hart N. Skeletal muscle dysfunction in critical care: Wasting, weakness, and rehabilitation strategies. *Critical Care Medicine*. 2010;38(10):S676. doi:10.1097/CCM.0b013e3181f2458d

106. Schefold JC, Bierbrauer J, Weber-Carstens S. Intensive care unit-acquired weakness (ICUAW) and muscle wasting in critically ill patients with severe sepsis and septic shock. *J Cachexia Sarcopenia Muscle*. 2010;1(2):147-157. doi:10.1007/s13539-010-0010-6

107. Marshall JC. The multiple organ dysfunction syndrome. In: *Surgical Treatment: Evidence-Based and Problem-Oriented*. Zuckschwerdt; 2001. Accessed February 9, 2025. https://www.ncbi.nlm.nih.gov/books/NBK6868/

108. Brealey D, Singer M. Multi-organ dysfunction in the critically ill: epidemiology, pathophysiology and management. *J R Coll Physicians Lond*. 2000;34(5):424-427.

109. Dittmer DK, Teasell R. Complications of immobilization and bed rest. Part 1: Musculoskeletal and cardiovascular complications. *Can Fam Physician*. 1993;39:1428-1432, 1435-1437.

110. Teasell R, Dittmer DK. Complications of immobilization and bed rest. Part 2: Other complications. *Can Fam Physician*. 1993;39:1440-1442, 1445-1446.

111. Hermans G, De Jonghe B, Bruyninckx F, Berghe GV den. Clinical review: Critical illness polyneuropathy and myopathy. *Critical Care*. 2008;12(6):238. doi:10.1186/cc7100

112. Bolton CF. Neuromuscular manifestations of critical illness. *Muscle Nerve*. 2005;32(2):140-163. doi:10.1002/mus.20304

113. Eržen I, Janáček J, Kubínová L. Characterization of the capillary network in skeletal muscles from 3D data. *Physiol Res*. 2011;60(1):1-13. doi:10.33549/physiolres.931988

114. Armstead WM. Cerebral Blood Flow Autoregulation and Dysautoregulation. *Anesthesiology Clinics*. 2016;34(3):465-477. doi:10.1016/j.anclin.2016.04.002

115. Lima A, Bakker J. Clinical monitoring of peripheral perfusion: there is more to learn. *Critical Care*. 2014;18(1):113. doi:10.1186/cc13738

116. Willie CK, Tzeng YC, Fisher JA, Ainslie PN. Integrative regulation of human brain blood flow. *The Journal of Physiology*. 2014;592(5):841-859. doi:10.1113/jphysiol.2013.268953

117. Meyer JS, Gilroy J. Regulation and Adjustment of the Cerebral Circulation. *Diseases of the Chest*. 1968;53(1):30-37. doi:10.1378/chest.53.1.30

118. Wagner EM, Traystman RJ. Hydrostatic determinants of cerebral perfusion. *Critical Care Medicine*. 1986;14(5):484.

119. Magder S. The meaning of blood pressure. *Crit Care*. 2018;22(1):257. doi:10.1186/s13054-018-2171-1

120. Chance B, Cooper CE, Delpy DT, Reynolds EOR, Reynolds EOR. Preface for a Discussion on Near–infrared spectroscopy and imaging of living systems. *Philosophical Transactions of the Royal Society of London Series B: Biological Sciences*. 1997;352(1354):645-645. doi:10.1098/rstb.1997.0044

121. Chance B, Cooper CE, Delpy DT, Reynolds EOR, Cooper C, Delpy DT. Introduction to a Discussion on Near–infrared spectroscopy and imaging of living systems. *Philosophical Transactions of the Royal Society of London Series B: Biological Sciences*. 1997;352(1354):647-648. doi:10.1098/rstb.1997.0045

122. Izzetoglu M, Bunce SC, Izzetoglu K, Onaral B, Pourrezaei K. Functional brain imaging using near-infrared technology. *IEEE Eng Med Biol Mag*. 2007;26(4):38-46. doi:10.1109/memb.2007.384094

123. Myllylä TS, Ilvesmäki M, Moradi S, et al. Dynamics of human cerebral fluids measured by near-infrared spectroscopy. In: Zalevsky Z, Tuchin VV, Leahy MJ, Wang RK, eds. *Dynamics and Fluctuations in Biomedical Photonics XX*. SPIE; 2023:9. doi:10.1117/12.2650582

124. Botero Fernandez V, Hoyos Carvajal LM, Marín Ortiz JC. Detection of significant wavelengths for identifying and classifying Fusarium oxysporum during the incubation period and water stress in Solanum lycopersicum plants using reflectance spectroscopy. *Journal of Plant Protection Research; 2019; vol 59; No 2; 244–254*. Published online 2019. Accessed February 6, 2025. https://journals.pan.pl/dlibra/publication/129290/edition/112837

125. Jöbsis FF. Noninvasive, infrared monitoring of cerebral and myocardial oxygen sufficiency and circulatory parameters. *Science*. 1977;198(4323):1264-1267. doi:10.1126/science.929199

126. Wray S, Cope M, Delpy DT, Wyatt JS, Reynolds EO. Characterization of the near infrared absorption spectra of cytochrome aa3 and haemoglobin for the non-invasive monitoring of cerebral oxygenation. *Biochim Biophys Acta*. 1988;933(1):184-192. doi:10.1016/0005-2728(88)90069-2

127. Scholkmann F, Kleiser S, Metz AJ, et al. A review on continuous wave functional near-infrared spectroscopy and imaging instrumentation and methodology. *Neuroimage*. 2014;85 Pt 1:6-27. doi:10.1016/j.neuroimage.2013.05.004

128. Fantini S. Dynamic model for the tissue concentration and oxygen saturation of hemoglobin in relation to blood volume, flow velocity, and oxygen consumption: Implications for functional neuroimaging and coherent hemodynamics spectroscopy (CHS). *Neuroimage*. 2014;85 Pt 1(0 1):202-221. doi:10.1016/j.neuroimage.2013.03.065

129. Mendelson AA, Rajaram A, Bainbridge D, et al. Dynamic tracking of microvascular hemoglobin content for continuous perfusion monitoring in the intensive care unit: pilot feasibility study. *J Clin Monit Comput*. 2021;35(6):1453-1465. doi:10.1007/s10877-020-00611-x

130. Palmer KF, Williams D. Optical properties of water in the near infrared*. *J Opt Soc Am, JOSA*. 1974;64(8):1107-1110. doi:10.1364/JOSA.64.001107

131. Beer. Bestimmung der Absorption des rothen Lichts in farbigen Flüssigkeiten. *Annalen der Physik*. 1852;162(5):78-88. doi:10.1002/andp.18521620505

132. Lambert JH. *J.H. Lambert ... Photometria Sive De Mensura Et Gradibus Luminis, Colorum Et Umbrae*. Klett; 1760. Accessed May 5, 2025. urn:nbn:de:bsz:14-db-id3706071398

133. Delpy DT, Cope M, van der Zee P, Arridge S, Wray S, Wyatt J. Estimation of optical pathlength through tissue from direct time of flight measurement. *Phys Med Biol*. 1988;33(12):1433-1442. doi:10.1088/0031-9155/33/12/008

134. Delpy DT, Cope M. Quantification in tissue near-infrared spectroscopy. *Philos Trans R Soc Lond B Biol Sci*. 1997;352(1354):649-659. doi:10.1098/rstb.1997.0046

135. Perrey S. Non-invasive NIR spectroscopy of human brain function during exercise. *Methods*. 2008;45(4):289-299. doi:10.1016/j.ymeth.2008.04.005

136. Chance B, Maris MB, Sorge J, Zhang MZ. Phase modulation system for dual wavelength difference spectroscopy of hemoglobin deoxygenation in tissues. 1990;1204:481-491. doi:10.1117/12.17711

137. Neto AS, Pereira VGM, Manetta JA, Espósito DC, Schultz MJ. Association between static and dynamic thenar near-infrared spectroscopy and mortality in patients with sepsis: a systematic review and meta-analysis. *J Trauma Acute Care Surg*. 2014;76(1):226-233. doi:10.1097/TA.0b013e3182a9221f

138. Collet M, Huot B, Barthélémy R, et al. Influence of systemic hemodynamics on microcirculation during sepsis. *J Crit Care*. 2019;52:213-218. doi:10.1016/j.jcrc.2019.05.002

139. Samraj RS, Lopez-Colon D, Kerrigan M, et al. Thenar Muscle Oxygen Saturation Using Vascular Occlusion Test: A Novel Technique to Study Microcirculatory Abnormalities in Pediatric Heart Failure Patients. *Pediatr Cardiol*. 2019;40(6):1151-1158. doi:10.1007/s00246-019-02118-y

140. M.d AJM. Near infrared spectroscopy of the central nervous system: monitoring oxygenation in the neonatal brain and in the spinal cord following traumatic injury. In: *Biophotonics in Exercise Science, Sports Medicine, Health Monitoring Technologies, and Wearables IV*. Vol 12375. SPIE; 2023:30-43. doi:10.1117/12.2659206

141. Lange F, Tachtsidis I. Clinical Brain Monitoring with Time Domain NIRS: A Review and Future Perspectives. *Applied Sciences*. 2019;9(8):1612. doi:10.3390/app9081612

142. Gomez A, Dian J, Zeiler FA. Continuous and entirely non-invasive method for cerebrovascular reactivity assessment: technique and implications. *J Clin Monit Comput*. 2021;35(2):307-315. doi:10.1007/s10877-020-00472-4

143. Gomez A, Froese L, Bergmann T, et al. P.119 NIRS regional oxygen saturation based cerebrovascular reactivity in the recovery from moderate/severe TBI. *Canadian Journal of Neurological Sciences*. 2024;51(s1):S48-S49. doi:10.1017/cjn.2024.221

144. Sainbhi AS, Vakitbilir N, Gomez A, Stein KY, Froese L, Zeiler FA. Non-Invasive Mapping of Cerebral Autoregulation Using Near-Infrared Spectroscopy: A Study Protocol. *Methods and Protocols*. 2023;6(3):58. doi:10.3390/mps6030058

145. Rivera-Lara L, Geocadin R, Zorrilla-Vaca A, et al. Near-infrared Spectroscopy–derived Cerebral Autoregulation Indices Independently Predict Clinical Outcome in Acutely Ill Comatose Patients. *Journal of Neurosurgical Anesthesiology*. 2020;32(3):234. doi:10.1097/ANA.0000000000000589

146. Cody N, Bradbury I, McMullan RR, et al. Physiologic Determinants of Near-Infrared Spectroscopy-Derived Cerebral and Tissue Oxygen Saturation Measurements in Critically Ill Patients. *Crit Care Explor*. 2024;6(5):e1094. doi:10.1097/CCE.0000000000001094

147. Cohen L. *Time-Frequency Analysis: Theory and Applications*. Prentice-Hall, Inc.; 1995.

148. Daubechies I. The wavelet transform, time-frequency localization and signal analysis. *IEEE Transactions on Information Theory*. 1990;36(5):961-1005. doi:10.1109/18.57199

149. Mallat SG. *A Wavelet Tour of Signal Processing*. Academic Press; 1998.

150. Flandrin P. *Time-Frequency/Time-Scale Analysis*. Academic Press; 1998.

151. Raez MBI, Hussain MS, Mohd-Yasin F. Techniques of EMG signal analysis: detection, processing, classification and applications. *Biol Proced Online*. 2006;8:11-35. doi:10.1251/bpo115

152. Thewissen L, Caicedo A, Lemmers P, Van Bel F, Van Huffel S, Naulaers G. Measuring Near-Infrared Spectroscopy Derived Cerebral Autoregulation in Neonates: From Research Tool Toward Bedside Multimodal Monitoring. *Front Pediatr*. 2018;6. doi:10.3389/fped.2018.00117

153. Gomez A, Sainbhi AS, Stein KY, Vakitbilir N, Froese L, Zeiler FA. Statistical properties of cerebral near infrared and intracranial pressure-based cerebrovascular reactivity metrics in moderate and severe neural injury: a machine learning and time-series analysis. *Intensive Care Med Exp*. 2023;11(1):57. doi:10.1186/s40635-023-00541-3

154. Petrovčič R, Rakusa M, Markota A. Monitoring of Cerebral Blood Flow Autoregulation after Cardiac Arrest. *Medicina (Kaunas)*. 2024;60(9):1381. doi:10.3390/medicina60091381

155. Brady KM, Lee JK, Kibler KK, et al. Continuous Time-Domain Analysis of Cerebrovascular Autoregulation Using Near-Infrared Spectroscopy. *Stroke*. 2007;38(10):2818-2825. doi:10.1161/STROKEAHA.107.485706

156. Regulation of the Cerebral Circulation During Development - Koehler - Major Reference Works - Wiley Online Library. Accessed January 16, 2025. https://onlinelibrary.wiley.com/doi/10.1002/cphy.c200028

157. Fourier JBJ. *The Analytical Theory of Heat*. Cambridge University Press; 2009.

158. Debnath L, Shah FA. *Wavelet Transforms and Their Applications*. Springer; 2014.

159. Gabor D. Theory of communication. Part 1: The analysis of information. *Journal of the Institution of Electrical Engineers - Part III: Radio and Communication Engineering*. 1946;93(26):429-441. doi:10.1049/ji-3-2.1946.0074

160. Hlawatsch F, Boudreaux-Bartels GF. Linear and quadratic time-frequency signal representations. *IEEE Signal Processing Magazine*. 1992;9(2):21-67. doi:10.1109/79.127284

161. Cohen L. *Time-Frequency Analysis*. Prentice Hall PTR; 1995.

162. Cohen L. Time-frequency distributions-a review. *Proceedings of the IEEE*. 1989;77(7):941-981. doi:10.1109/5.30749

163. Stark HG. *Wavelets and Signal Processing: An Application-Based Introduction*. Springer Science & Business Media; 2005.

164. Compton AH, Heisenberg W. The Physical Principles of the Quantum Theory. In: Blum W, Dürr HP, Rechenberg H, eds. *Scientific Review Papers, Talks, and Books Wissenschaftliche Übersichtsartikel, Vorträge Und Bücher*. Springer; 1984:117-166. doi:10.1007/978-3-642-61742-3_10

165. Morlet J, Arens G, Fourgeau E, Glard D. Wave propagation and sampling theory—Part I: Complex signal and scattering in multilayered media. *GEOPHYSICS*. 1982;47(2):203-221. doi:10.1190/1.1441328

166. Morlet J, Arens G, Fourgeau E, Giard D. Wave propagation and sampling theory—Part II: Sampling theory and complex waves. *GEOPHYSICS*. 1982;47(2):222-236. doi:10.1190/1.1441329

167. Li Z min, Cui L guo, Xu S wei, et al. Prediction Model of Weekly Retail Price for Eggs Based on Chaotic Neural Network. *Journal of Integrative Agriculture*. 2013;12(12):2292-2299. doi:10.1016/S2095-3119(13)60610-3

168. Mak M. Orthogonal Wavelet Analysis: Interannual Variability in the Sea Surface Temperature. *Bulletin of the American Meteorological Society*. 1995;76(11):2179-2186.

169. Lindsay RW, Percival DB, Rothrock DA. The discrete wavelet transform and the scale analysis of the surface properties of sea ice. *IEEE Transactions on Geoscience and Remote Sensing*. 1996;34(3):771-787. doi:10.1109/36.499782

170. Kaiser G. *A Friendly Guide to Wavelets*. Springer Science & Business Media; 1994.

171. Torrence C, Compo GP. A Practical Guide to Wavelet Analysis. *Bulletin of the American Meteorological Society*. Published online February 1, 1998. doi:10.1175/1520-0477(1998)079<0061:APGTWA>2.0.CO;2

172. Baidya R, Lee SW. Addressing the Non-Stationarity and Complexity of Time Series Data for Long-Term Forecasts. *Applied Sciences*. 2024;14(11):4436. doi:10.3390/app14114436

173. Fulcher BD, Little MA, Jones NS. Highly comparative time-series analysis: the empirical structure of time series and their methods. *J R Soc Interface*. 2013;10(83):20130048. doi:10.1098/rsif.2013.0048

174. Lehman LWH, Adams RP, Mayaud L, et al. A Physiological Time Series Dynamics-Based Approach to Patient Monitoring and Outcome Prediction. *IEEE J Biomed Health Inform*. 2015;19(3):1068-1076. doi:10.1109/JBHI.2014.2330827

175. Bhandary M. Estimation of Covariance Matrix in Signal Processing When the Noise Covariance Matrix is Arbitrary. *Journal of Modern Applied Statistical Methods*. 2008;7(1). doi:10.22237/jmasm/1209615300

176. Elvander F, Karlsson J. Variance Analysis of Covariance and Spectral Estimates for Mixed-Spectrum Continuous-Time Signals. *IEEE Transactions on Signal Processing*. 2023;71:1395-1407. doi:10.1109/TSP.2023.3266474

177. Margalit G, Kable J. Cross-Correlations and their Applications to Brain Patterns and Sound Waves.

178. Cai X, Xu T, Yi J, Huang J, Rajasekaran S. DTWNet: a Dynamic Time Warping Network. In: *Advances in Neural Information Processing Systems*. Vol 32. Curran Associates, Inc.; 2019. Accessed January 28, 2025. https://papers.nips.cc/paper_files/paper/2019/hash/02f063c236c7eef66324b432b748d15d-Abstract.html

179. Senin P. Dynamic Time Warping Algorithm Review. Published online January 1, 2009.

180. Lin J, Keogh E, Lonardi S, Chiu B. A symbolic representation of time series, with implications for streaming algorithms. In: *Proceedings of the 8th ACM SIGMOD Workshop on Research Issues in Data Mining and Knowledge Discovery*. DMKD '03. Association for Computing Machinery; 2003:2-11. doi:10.1145/882082.882086

181. Liu PC. Wavelet Spectrum Analysis and Ocean Wind Waves. In: Vol 4. Elsevier; 1994:151-166. doi:10.1016/B978-0-08-052087-2.50012-8

182. Ge Z. Significance tests for the wavelet cross spectrum and wavelet linear coherence. In: ; 2008. Accessed January 28, 2025. https://www.semanticscholar.org/paper/Significance-tests-for-the-wavelet-cross-spectrum-Ge/b07c51b76e0bc7ac1102a01cdf8d8a830f9fd336

183. Comparing time series using wavelet-based semblance analysis. *Computers & Geosciences*. 2008;34(2):95-102. doi:10.1016/j.cageo.2007.03.009

184. Torrence C, Webster PJ. Interdecadal Changes in the ENSO–Monsoon System. Published online August 1, 1999. Accessed January 29, 2025. https://journals.ametsoc.org/view/journals/clim/12/8/1520-0442_1999_012_2679_icitem_2.0.co_2.xml

185. Foufoula-Georgiou E, Kumar P. *Wavelets in Geophysics*. Elsevier; 2014.

186. Ge Z. Significance tests for the wavelet power and the wavelet power spectrum. *Annales Geophysicae*. 2007;25(11):2259-2269. doi:10.5194/angeo-25-2259-2007

187. Ge Z, Liu PC. A time-localized response of wave growth process under turbulent winds. *Annales Geophysicae*. 2007;25(6):1253-1262. doi:10.5194/angeo-25-1253-2007

188. Elsayed MAK. Nonlinear Wave-Wave Interactions. *Journal of Coastal Research*. 2008;24(3):692-700. doi:10.2112/05-0445.1

189. Grinsted A, Moore JC, Jevrejeva S. Application of the cross wavelet transform and wavelet coherence to geophysical time series. *Nonlinear Processes in Geophysics*. 2004;11(5/6):561-566. doi:10.5194/npg-11-561-2004

190. Garg A, Xu D, Laurin A, Blaber AP. Physiological interdependence of the cardiovascular and postural control systems under orthostatic stress. *Am J Physiol Heart Circ Physiol*. 2014;307(2):H259-264. doi:10.1152/ajpheart.00171.2014

191. Hermans T, Carkeek K, Dereymaeker A, et al. Partial wavelet coherence as a robust method for assessment of neurovascular coupling in neonates with hypoxic ischemic encephalopathy. *Sci Rep*. 2023;13(1):457. doi:10.1038/s41598-022-27275-8

192. Bernjak A, Stefanovska A. Importance of wavelet analysis in laser Doppler flowmetry time series. *Annu Int Conf IEEE Eng Med Biol Soc*. 2007;2007:4064-4067. doi:10.1109/IEMBS.2007.4353226

193. Ince C. Hemodynamic coherence and the rationale for monitoring the microcirculation. *Crit Care*. 2015;19(Suppl 3):S8. doi:10.1186/cc14726

194. Liu X, Hu X, Brady KM, et al. Comparison of wavelet and correlation indices of cerebral autoregulation in a pediatric swine model of cardiac arrest. *Sci Rep*. 2020;10(1):5926. doi:10.1038/s41598-020-62435-8

195. Liu X, Donnelly J, Czosnyka M, et al. Cerebrovascular pressure reactivity monitoring using wavelet analysis in traumatic brain injury patients: A retrospective study. *PLoS Med*. 2017;14(7):e1002348. doi:10.1371/journal.pmed.1002348

196. Duncan A, Meek JH, Clemence M, et al. Measurement of Cranial Optical Path Length as a Function of Age Using Phase Resolved Near Infrared Spectroscopy. *Pediatr Res*. 1996;39(5):889-894. doi:10.1203/00006450-199605000-00025

197. GitHub - sccn/labstreaminglayer: LabStreamingLayer super repository comprising submodules for LSL and associated apps. Accessed October 21, 2024. https://github.com/sccn/labstreaminglayer

198. Yeh CCM, Zhu Y, Ulanova L, et al. Matrix Profile I: All Pairs Similarity Joins for Time Series: A Unifying View That Includes Motifs, Discords and Shapelets. In: *2016 IEEE 16th International Conference on Data Mining (ICDM)*. ; 2016:1317-1322. doi:10.1109/ICDM.2016.0179

199. Addison PS. A Review of Wavelet Transform Time-Frequency Methods for NIRS-Based Analysis of Cerebral Autoregulation. *IEEE Rev Biomed Eng*. 2015;8:78-85. doi:10.1109/RBME.2015.2436978

200. Dinç E, Yazan Z. Wavelet Transform-Based UV Spectroscopy for Pharmaceutical Analysis. *Frontiers in Chemistry*. 2018;6. Accessed March 5, 2024. https://www.frontiersin.org/articles/10.3389/fchem.2018.00503

201. Duan L, Zhao Z, Lin Y, Wu X, Luo Y, Xu P. Wavelet-based method for removing global physiological noise in functional near-infrared spectroscopy. *Biomedical Optics Express*. 2018;9(8):3805. doi:10.1364/BOE.9.003805

202. Zhang X, Noah JA, Dravida S, Hirsch J. Optimization of wavelet coherence analysis as a measure of neural synchrony during hyperscanning using functional near-infrared spectroscopy. *Neurophotonics*. 2020;7(1):015010. doi:10.1117/1.NPh.7.1.015010

203. Bu L, Li J, Li F, Liu H, Li Z. Wavelet coherence analysis of cerebral oxygenation signals measured by near-infrared spectroscopy in sailors: an exploratory, experimental study. *BMJ Open*. 2016;6(11):e013357. doi:10.1136/bmjopen-2016-013357

204. Torrence C, Compo GP. A Practical Guide to Wavelet Analysis. Published online January 1, 1998. Accessed December 19, 2024. https://journals.ametsoc.org/view/journals/bams/79/1/1520-0477_1998_079_0061_apgtwa_2_0_co_2.xml

205. Mitra S, Bale G, Highton D, et al. Pressure passivity of cerebral mitochondrial metabolism is associated with poor outcome following perinatal hypoxic ischemic brain injury. *J Cereb Blood Flow Metab*. 2019;39(1):118-130. doi:10.1177/0271678X17733639

206. Bergmann T, Froese L, Gomez A, et al. Evaluation of Morlet Wavelet Analysis for Artifact Detection in Low-Frequency Commercial Near-Infrared Spectroscopy Systems. *Bioengineering*. 2024;11(1):33. doi:10.3390/bioengineering11010033

207. Folgosi-Correa MS, Nogueira GEC. Quantifying low-frequency fluctuations in the laser Doppler flow signal from human skin. In: *Dynamics and Fluctuations in Biomedical Photonics VIII*. Vol 7898. SPIE; 2011:190-195. doi:10.1117/12.874080

208. Kvandal P, Landsverk SA, Bernjak A, Stefanovska A, Kvernmo HD, Kirkebøen KA. Low-frequency oscillations of the laser Doppler perfusion signal in human skin. *Microvasc Res*. 2006;72(3):120-127. doi:10.1016/j.mvr.2006.05.006

209. Bernjak A, Clarkson PBM, McClintock PVE, Stefanovska A. Low-frequency blood flow oscillations in congestive heart failure and after β1-blockade treatment. *Microvascular Research*. 2008;76(3):224-232. doi:10.1016/j.mvr.2008.07.006

210. Geyer MJ, Jan YK, Brienza DM, Boninger ML. Using wavelet analysis to characterize the thermoregulatory mechanisms of sacral skin blood flow. *J Rehabil Res Dev*. 2004;41(6A):797-806. doi:10.1682/jrrd.2003.10.0159

211. Stefanovska A. Coupled oscillators. Complex but not complicated cardiovascular and brain interactions. *IEEE Eng Med Biol Mag*. 2007;26(6):25-29. doi:10.1109/emb.2007.907088

212. Mohammadzadeh L, Latifi H, Khaksar S, et al. Measuring the Frequency-Specific Functional Connectivity Using Wavelet Coherence Analysis in Stroke Rats Based on Intrinsic Signals. *Sci Rep*. 2020;10(1):9429. doi:10.1038/s41598-020-66246-9

APPENDIX A

Table A.1: Comparative Analysis of Wavelet Coherence of ICU Survivors vs. Healthy Controls.

Frequency bands	Brain – Muscle	
	Healthy (15)	ICU Survivors (20)
Microvascular (B2–B4)	2.72% (0.79% - 10.46%)	2.78% (0.82% - 5.72%)
Cardiac (B6)	97.14% (93.19% - 98.61%)	90.38% (56.37% - 98.43%)
	Brain - ABP	
	Healthy (12)	ICU Survivors (18)
Microvascular (B2–B4)	1.58% (0% - 5.91%)	3.09% (1.00% - 16.97%)
Cardiac (B6)	94.78% (53.11% - 96.75%)	92.00% (68.85% - 98.96%)
	Muscle - ABP	
	Healthy (12)	ICU Survivors (17)
Microvascular (B2–B4)	0.40% (0% - 1.97%)	4.81% (0.04% - 6.59%)
Cardiac (B6)	86.21% (55.19% - 98.21%)	83.78% (65.73% - 98.54%)

Comparative analysis of wavelet coherence (%signfCoherenceDuration) between ICU survivors and healthy controls across three physiological signal pairs: Brain–Skeletal Muscle, Brain–ABP/NIBP, and Skeletal Muscle–ABP/NIBP within the cardiac (B6) and Microvascular (B2–B4) frequency bands. Data are presented as median (IQR). Statistical comparisons were conducted using the Mann–Whitney U non-parametric test. Asterisks (**) indicate statistically significant differences at $p < 0.05$.

Table A.2: Comparative Analysis of Wavelet Coherence of ICU Non-survivors vs. Healthy Controls.

Frequency bands	Brain – Muscle	
	Healthy (15)	ICU non-survivors (11)
Microvascular (B2–B4)	2.72% (0.79% - 10.46%)	7.13% (0.92%-18.35%)
Cardiac (B6) **	97.14% (93.19% - 98.61%)	78.76% (57.07%-96.05%)
	Brain - ABP	
	Healthy (12)	ICU non-survivors (8)
Microvascular (B2–B4)	1.58% (0% - 5.91%)	6.51% (2.94% - 18.68%)
Cardiac (B6)	94.78% (53.11% - 96.75%)	69.83% (43.91%- 78.46%)
	Muscle - ABP	
	Healthy (12)	ICU non-survivors (9)
Microvascular (B2–B4) **	0.40% (0% - 1.97%)	6.05% (4.58% - 40.05%)
Cardiac (B6)	86.21% (55.19% - 98.21%)	77.20% (51.23% - 79.99%)

Comparative analysis of wavelet coherence (%signfCoherenceDuration) between ICU non survivors and and healthy controls across three physiological signal pairs: Brain–Skeletal Muscle, Brain–ABP/NIBP, and Skeletal Muscle–ABP/NIBP within the cardiac (B6) and Microvascular (B2–B4) frequency bands. Data are presented as median (IQR). Statistical comparisons were conducted using the Mann–Whitney U non-parametric test. Asterisks (**) indicate statistically significant differences at $p < 0.05$.

Table A.3: Comparative Analysis of Wavelet Semblance of ICU Survivors vs. and Healthy Controls.

Frequency bands	Brain – Muscle	
	Healthy (15)	ICU survivors (20)
Microvascular (B2–B4)	0.39 (0.30 – 0.49)	0.36 (0.08 - 0.49)
Cardiac (B6) **	0.71 (0.59 – 0.75)	0.31 (0.22 - 0.53)
	Brain - ABP	
	Healthy (12)	ICU survivors (18)
Microvascular	0.20 (0.08 – 0.39)	0.22 (-0.07 - 0.55)
Cardiac (B6) **	-0.034 (-0.08 – 0.00)	-0.40 (-0.47 - -0.28)
	Muscle - ABP	
	Healthy (12)	ICU survivors (17)
Microvascular (B2–B4)	0.20 (0.12 – 0.29)	0.23 (-0.14 - 0.33)
Cardiac (B6)	-0.04 (-0.23 – 0.021)	-0.28 (-0.36 - -0.18)

Comparative analysis of wavelet semblance between ICU Survivors and Healthy controls across three physiological signal pairs: Brain–Skeletal Muscle, Brain–ABP/NIBP, and Skeletal Muscle–ABP/NIBP within the cardiac (B6) and Microvascular (B2–B4) frequency bands. Data are presented as median (IQR). Statistical comparisons were conducted using the Mann–Whitney U non-parametric test. Asterisks (**) indicate statistically significant differences at $p < 0.05$.

Table A.4: Comparative Analysis of Wavelet Semblance of ICU Non-Survivors vs. and Healthy Controls.

Frequency bands	Brain – Muscle	
	Healthy (15)	ICU non- survivors (11)
Microvascular (B2–B4)	0.39 (0.30 – 0.49)	0.48 (0.14 - 0.55)
Cardiac (B6) **	0.71 (0.59 – 0.75)	0.43 (0.21 - 0.56)
	Brain - ABP	
	Healthy (12)	ICU non- survivors (8)
Microvascular (B2–B4)	0.20 (0.08 – 0.39)	0.20 (0.11 - 0.40)
Cardiac (B6) **	-0.034 (-0.08 – 0.00)	-0.28 (-0.38 - -0.20)
	Muscle - ABP	
	Healthy (12)	ICU non-survivors (9)
Microvascular (B2–B4) **	0.20 (0.12 – 0.29)	0.52 (0.24 - 0.56)
Cardiac (B6) **	0.04 (-0.23 – 0.021)	-0.44 (-0.47 - -0.38)

Comparative analysis of wavelet semblance between ICU non survivors and healthy controls across three physiological signal pairs: Brain–Skeletal Muscle, Brain–ABP/NIBP, and Skeletal Muscle–ABP/NIBP within the Cardiac (B6) and Microvascular (B2–B4) frequency bands. Data are presented as median (IQR). Statistical comparisons were conducted using the Mann–Whitney U non-parametric test. Asterisks (**) indicate statistically significant differences at $p < 0.05$.